Title

Dynamic microvillar search in traditional and synthetic ligand detection by T cells

Permalink

https://escholarship.org/uc/item/4rr2q4m8

Author

Beppler, Casey

Publication Date

2022

Supplemental Material

https://escholarship.org/uc/item/4rr2q4m8#supplemental

Peer reviewed|Thesis/dissertation

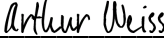Dynamic microvillar search in traditional and synthetic ligand detection by T cells

by
Casey Beppler

DISSERTATION
Submitted in partial satisfaction of the requirements for degree of
DOCTOR OF PHILOSOPHY

in

Biomedical Sciences

in the

GRADUATE DIVISION
of the
UNIVERSITY OF CALIFORNIA, SAN FRANCISCO

Approved:

DocuSigned by:
Arthur Weiss   Arthur Weiss
A45915AB27B74F5...   Chair

DocuSigned by:
Matthew Krummel   Matthew Krummel
DocuSigned by: 445...

Kole Roybal   Kole Roybal
DocuSigned by: 48B...

Orion Weiner   Orion Weiner
DC0B9413C4A0416...

Committee Members

This dissertation is dedicated to my parents, Scott and Anne Marie Beppler,

who made it possible for me to attend graduate school.

And to my partner, Trenton Pantaleoni, who made it possible for me to finish.

Acknowledgements

Contributions

This thesis work was performed under the direct supervision of Dr. Matthew M. Krummel with guidance from Dr. Kole Roybal. Thesis committee chair Arthur Weiss and committee member Orion Weiner provided valuable insight throughout project development.

Chapter 2 adapted from:

Beppler, C.*, Cai, E.*, K. Marchuk*, P. Beemiller*, M.G. Rubashkin, V.M. Weaver, A. Gerard, T.-L. Liu, B.-C. Chen, E. Betzig, F. Bartumeus, and M.F. Krummel. 2017. Visualizing dynamic microvillar search and stabilization during ligand detection by T cells. *Science (80-.).* 356. doi:10.1126/science.aal3118.
*These authors contributed equally to this work.

PB, KM, CB, EC and MFK designed the experiments. PB and MGR performed the SAIM imaging experiments. PB, EC and CB performed SCM experiments and AG performed 2-photon imaging. KM, CB and EC performed the remaining experiments. TL, BC and EB provided critical support for LLS microscopy. FB, CB and KM performed diffusion and fractal analysis. VW provided financial support. MFK wrote the paper together with KM, CB and EC.

Chapter 3 adapted from:

Beppler, C., J. Eichorst, K. Marchuk, E. Cai, C.A. Castellanos, V. Sriram, K.T. Roybal, and M.F. Krummel. 2022. Visualizing and manipulating hyperstabilization of T cell microvilli contacts by engineered chimeric antigen receptors. *bioRxiv.* 2021.08.18.456686. doi:10.1101/2021.08.18.456686.

C.B. designed, conducted, and analyzed most experiments, and drafted the manuscript. J.E. and K.M. authored unique MatLab codes and discussed data. K.M. also assisted with LLS imaging acquisition. E.C. discussed project design. C.A.C. assisted with experiments and discussed data. V.S. designed affinity measurement experiments. K.T.R. contributed to the formulation of the project, designed experiments, provided reagents for experiments involving human T cells, and interpreted data. M.F.K. contributed to the formulation of the project, designed experiments, interpreted data, and developed the manuscript. All authors contributed manuscript revisions.

Dynamic microvillar search in traditional and synthetic ligand detection by T cells

Casey Beppler

Abstract

A T cell's ability to efficiently surveil its environment and recognize and respond appropriately to cognate antigen via its antigen receptor is a critical feature of adaptive immunity. Although cell-cell interactions are often depicted as two flat surfaces pushing up against each other with molecules moving laterally within a single plane, the reality is that T cells must probe three-dimensionally complex surfaces covered in relatively large, glycosylated molecules as they migrate through lymph nodes and other tissues during immune surveillance. Yet, it is unknown how T cells overcome these barriers to make very close contact with apposing membranes, bringing together the small membrane receptors that initiate T cell signaling. Prior to these studies, whether T cells use their membrane microvilli to aid in detection of antigen was largely unknown.

Here, we used lattice light sheet (LLS) microscopy and synaptic contact mapping (SCM) total internal reflection fluorescence (TIRF) imaging to visualize microvilli on T cells with high spatiotemporal resolution prior to and during ligand detection by T cells. We found that T cell microvilli are highly dynamic structures that efficiently probe surfaces in physiologically relevant timescales. Specifically, upon binding of the T cell antigen receptor (TCR) to cognate ligand, the underlying microvillus became stabilized, providing a persistent surface for signaling. Of note, ZAP70 catalytic function and actin polymerization were not required to maintain these close

contacts after binding to cognate antigen, indicating that physical pinning of membranes via membrane receptors is a significant contributor to changes in membrane dynamics.

Given that natural antigen receptors make use of this cell biology, we then asked whether engineered chimeric antigen receptors (CARs) interact similarly. We found that CARs distributed in the plasma membrane similarly to natural TCRs, although notably in distinct patches. However, when engaging ligands these induced hyper-stabilization of the underlying microvilli relative to that of the TCR. This hyper-stabilization was dependent on the high affinity and avidity of CAR binding and was associated with altered organization of molecules at the cell-cell interface, decreased effector function, and increased propensity for exhaustion. Thus, although microvillar search is involved in both natural and synthetic ligand detection, microvillar dynamics are differentially altered depending on strength of receptor binding. This work reveals the cell biology underlying T cell ligand detection and its sensitivity to changes in binding dynamics, with likely clinical importance for the development of cell therapies.

Table of Contents

List of Figures

List of Tables

Chapter 1 – Introduction

The ability to communicate via the formation of receptor-ligand complexes at cell-cell interfaces is a basic requirement of multicellular organisms. However, the three-dimensional topology of the plasma membrane and its dynamics underlying the formation of and signaling through receptor complexes is often overlooked. One such critical interface exists at the immune synapse (IS), where T cells interact with antigen presenting cells (APCs) and initiate the signaling cascade that ultimately leads to a robust adaptive immune response. Whether and how T cells use their finger-like membrane protrusions, called microvilli, in the process of natural and synthetic ligand detection is the subject of this dissertation.

Part 1 – T cell activation at the immune synapse

Signaling via the T cell antigen receptor (TCR) is required for a T cell to gain effector functions and elicit an adaptive immune response when faced with a pathogen or cancer. Ligand detection is a fundamental requirement in the initiation of TCR signaling, and occurs at the T cell-APC interface, or IS, which has been well described in two dimensions[1–3]. The key recognition event involves TCR binding to a cognate peptide in the context of major histocompatibility complex (pMHC)[4]. A critical feature of TCR:pMHC recognition is that it is sensitive to the identity of the peptide that is bound in the MHC groove[5–8]. APCs that present cognate pMHC do so alongside an abundance of non-cognate pMHC molecules[9–12]. The ability of the T cell to find rare cognate pMHC is critical[13]. Furthermore, the antigen presenting surface also presents a complex surface to scan since it has its own three-dimensional topology and is decorated with a dense glycocalyx[14–16]. Thus, immune surveillance requires efficient and thorough three-dimensional T cell scanning of APCs for rare cognate pMHC.

Features of TCR binding to pMHC that contribute to ligand sensitivity

The affinities of TCR complexes for their cognate pMHC[17–19] are relatively low compared to their antigen receptor (and antibody) counterpart on B cells[20–23]. Nevertheless, T cells can respond to low density agonist pMHC on target cells[24–27]. The off-rate of the TCR:pMHC complex is inversely correlated with stimulatory capacity[17,28], and dense packing or concatenation of TCRs, resulting in increased avidity, have been shown to significantly increase the T cell's sensitivity to antigen[26,29–33]. TCR mutants incapable of dimerizing show impaired synapse formation and intracellular signaling[34]. Various non-mutually exclusive models have been proposed to explain how TCR binding of pMHC results in signaling, involving conformational changes[35–38], aggregation of signaling components at TCR microclusters[39,40], kinetic proofreading[41], or kinetic segregation[42–45], and it may well be that all of these mechanisms contribute to facilitating signal

2

transduction. In all of these models, the ability to achieve a local avid binding surface appears crucial to discrimination of and sensitivity to stimulatory antigen, and yet our understanding of the structure of that surface remains limited.

Organization of TCRs at the IS

T cell synapse dynamics are most thoroughly described for T cells interacting with antigen-presenting supported lipid bilayers (SLBs)[1,46–49]. In this experimental design, a lipid bilayer is formed on a glass coverslip and loaded with pMHC and other T cell-binding proteins, e.g. ICAM[50]. Total internal reflection fluorescence (TIRF) microscopy improves imaging resolution for IS formed on SLBs, allowing for visualization of small clusters of molecules[51–53]. TIRF benefits from the specific illumination of a thin (~100 nm) section directly adjacent to the glass support by an evanescent wave. Thus, background fluorescence outside the focal plane is eliminated, resulting in improved signal-to-noise ratio and spatial resolution. Given the thin optical section available, this modality is ideally suited for the analysis of molecules that localize to the membrane at the SLB-cell interface, as is the case for TCRs on a T cell interacting with a cognate pMHC-loaded SLB.

When T cell synapses form on cognate pMHC-loaded SLBs, TCRs rapidly coalesce, along with other signaling components[33,54], to form submicron-sized microclusters. Over the subsequent minutes, these move radially towards the center of the IS into a larger aggregation which has been named the central supramolecular activation cluster (cSMAC)[55]. TCR signaling occurs at peripheral microclusters[56,57]. Despite its name, the cSMAC is now understood to be where signaling ends[53], TCRs internalize[58,59], and when viewed by EM is also characterized by the accumulation of large numbers of extracellular TCR-containing vesicles which contribute to the high density of TCRs observed by lower resolution methods[60] . On SLBs, this prototypical

organization at the IS is indicative of activating TCR signals – SLBs without cognate pMHC do not induce the formation of microclusters or SMACs. A central clustering of TCRs has also been observed for interactions of T cells with B cells and target cells[61], but dendritic cells, known to induce robust T cell activation, more often induce multifocal synapse structures[62]. These are characterized by the appearance of stable peripheral clusters of TCRs and signaling molecules, which do not coalesce into a cSMAC[61]. Notably, transient and dynamic synapses, or kinapses, are predominant in lymph nodes as T cells migrate across APCs in vivo[63–65]. During T cell development, multifocal synapses also form during negative selection[66], a process in which TCRs that signal too strongly in response to self-ligand induce cell death[67]. Thus, functional IS take on a variety of structures in different contexts, and with different implications for T cell fate.

Part 2 – T cell microvilli

T cells are covered in actin-dependent microvilli[68] that aid in adhesion to vascular endothelium[69,70], but little else is known about their biology or function. Much more is known about the microvilli on gut epithelial cells which aid in absorption, termed the brush border[71]. Brush border microvilli are long-lived structures with limited motility – nascent epithelial microvilli move at about 0.2 µm/min[72]. Because T cell microvilli were observed previously only by scanning electron microscopy[73,74] which requires cell fixation, the dynamics of microvilli on T cells remain largely unknown.

We hypothesized that these small membrane protrusions may enable a T cell to more thoroughly probe topologically complex APCs for cognate ligand in the limited time that they spend in contact with a given cell – about one minute for lymph node dendritic cells[13]. In order for T cells to use microvilli in this way, TCRs must be present on microvilli. TCR distribution relative to microvilli has only recently been assessed experimentally. While some discrepancies in the literature exist, likely due to differences in imaging modality chosen, at least some portion of TCRs are found at the tips of microvilli prior to ligand detection[75,76].

With the development of lattice light sheet (LLS) microscopy[77], the contributions of T cell microvilli to antigen scanning can now be assessed with high spatiotemporal resolution in live cell-cell contacts. This method uses illumination by a patterned sheet of light to create thin optical sections, yielding high axial resolution and fast acquisition of full volumes. Thus, LLS imaging is well-suited to determine the dynamics of microvilli on the T cell surface before and during ligand detection.

Part 3 – Ligand detection by conventional chimeric antigen receptor T cells

A chimeric antigen receptor (CAR) is a receptor made up of domains derived from multiple different proteins. Modern CAR technology has been applied in several contexts. Areas of active research and ongoing clinical trials today include CAR expression on T cells[78–81], NK cells[82,83] and macrophages[84,85] for cancer treatment, expression on regulatory T cells for use in autoimmunity and transplant rejection[86,87]; and expression on T cells, natural killer (NK) cells, and stem cells for HIV treatment[88,89]. Work in this dissertation focuses on CARs expressed, as described below, on conventional T cells for the purpose of directing their cytotoxic functions at tumor cells – the only application for which current FDA approvals exist[90].

Elements of conventional CAR T cell design

The first receptors resembling modern CARs were made of fused immunoglobulin- and TCR-derived domains[91,92]. Extracellular binding (in this case by CD8) paired to CD3ζ was then shown to be sufficient for T cell activation[93]. On the exterior face of the cell, today's CARs typically use an antibody-derived single chain variable fragment (scFv) for binding. However, as with most components of the CAR, this domain can be derived from many different molecules, e.g. nanobodies, ligands, receptors, cytokines, or other peptides[94–99]. The binding domain attaches to an extracellular hinge region, typically CD8-, CD28-, or immunoglobulin Fc-derived. Disulfide bonds in these hinge regions lead to dimerization[100–102]. Thus, typical CARs are dimers. The transmembrane domain of CARs is typically from either CD8 or CD28[103]. Intracellular signaling domains include the CD3ζ chain and a co-stimulatory domain, typically derived from either 4-1BB or CD28[81,104–106]. These fusion proteins allow the T cell to be directed to bind a molecule on the surface of an opposing cell (e.g. a tumor cell) and then initiate an intracellular signaling cascade, ultimately leading to cytotoxicity[107].

Challenges in CAR T cell therapies for solid tumors

The development of CAR T cells revolutionized the field of cancer immunotherapy, providing successful clinical outcomes for the treatment of B cell malignancies including chronic lymphocytic leukemia[108,109], acute lymphocytic leukemia[110–114], diffuse large B cell lymphoma[115,116], and multiple myeloma[117–119]. There are six currently FDA-approved CAR T cell therapies[90], of which four target the pan-B cell marker CD19 and two target B-cell maturation antigen (BCMA, primarily expressed on plasma cells). In each of these cases, CAR T cells are remarkably effective at killing cells that maintain high expression of unmutated antigen[120,121], leading to the depletion of all B cells in patients receiving anti-CD19 CAR therapies. A key commonality of these FDA-approved therapies is their use to treat a hematologic malignancy. However, efforts to translate CAR T cell successes to solid tumors have revealed deficiencies in the currently engineered biology.

Challenges in CAR T cell therapies for solid tumors include the lack of CAR T cell infiltration into the tumor (due to deficiencies in trafficking or in overcoming physical barriers)[122], incomplete tumor clearance and escape variants[123], and importantly, a failure of cells to persist in a functional effector state[124]. In one recent study, large-scale aggregation of a disialoganglioside GD2-targeting CAR, caused by unintended interactions in scFv framework regions, resulted in over-triggering of T cells via tonic signaling and exhaustion[125]. Clinically, CAR T cell products with a more naïve or stem cell memory-like phenotype have been reported as more effective[126]. Studies like these highlight the need to optimize the quality of the CAR T cell product that is administered to patients to ensure that their long-term functionality.

Another significant challenge lies in the identification of actionable tumor antigens[123,127]. Given the paucity of tumor-specific antigens (TSAs) and their uniqueness within given patients, one strategy has been to target tumor-associated antigens (TAAs). Many such TAAs have been

tested as CAR therapy-directed targets including: human epidermal growth factor receptor 2 (HER2) for breast, ovarian, and other cancers[128,129]; epidermal growth factor receptor (EGFR) for non-small cell lung cancer (NSCLC), glioblastoma (GBM), and others[129,130]; carcinoembryonic antigen (CEA) for ovarian, gastrointestinal, and other cancers[129,131]; GD2 for neuroblastoma, melanoma, and others[129,132]; and mucin 1 (MUC1) for hepatocellular carcinoma (HCC), NSCLC, and others[129,133]. For each of these CAR T cell therapies, it is critical to discriminate between high level target antigen on tumor cells (on-target, on-tumor) and low level expression of the same antigen on healthy cells (on-target, off-tumor). On-target recognition of off-tumor antigen can lead to serious clinical toxicities[134]. Several strategies have been proposed in attempts to circumvent this problem[135–142]. Given the intricacies of targeting TAAs, we hypothesize that understanding the nature of ligand engagement will improve future TAA-targeting CAR engineering.

CAR binding modality and antigen scanning

Signaling events initiated by scFv binding and subsequent phosphorylation of intracellular components at the immune synapse lead to the acquisition of CAR T cell effector functions. Although a CAR T cell's ability to scan for cognate antigen is of critical importance, very little is known about how CAR-bearing cells engage in ligand scanning or synapse formation[143,144]. One key difference between TCRs and CARs which might be expected to affect antigen scanning and IS formation is their difference in binding modality. TCRs specifically recognize peptides presented by MHC[4], whereas CARs can target any molecule expressed on the cell surface. This means that even two CARs targeting the same antigen can have variable binding orientation depending on both the epitope site[145] and the hinge length[146]. Additionally, natural TCRs bind agonist pMHCs with micromolar affinities[147], whereas CAR scFvs, derived from high affinity antibody binding domains, bind antigen with nano- or even picomolar affinities. Furthermore,

typical CARs dimerize via the extracellular hinge regions[100–102] which increases the avidity of their binding. Whether any of these differences in binding might contribute to alterations in antigen scanning and IS formation[143] is unknown. This thesis work focuses on the effects of affinity and avidity of conventional high affinity dimer CAR binding.

The rationale for critically assessing the dynamics and antigen scanning downstream of conventional high affinity dimer CAR binding is supported by evidence that there is an upper efficacy limit on CAR affinity and antigen density[137,142,148,149]. Reduced activation or effector functions have also been described for TCR:pMHC interactions with supraphysiological binding dynamics[150–157]. SHP-1 expression has been shown to increase with increasing TCR affinity, while other signaling and activation markers increased for increasing affinities up to ~1 μM and then declined[158]. Serial triggering of TCRs, which is especially important in settings of limited pMHC[157], depends on the receptor's rate of dissociation. TCRs that are made not to dissociate by photo-crosslinking can't engage in serial triggering and do not sustain calcium flux[155].

These studies are line with a prevalent theme in T cell biology which is often overlooked in synthetic T cell engineering – T cell functions are highly tuned to respond to a certain range and duration of stimulation. Synthetic biology applied to any existing biological system must be designed with that natural biology in mind. CAR T cell engineering in particular aims to redesign a process for which the cell is exquisitely regulated even from early development. TCRs expressed on peripheral T cells are selected for in the thymus via a complex and tightly regulated process of positive and negative selection to produce receptors that will functionally but specifically bind non-self pMHC[159,160]. Even within the natural range of TCR binding affinities, the flavor of T cell responses will differ depending on strength of TCR signals, along with interpretation of other cues (co-stimulation, cytokines, etc.)[161,162]. Sustain strong signaling via the TCR and cells will undergo activation-induced cell death[163]. Receive chronic TCR

stimulation and cells will persist in a dysfunctional, or exhausted, state[164,165]. Thus, T cells have

told us again and again that it is indeed possible to have too much of a good thing.

Chapter 2 – Visualizing Dynamic Microvillar Search and Stabilization during Ligand Detection by T cells

Material for this chapter comes from the following published work:

Abstract

During immune surveillance, T cells survey the surface of antigen presenting cells. In searching for peptide-loaded major histocompatibility complexes (pMHC), they must solve a classic tradeoff between speed and sensitivity. It has long been supposed that microvilli on T cells act as sensory organs to enable search, but their strategy has been unknown. We used lattice light sheet and Qdot-enabled synaptic contact mapping microscopy to show that anomalous diffusion and fractal organization of microvilli survey the majority of opposing surfaces within one minute. Individual dwell times were long enough to discriminate pMHC half-lives and T cell receptor (TCR) accumulation selectively stabilized microvilli. Stabilization was independent of tyrosine kinase signaling and the actin cytoskeleton, suggesting selection for avid TCR microclusters. This work defines the efficient cellular search process against which ligand detection takes place.

Introduction

T cells use surface-bound T cell receptors (TCRs) to identify ligands on antigen-presenting cells (APCs). Detection results in rapid intracellular signaling, which is necessary for the acquisition of T cell effector functions and leads to adaptive immunity. The efficiency of search and detection has implications for the ability of T cells to discover rare epitopes and initiate a response[13], for example, during the early phases of a viral infection. The pathway to survey entire surfaces to detect rare ligands is likely to be exacerbated by the presence of a dense and wide glycocalyx, which is likely to inhibit whole scale surface-to-surface appositions[14,15] and would seem to make small villi a preferred energetic solution toward detecting relatively short ligands.

TCR recognition happens at the same time as surface deformations provide initial contact[2,33,69,166–171]. However, despite various fixed and lower-resolution approaches to understand this process, it has not been possible to study this complete surface in real-time in the full 3-dimensions in which it takes place. In particular, it is not clear how surface deformation is used to make detection efficient and whether the entire initial deformed surface is stable as soon as contact is made or whether cells might continue to "search" the surface in some form.

Fractal distribution of microvilli on the T cell surface and their effective scan of the opposing surface

We imaged membrane deformations across the entire surface of mouse T cells in culture at 0.22-0.44 Hz at diffraction-limited resolution using lattice light sheet microscopy (LLS)[77]. T cells were surface-labeled with either monodispersed non-stimulatory antibodies to the highly abundant surface molecule CD45 or using a membrane-bound form of the fluorophore tdTomato. Microvilli were found to be highly dynamic structures (**Fig 2.1A** and **Movies 2.1 and 2.2**). Most microvilli undulated and moved laterally, although we occasionally observed apparent reabsorption or projection from flatter membrane patches. We tracked microvillar movements and found that lateral displacements on the surface had a range of average speeds in individual cells (**Fig 2.1B**) with a mean across three cells of 5.2 ± 0.4 (SD) μm/min, which approximates the speed of T cell motility in vivo[172,173]. Microvillar movements covered a wide range of angles between timepoints (**Fig 2.1C**) with a close to uniform distribution of 82 ± 3 (SD) degrees (n=3), suggesting random turning. We characterized microvillar diffusive properties using mean squared displacement (MSD) by estimating the scaling exponent α in MSD~t^{α}. We found that α = 1.13 for time scales within 15 seconds, which resembles superdiffusive motion (**Fig 2.1D**). Over longer time scales, α = 0.85 (resembling subdiffusion), suggesting that each microvillus might also be modestly confined and/or colliding with neighboring microvilli. Microvilli velocity correlations were positive, gradually decaying up to 10 - 15 seconds to become then negative (**Fig 2.2A**). The presence of negative velocity correlations beyond 15 seconds supports the idea that microvilli display subdiffusion on a longer time scale. Microvilli are all part of one surface and their free and persistent motion may thus only last until they interact with some neighboring microvilli. This will lower the search efficiency for an individual microvillus, but because free-ranging search occurs on time scales of less than 15 seconds, it will have less effect on the overall search efficiency.

The dynamics of microvilli were also visualized by sequential line-scans of a patch of membrane over three sequential timepoints (e.g. 9 seconds; **Fig 2.1E**), which revealed tilting in addition to lateral motion of microvilli. However, when assessed over > 1 minute periods (**Fig 2.2B-C)** similar analysis did not support "hot spots" for scanning. This suggests a potential underlying order that distributes these projections. We thus assessed microvillar distribution across length scales and time by performing fractal analysis. Fractal geometries in nature often provide consistent coverage across scales[174,175], filling a volume or a surface in a compact and effective way, or assisting in finding adequate compromises between local exploitation and broad exploration[176]. Plots of the logarithm of the number of regions that are necessary to contain all microvilli versus the logarithm of the region size gave a linear relationship across 1.5 orders of magnitude (**Fig 2.1F** and **2.3A-B**), suggesting that microvilli distribution is indeed fractal. Notably, the observed fractal dimension F_d varied little with time (example **Fig 2.1F, inset**), suggesting that both a stationary stochastic and a complex dynamic process governs efficient microvillar-based scanning. Based on characterization of microvillar dynamics (**Fig 2.1D**), microvillar motion could be divided into two regimes: I. moderate superdiffusive motion over short time scales, and II. subdiffusive motion over longer time scales. These regimes may act similarly through time, which would account for a constant fractal dimension. The surface of the cell is on average quite crowded with microvillar protrusions given that a fractal dimension of 1.7 is relatively close to 2, namely, the topological dimension of the cell surface. However, the scaling (fractal) properties of microvillar protrusions cover a broad range of scales and ensure an efficient hierarchical embedding of the overall coverage, minimizing spatial overlaps.

To quantify how effectively these fractally distributed projections search opposing surfaces, we first considered a randomly selected cell-contact sized region just above the cell volume in the absence of any actual surface-contacts at that site (e.g. Mask, **Fig 2.1G** and **Fig 2.4**). We then quantified the distributions of microvilli projected from the T cell into that mask by applying a threshold to convert intensities into a binary map (e.g. Threshold, **Fig 2.1G**) using red to

represent instantaneously "occupied" space and black to represent "unoccupied" areas. Further, to identify regions that have ever been scanned, we created a "Cumulative" image in which red now represents space that had a microvillus at that site at any time (example in **Fig 2.1G** shows total coverage achieved within 13.5 seconds). We then generated a time-series of these projections (**Movie 2.3**) and plotted the instantaneous and cumulative percent occupancy over time (**Fig 2.1H**). We found that cells had very consistent degrees to which they were instantaneously surveying such a region, here having an average of 39.8% and deviating less than 10% from this at any time (we observed variation in the mean coverage, cell-to-cell, from 35-45%, **Fig 2.5B**). Notably, the apparently random movements of microvilli resulted in a very rapid rise in cumulative coverage over time; 98% of the putative surface was visited by at least one microvillar contact within 1 minute (**Fig 2.1H**). For perspective, the half-life of T cell-APC contacts in vivo is roughly 1 minute (**Fig 2.1H**), suggesting that nearly complete scanning can be done at physiological dwell times.

Altered microvilli dynamics upon antigen recognition

We next sought to determine whether membrane movements changed upon recognition of pMHC, presumably the goal for which the search is ideally tuned. We thus analyzed regions of the T cell surface that either were or were not in contact with the surfaces of opposing APCs bearing agonist pMHC complexes. An example of a T cell contacting a pMHC-bearing APC is shown in **Movie 2.4**. For the studied regions within the immunological synapse ("IS") and outside ("non-IS") another representative synapse is shown in **Fig 2.5A**. We found that instantaneous coverage did not vary appreciably over the time-course of synapse development for either location and that IS versus non-IS regions were similarly dense for protrusions (**Fig 2.5B**). This suggests that T cells did not intensify their search for antigens upon antigen recognition. However, a cumulative plot revealed that, in the IS, the rate of surface contact saturation actually slowed down (**Fig 2.5C**). To capture this, we adopted a metric (T75%) that

reports the time at which 75% saturation of the contact is achieved, based on the 75% coverage point lying at the steep part of the contact saturation curve. In the example cell shown in **Fig 2.5A**, we found T75% was significantly faster (13.5 seconds) in non-IS compared to IS (25 seconds); and IS regions were slower to saturate as a class, compared to either isolated cells that were not making contacts with other cells or when comparing to non-IS regions in the same cells or synaptic regions without agonist pMHCs (**Fig 2.5D**).

We hypothesized that the reduced saturation rate in the IS was a consequence of some protrusions being stabilized as a result of ligand detection, thus leaving fewer protrusions to scan new areas. To assess dwell time via LLS imaging from the perspective of the "target", we developed an analytic method to analyze occupancy patterns at all the possible microvilli-sized (**Fig 2.6**) areas within a putative contact (**Fig 2.7A**). To extract how long such a region was continuously occupied by a T cell protrusion, we tracked the binary intensity of single-microvilli sized regions through time. A plot for a typical region is shown in **Fig 2.7B**, demonstrating times when microvilli passed through the region and exceeded a threshold of 50% coverage for just a single imaging timepoint (black arrow heads) or dwelled longer (grey arrow head). We plotted the average lifetime of all protrusions that were above the 50% cutoff for multiple cells and found similar lifetimes for isolated cells and for non-IS regions of cells that were engaging pMHC-bearing APCs (averaging 6.9 and 6.48 seconds respectively, **Fig 2.7C**). For IS regions of cells interacting with APCs in the absence of antigen, average dwell time was slightly longer (7.69 s). In contrast, average dwell times were the longest in the IS (8.9 seconds). We differentially color-coded protrusions in image sequences for an IS region, based on whether they visually persisted (**Fig 2.7D** and **Movie 2.5**)**.** This highlighted the more stable microvilli that ceased to scan as extensively in the IS. Such stable contacts were typically but not exclusively localized in the center of the contact.

Synaptic contact mapping (SCM) of TCR-mediated protrusion-stabilization in the IS

These LLS data suggest stabilization of contacts might occur as a stochastic result of global signaling or as a specific consequence for those that had ligated their TCRs. We thus sought to visualize TCR microclusters together with these protrusion structures. While LLS imaging had proved facile for full cell volumes, we sought a companion tracking technique based on total internal reflection fluorescence (TIRF) imaging as a means to increase the scanning rate at the IS and focus upon nanometer level measurements of the contacts. We also sought to simultaneously visualize membrane apposition together with TCR density. Thus, we analyzed T cells that were settled upon supported lipid bilayers containing pMHC and intercellular adhesion molecule 1 (ICAM-1)[1,50] to see if we could detect and thus study similar microvillar-like protrusions under these conditions. LLS imaging of fixed cells on bilayers (**Fig 2.8A** and **Movie 2.6**) also demonstrated that T cells generated microvillar-like projections. Scanning angle interference microscopy (**Fig 2.8B**) of T cells encountering lipid bilayers similarly confirmed that there were significant height variations of membrane for cells engaging lipid bilayers (**Fig 2.8C**). Notably bright TCR accumulations (microclusters) were closer to lipid bilayers as compared to the entire pool average, which is consistent with recent variable-angle TIRF studies showing TCR pre-enriched at microvillar tips[75] ICAM-1, a bigger molecule, was found farther away from the bilayer (**Fig 2.8B-D**).

To then study these contacts in real-time, we developed a method whereby quantum dots (Qdots), with a diameter larger than TCR-pMHC bond lengths, were seeded onto the lipid bilayers and used to specifically study close apposition on the scale of molecular interaction, akin to a "molecular ruler"[177] (**Fig 2.9A and 2.10A**). When T cells engaged bilayers containing ~16 nm Qdots, we observed "holes" in the otherwise uniform Qdot layer (**Fig 2.9B**) and found that intense TCR microclusters were inversely correlated with the Qdot intensity (**Fig 2.9B-C**).

We confirmed that the contact "holes" and inverse correlation with TCR were specifically seen with larger 16 nm Qdots, but were essentially lost when smaller (~13 nm in diameter) Qdots or rhodamine formed the fluorescent layer (**Fig 2.10B-C**). These exclusion zones were likewise revealed when Qdots were added after synapses had formed (**Fig 2.10E**), showing that the Qdots did not induce the structures. We termed this method synaptic contact mapping (SCM) and found that SCM "holes" had mean diameter of 541 nm (**Fig 2.10D**) as compared to LLS imaging which estimated the mean microvilli thickness at 535nm (**Fig 2.6**). Also predicted from LLS imaging, these contacts could be observed to form as cells first spread onto bilayers (**Fig 2.9D** and **Movie 2.7**) and occurred at consistent densities over time (**Fig 2.9E**). We also applied SCM in a multichannel format to co-track multiple molecules alongside Qdots. TCRs co-localized with holes/contacts (**Fig 2.9B**), while LFA-1/ICAM-1, which are larger molecular interactions, were excluded (**Fig 2.11**).

"Holes" in the Qdot distribution were mapped using automated image analysis (**Fig 2.12**) and not all contact regions contained significant accumulations of TCRs (arrows in **Fig 2.9B box-inset** and **Fig 2.9F**). To quantify this and to determine whether TCR-occupied protrusions had longer dwell times in the IS, we defined a cutoff based on background TCR intensity levels across the entire imaging field (**Fig 2.9F**) and thereby defined "TCR$^+$" versus "TCR$^-$" contacts. We used 20-second windows of analysis to limit observations of rebinding and found that whereas TCR$^-$ SCM "holes" had a mean lifetime of 3.7 seconds, TCR$^+$ SCM sites were stable for an average of 11.1 seconds (**Fig 2.9G**). Additionally, 25% of TCR$^+$ SCM sites were stable for the entire observation period whereas none of the TCR$^-$ contacts persisted. While we have long recognized stabilized TCR microclusters as a feature of a signaling interface, this analysis reveals an additional ongoing search of the opposing surface that continues to take place, apart from microclusters (**Fig 2.9H** and **Movie 2.8**).

SCM also allowed us to study how 3D membrane dynamics underlie some of the movements of TCR microclusters that have previously been described[50,53]. We used kymographs of TCR

tracks to show an exact correspondence between complex TCR movements and the movements of the underlying 3D protrusion (**Fig 2.9I)**, and similarly for microclusters of the proximal kinase ZAP-70 (**Fig 2.9J**), showing that these movements are taking place in association with a stably surface-anchored projection. But, protrusions could also be seen to have more complex merging dynamics, which could result in conglomeration of TCR microclusters when both of the merging contacts were previously occupied (**Movie 2.9**). Merging took place even when only one (**Movie 2.10**) or neither contact contained an evident TCR microcluster, and microclusters themselves could both split and merge (**Movie 2.11**). Notably, contacts were also observed in SCM images for B cells, macrophages, and dendritic cells (**Movie 2.12**) with different patterns, suggesting other immune cells survey the opposing surface with different strategies.

Actin cytoskeleton and signaling independence of TCR-mediated protrusion-stabilization

This data provided a framework for correlating membrane protrusion stability with TCR aggregation, and we sought to understand whether signaling and ensuing actin assemblies were required for modulating that stability. To assess this, we first used ZAP70 analog-sensitive[178] OT-I T cells, for which a specific kinase-inhibitor blocks signaling through the proximal kinase in TCR signaling. We found that although drug treatment fully blocked TCR-induced calcium signaling[178] (**Fig 2.13A**), both microvillar probing and microcluster accumulation in stabilized contacts was at least as robust as in the absence of signaling (**Fig 2.13B-C** and **Movie 2.13**). Similarly, complete inhibition of all tyrosine phosphorylation with Src-family kinase inhibitor PP2 did not block microvillar scanning **(Fig. 2.14A)**. In the absence of pMHC (ICAM-1 only on bilayers), "holes" were observed by SCM (**Fig 2.13D**) and moved retrograde to the direction of cell migration (**Fig 2.13E-F**). Furthermore, stabilization was specific to agonist-bearing complexes and null pMHC did not stabilize contacts (**Fig 2.13G**). While it has previously

been observed that tyrosine kinase signaling is not necessary for microcluster aggregation[179], this result shows that cells continue to form microvilli, probe the surface and that TCR occupancy converts these protrusions to long-lived contacts.

To explore this further, we tested the role for the actin cytoskeleton in stabilized contacts. Treatment of recently established synapses with Latrunculin B (LatB), which sequesters actin, results in actin disassembly, elimination of microvilli (**Fig 2.14B**), and the overall loosening of the cell cortex away from the bilayer, as visualized by a decreased interference reflection microscopy (IRM) signal (**Fig 2.15A and Movie 2.14**). However, the number of TCR microclusters remained steady after LatB addition even as the number of total contacts decreased to approximate the number of microclusters (**Fig 2.15B**). Plotting the probability of "occupancy" of a contact with a microcluster showed that actin depolymerization increased this probability; TCR$^+$ contacts were selectively retained over time (**Fig 2.15C**, see also zoom in **Fig 2.15A**), both in a single cell and when viewed over many examples (**Fig 2.15D**). Consistent with this observation, we compared actin localization relative to these contacts in early (< 3 minute) synapses with late (> 6 minute) synapses in which actin depolymerization clears the majority of the central synapse[50,167,180]. Whereas early contacts contain high densities of nucleated actin, the actin-void regions in later contacts, particularly of the central synapse, also supported contacts, which is consistent with their existence being actin-independent (**Fig 2.15E-H**). This confirms previous reports that showed actin to be dispensable for existing microclusters to persist[53] and that polymerized actin can be found at early sites of TCR signaling[179]. However, it puts those findings in context of clear requirements for actin in most 3D contacts being compensated by the presence of TCR microclusters.

Discussion

While clustering of TCRs has long been proposed to represent a fundamental signaling unit[40,181], here we see that neither signaling nor cytoskeletal attachment were required for TCR microclusters to complete the search process and capture a membrane contact. It is intriguing that estimates for microvilli dwell times in the absence of ligands was ~3.5-6 seconds, depending on the method used to measure them in this study, because that range is long enough to discern short–lived antagonists (typical $t^{1/2}$ of ~2 seconds) from longer-lived agonist pMHC-TCR complexes[182]. Variations in that estimate from LLS to SCM methods may represent the sensitivity of the methods (e.g. with SCM-based tracking of a low intensity signal being susceptible to possible "dropping" of a contact) and/or the effects of simplified bilayers as compared to complex cell surfaces. While others have recently described immediately-stable "close contacts"[45] formed on glass surfaces that uniformly induce signaling associated with exclusion of large molecules such as the phosphatase CD45, contacts with native ligands are more dynamic and we did not observe profound CD45 exclusion in most contacts excepting occasional late, central synaptic membrane contacts. A series of future questions will need to address how molecules distribute at very small size scales on these tips but the ultimate result may resemble recently described micro-synapses[183]. We also speculate that dynamic microvilli are the 3D structure on which previously described lipid rafts or "islands" are assembled, since islands have similar dimensions to microvilli, and that the movements and concatenations we describe on 3D surfaces are those on which such islands may merge or split[54]. Addressing this will require further improvements in microscopy for multi-color LLS at higher frame rates.

This work shows that a topographic scan, or "palpation" of the opposing surface, underlies the act of TCR recognition and defines a key parameter in cell-cell recognition, namely the time pressure for ligands to solidify interactions with an opposing surface. Given that ligand density is tightly regulated in most biological systems, different cells are expected to take different approaches to this problem. We note that different immune cell types appear to survey more or

less actively as compared to T cells and sometimes with waves or other patterns of membrane movements that are likely to lead to different efficiencies. Multiple additional levels of regulation of this process are now open to study.

Figures
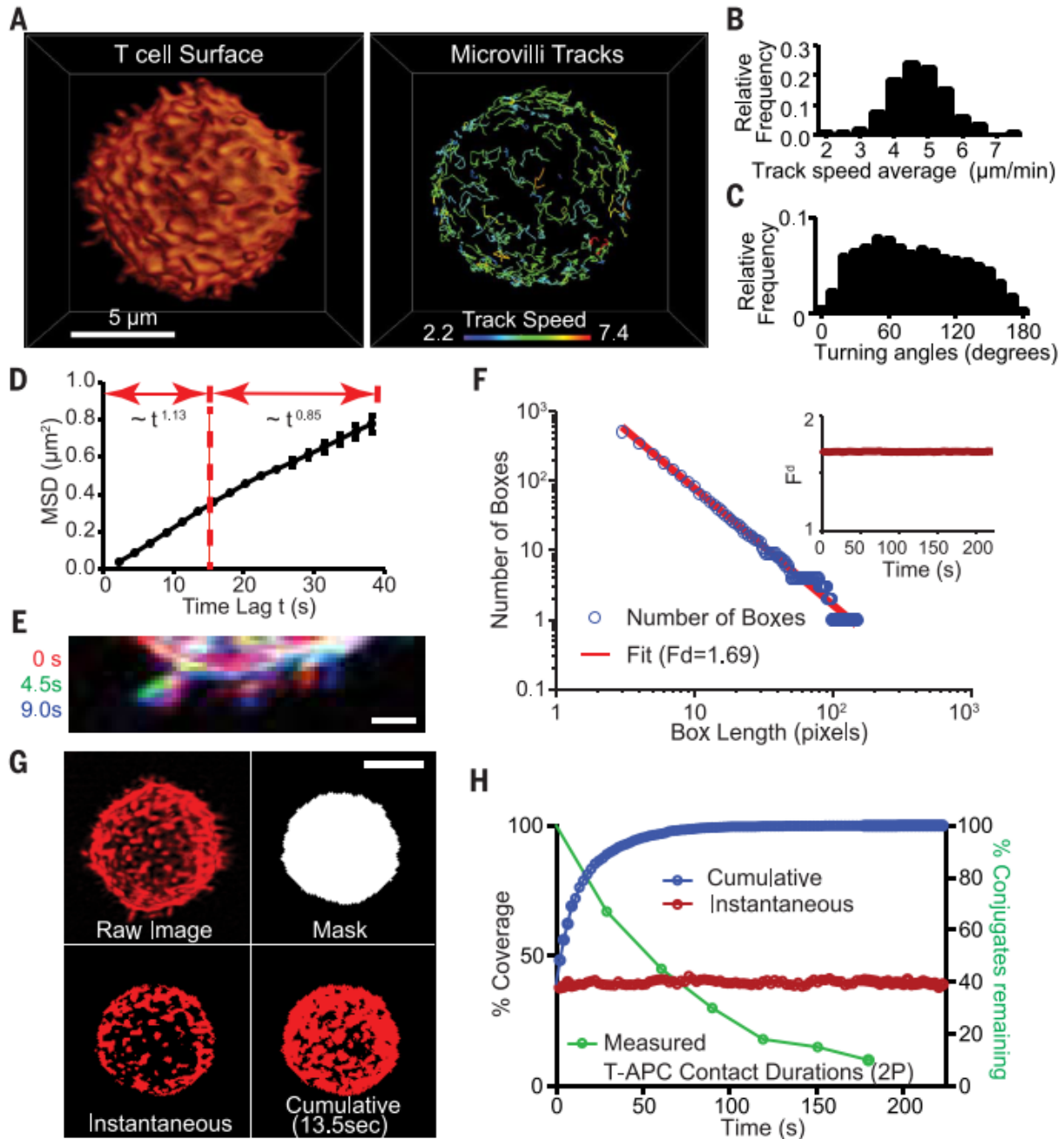
Figure 2.1. Effective surface scanning by T cell protrusions.
(A) Surface projection rendering of a mouse T cell imaged by LLS (left). Isolated tracks for individual microvilli (right). See also **Movies 2.1, 2.2.** Tracking was assisted in some cases by image stabilization, to account for modest cell drift (**Fig 2.4A**). **(B)** Track speeds, **(C)** Turning angles and (**D**) MSD for microvilli (n>232 microvilli for all timepoints, across 3 cells). The curve follows the power law of MSD~t^{α}, for t < 15 s, α = 1.13; and for t > 15 s, α = 0.85. Error bar corresponds to the standard deviation (SD). **(E)** Three-color overlay of a sub-section of an isolated T cell at three time points. Scale bar: 1 micron. **(F)** Fractal analysis: plot of the number of boxes needed to cover the active area of a T cell vs. length of the box (L). The slope of the fit

24

line is used to determine the fractal dimension (F_d). Inset: F_d over time for a single T cell. **(G)** Representation of the masking and threshold method used to calculate the instantaneous and cumulative coverage of T cell surfaces and IS ROIs. Anti-CD45 was used to label cell surfaces in this example. Scale bar: 5 microns. See also **Movie 2.3**. **(H)** Left axis: Percentage of surface coverage (cumulative in blue, instantaneous in red) of an isolated T cell throughout time from LLS in vitro. Right axis: Percentage of T-APC contacts remaining vs. time, from 2-photon imaging data in vital lymph nodes.
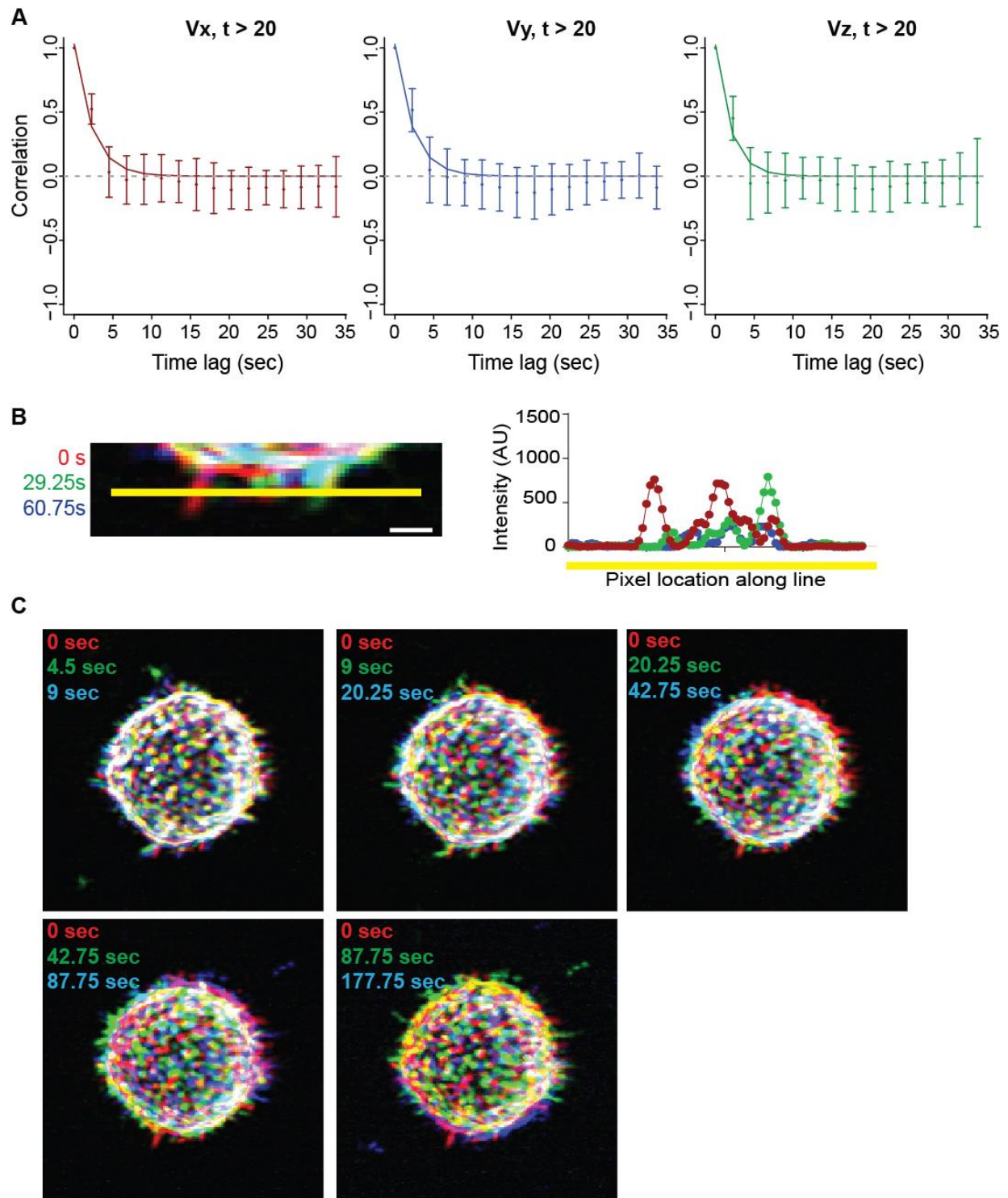
Figure 2.2. Autocorrelation of microvilli velocities and three-timepoint 'discoball' overlay of microvilli dynamics.

(A) Autocorrelation of microvillar velocities in Vx, Vy and Vz for trajectories that lasted equal to or longer than 20 seconds (N = 27 microvilli). Data points are shown as dots with error bars (mean ± SD). Positive regime of the autocorrelation function is compared to an exponential curve (shown as solid lines). Whether data decays slightly slower than exponential decay is

unknown due to lack of time resolution. **(B)** Left: Three-color overlay of a sub-section of an isolated T cell at three time points. Identical to text Figure 1E but sequence is over an extended timeframe (60.75 seconds). Right: Plot of the intensity at each pixel across the yellow line in the left image. Scale bar: 1 micron. **(C)** Full cell version of the overlay displayed in Figure 1E & S2B (left). The indicated time periods were overlaid to further display the dynamic nature of the cell surface.
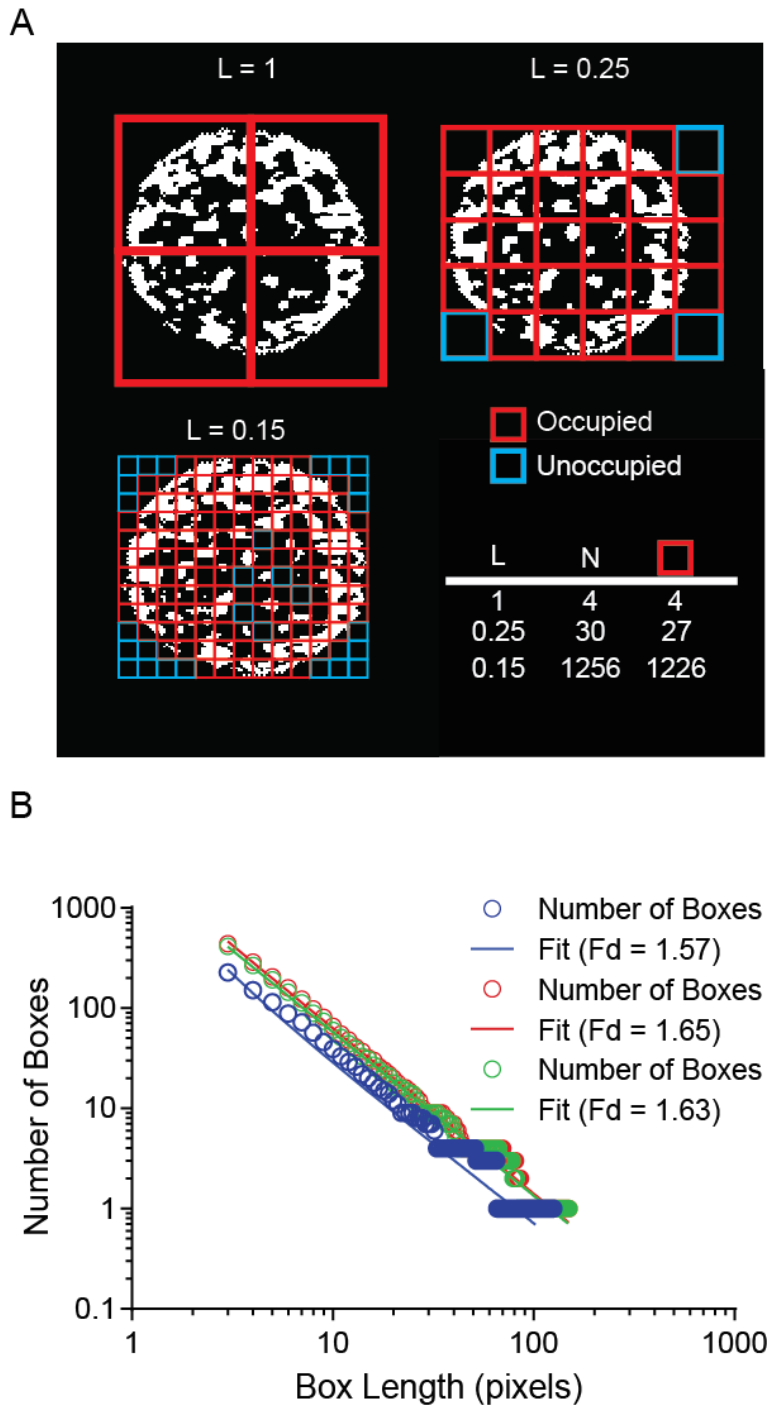
Figure 2.3. Analysis of fractal dimension for microvillar coverage centered on a randomly selected cell face.
(A) A visualization of how the fractal dimensions is calculated at each timepoint. The plot in Figure 1F and (B) is created using the number of occupied boxes vs the length of one side of the box. **(B)** Fractal Dimension calculated for 3 individual T cells.
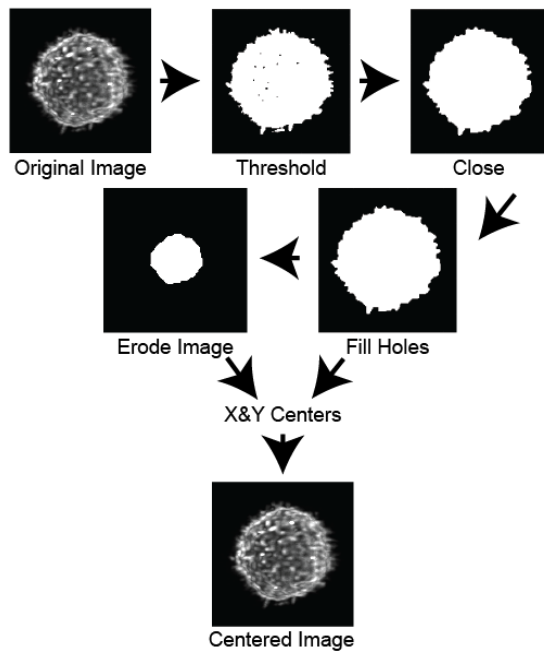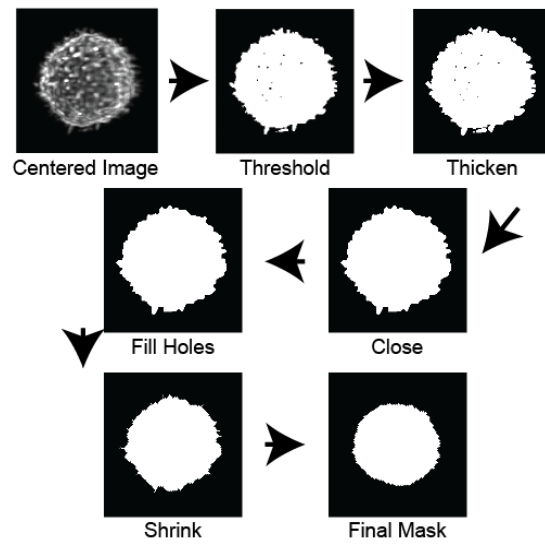
Figure 2.4. Analysis methods used with LLS microscopy.
(A) Visualization of the scheme used to stabilize maximum intensity projection movies for further analysis. **(B)** Visualization of the process to create a mask to isolate ROIs from LLS data for further analysis.
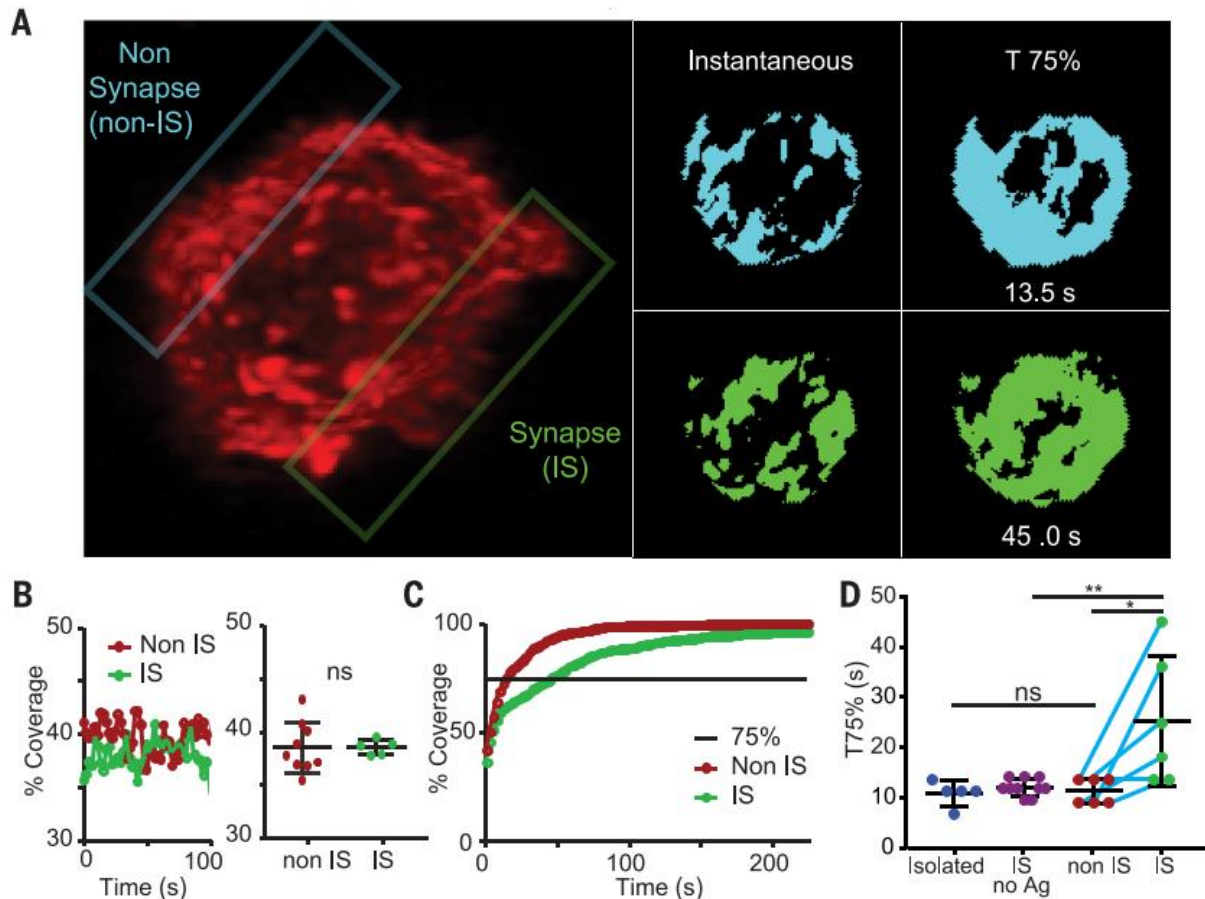
Figure 2.5. Altered microvillar cumulative coverage in response to ligand detection.
(A) Left: Image of a T cell in interaction with a peptide-loaded APC (unlabeled). The non-synaptic (non-IS) plane of interest is outlined in blue, the synapse (IS) is outlined in green. (See also **Movie 2.4** for another example of an immunological synapse formed between a T cell and an APC with both cells labeled.) Right: Thresholded images of the non-IS (blue) and IS (green) contact face at a single timepoint and a cumulative image when coverage had reached 75%. **(B)** Left: Percent surface coverage throughout time for a non-IS and IS region of a single T cell. Right: The distribution of average surface coverage for non-IS regions and IS regions taken from multiple T cells. Error bar corresponds to SD, data are pooled from 4 separate experiments. **(C)** Percent cumulative coverage comparing the non-IS and IS region of a single T cell. Line indicates 75% surface coverage. **(D)** Comparison between the distributions of T75% for isolated T cells, IS regions with no antigen, non-IS regions, and IS regions of multiple individual T cells. Error bar corresponds to SD, data are pooled from 4 separate experiments. The significance test was unpaired t-test.
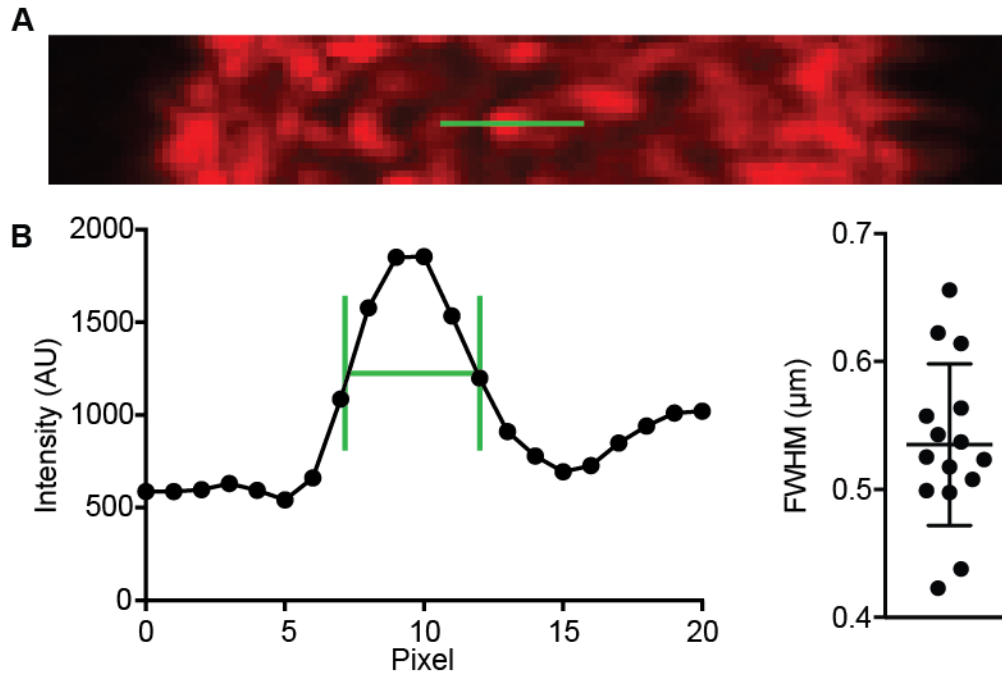
Figure 2.6. Measurement of microvilli dimensions from LLS microscopy.
(A) Example of a protrusion width measurement. The pixel intensity is recorded across the green line. **(B)** Left: A plot of the pixel intensity vs the pixel position on the green line in (A). The green lines represent the full width at half maximum (FWHM) of the protrusion. Right: The distribution of the FWHM values of protrusions on the cell surface. Error bar corresponds to the standard deviation.
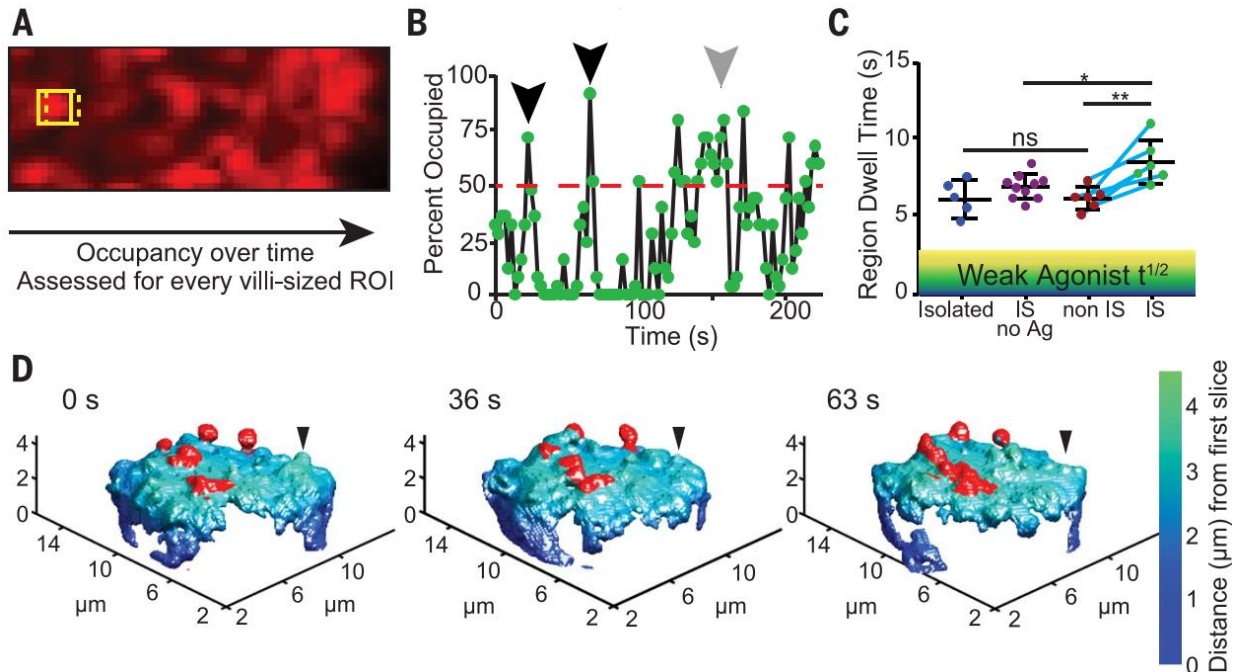
Figure 2.7. Altered microvillar regional dwell time in response to ligand detection.
(A) The scanning method for measuring regional dwell time over a contact surface. **(B)** Variation in occupancy, measured for a 25-pixel sized area, illustrating a cutoff at 50% occupancy. Short-lived protrusions are highlighted with the black arrows, while a longer-lived scanning event is shown in gray. **(C)** A comparison of the average regional dwell time, defined as in (B), for isolated T cells, IS with no antigen, non-IS regions, and IS regions in different T cells. Teal line connects individual cells. Shaded regions denote generalized half-life for weak-agonist pMHCs. Error bar corresponds to SD, data are pooled from 4 separate experiments. The significance test was unpaired t-test. **(D)** Membrane topology of the synaptic region of a T cell, labeled with anti CD45-Alexa488, interacting with a peptide-loaded APC at various timepoints. Stable protrusions are highlighted in red, an example transient protrusion is indicated with a black arrowhead.

A Bilayer/Lattice Light Sheet Imaging

5 µm

+0.0 µm

+0.4 µm

+0.8 µm
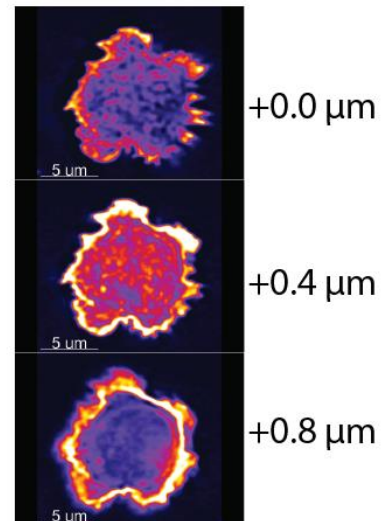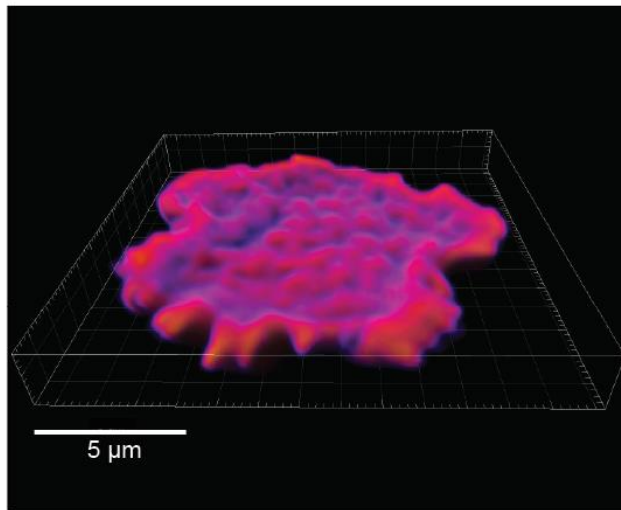
B Bilayer/Scanning Angle Interference Microscopy (SAIM)

C

D
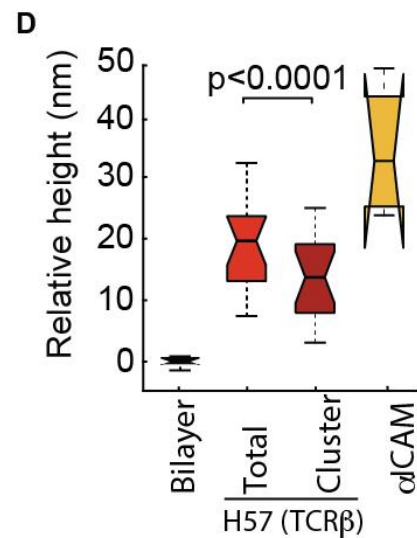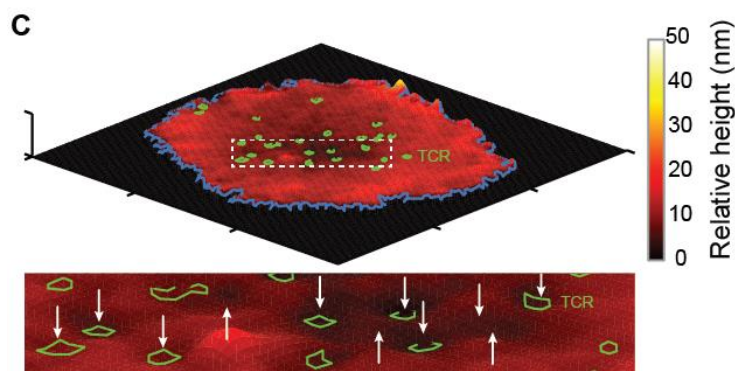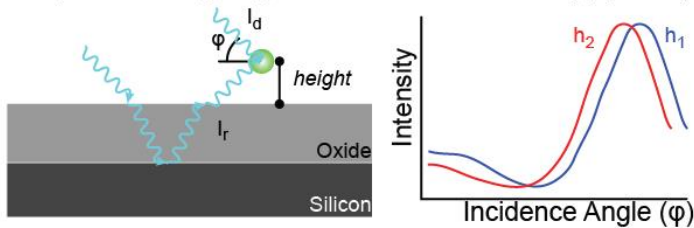
Figure 2.8. T cells on supported lipid bilayers form microvillar-like palpations.
(A) Surface rendering of lattice light sheet imaging of a T cell on an activating lipid bilayer
viewed from the coverslip. OT-I T cell blasts labeled with anti-CD45-Alexa647 were seeded on
bilayers containing ICAM-1 and SL8-Kb pMHC complexes and allowed to settle prior to fixation
and LLS imaging. See also Movie S4. Left panel shows an IS formed by a T cell on the lipid
bilayer, with the IS facing up in the image. The right panels show cross sections of the T cell at
different Z values. **(B)** SAIM imaging concept. Interference between the direct excitation light (I_d)
and the reflected excitation light (I_r) results in intensities that are a function of the scanning
angle and the axial position of the fluorophore (right). **(C)** SAIM height image projection of TCRs
in an OT-I IS. TCR microcluster boundaries are marked in green. Tick spacing: 5 µm. Heights
are pseudocolored according to the color bar at right. Boxed region shown magnified 4× at

bottom. Arrows in boxed region point to deformations in the membrane. **(D)** Box plot of average heights of all TCR fluorescence, microcluster-associated TCR fluorescence, lipid bilayers and clustered LFA-1. The average lipid bilayer height was set to 0. P < 0.0001 by paired t-test, N = 50 cells pooled from 3 independent experiments.
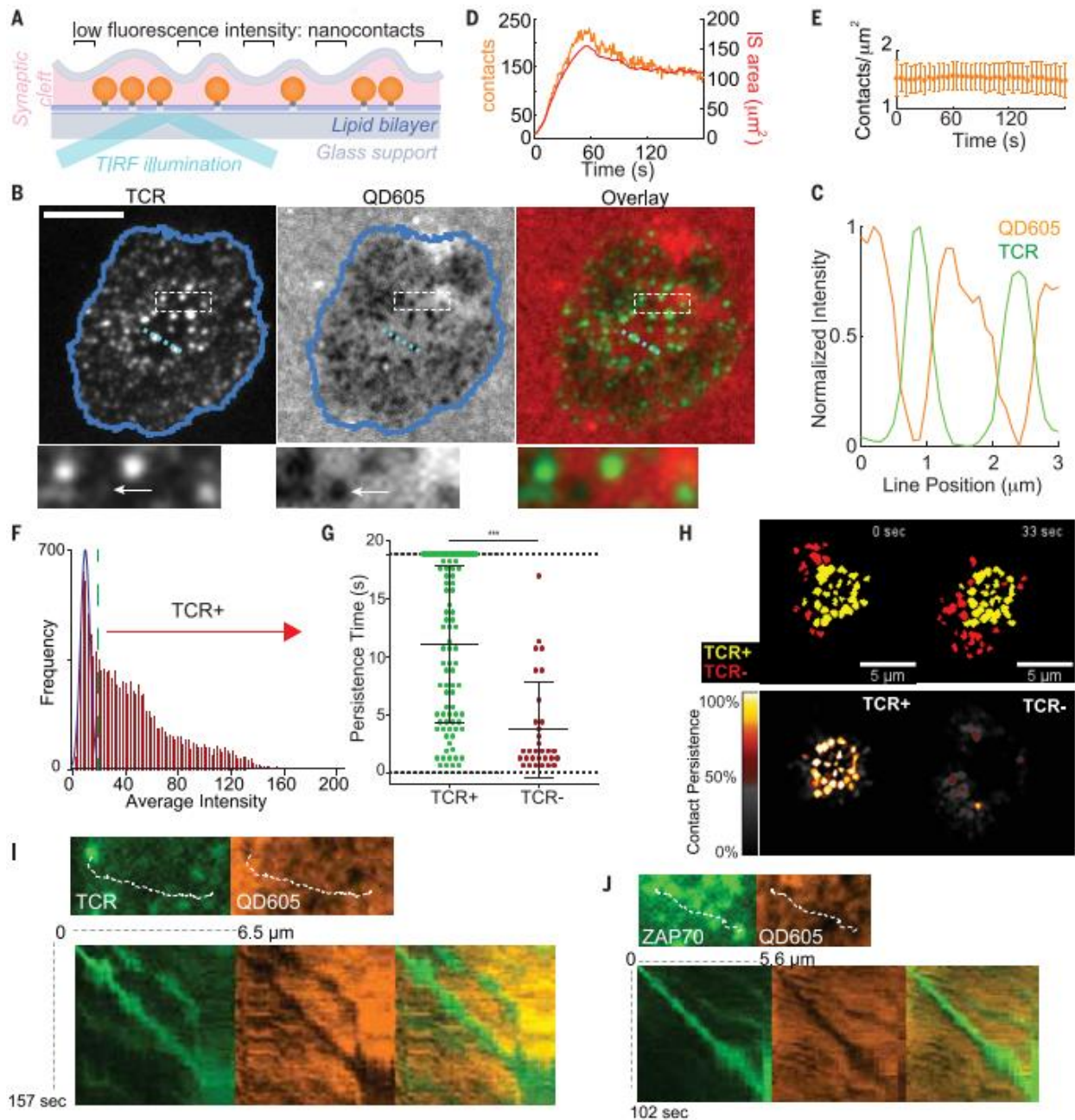
Figure 2.9. TCR-occupied projections are stabilized.
(A) Schematic representation of bilayer-bound Qdots for SCM based imaging. Qdots larger than the ~ 15 nm TCR-pMHC length are excluded when membranes closely appose. See also **Figure 2.10-11. (B)** Images of TCR, bilayer-bound QD605 streptavidin conjugates, and TCR/streptavidin overlays from cells fixed during synapse formation. Scale bars: 5 microns. Dashed box region is shown at the bottom. Arrow points to a contact with no apparent TCR microcluster. **(C)** Normalized intensities of Qdot605 and TCR line scan for the light blue line in (B). **(D)** Number of contacts and total IS area during IS formation. **(E)** Average contact density over time during IS formation. Error bars correspond to SD. Plot represents 28 cells pooled from 7 independent experiments. **(F)** Frequency histogram of the average intensity of all the contacts throughout the observation period. The blue Gaussian curve represents the intensity distribution expected from background sources for this region of interest. The green dashed line represents

the cutoff from TCR$^+$ to TCR$^-$. **(G)** Dwell times in the TCR$^+$ and TCR$^-$ populations within an 18.9 s observation window. Error bar corresponds to SD. The significance test was unpaired t-test. **(H)** Top: Overlay of TCR$^+$ (yellow) with the TCR$^-$ contact populations (red) at 2 different timepoints. Bottom: Time projection of TCR$^+$ (left) and TCR$^-$ (right). Colors represent the percentage of time of each pixel occupied by contacts over the length of the movie. **(I)** Top: Image of a nascent H57-labled TCR microcluster and corresponding contact image. Dashed line indicates the subsequent microcluster path. Bottom: kymograph generated from the microcluster path in each channel and overlay. **(J)** As (I) but for a ZAP70-GFP cluster.
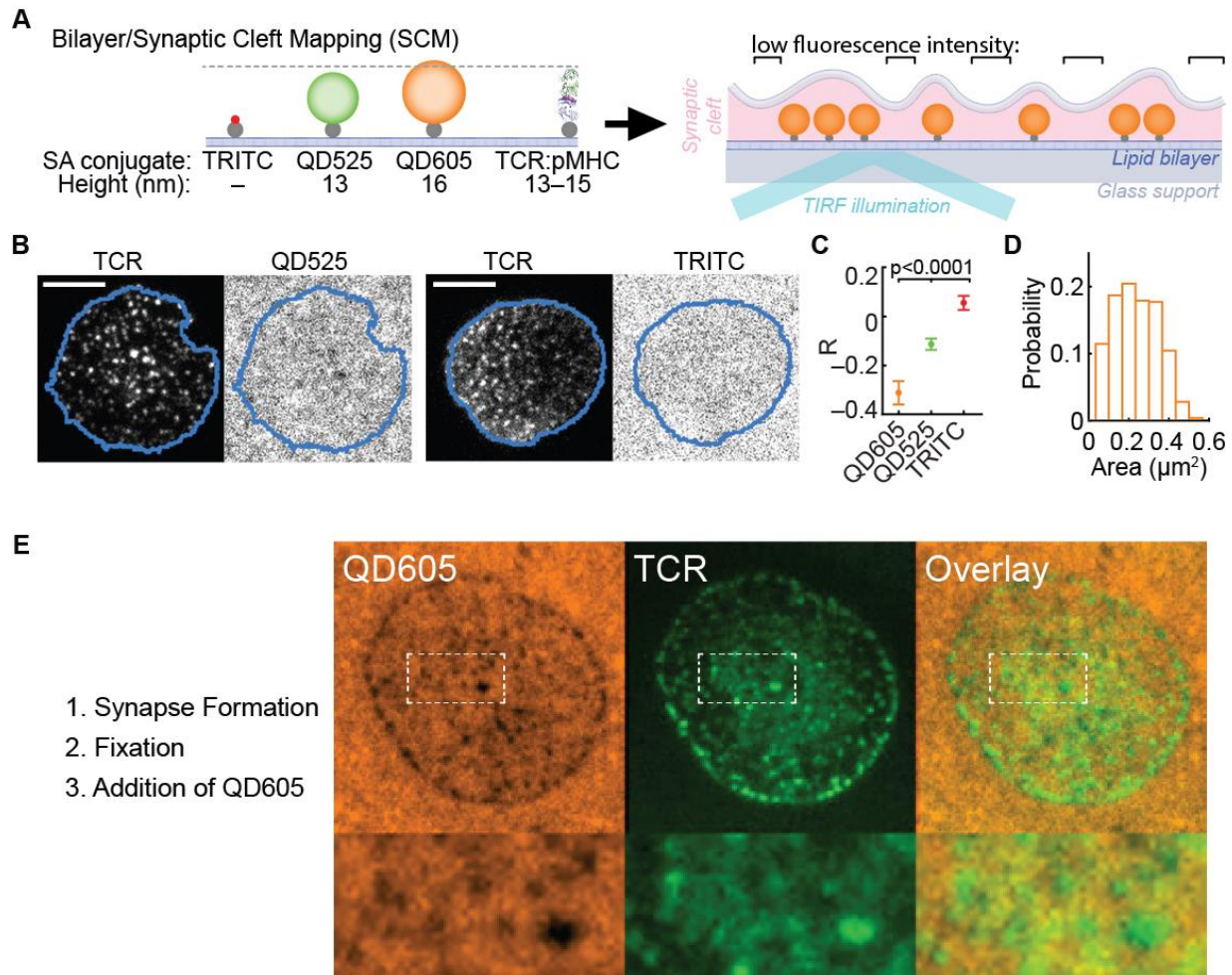
Figure 2.10. Synaptic Contact Mapping (SCM) microscopy principles and validation.
(A) Schematic comparison of TRITC-SA, QD525-SA, QD605-SA and TCR:pMHC. In SCM
Imaging, regions in which the synaptic cleft spacing is shorter than the diameter of the Qdots
will exclude the Qdots. Image series can be acquired to generate maps of synapse spacing
dynamics. The brackets denote the location of contacts—regions of tight synaptic cleft spacing
that exclude Qdots. **(B)** Images of TCRs, bilayer-bound QD525 streptavidin conjugates,
pseudocolored streptavidin intensity, and TCR/streptavidin overlays from cells fixed during
synapse formation. Scale bars: 5 µm. **(C)** TCR-streptavidin intensity correlations for the
indicated streptavidin conjugates. Plots represent the mean with 95% confidence intervals (CI).
N = 30–50 cells per streptavidin conjugate pooled from 3 independent experiments. Adjusted p
< 0.0001 for comparisons between each group (ANOVA, with Tukey's correction for multiple
comparisons). **(D)** Histogram of contact areas, quantified from SCM images. N = 31 cells pooled
from 2 experiments. **(E)** Post-fixation addition of Qdots to bilayers also highlights contacts.
QD605-streptavidin SCM and TCR TIRF images of an OT-I IS. Cells were allowed to bind to
bilayers and initiate IS formation before being fixed with PFA. The bilayer was then stained with
QD605-streptavidin and TCRs were stained with H57-597 conjugated to Alexa Fluor 488. Inset
region measures 5 × 2.5 µm.
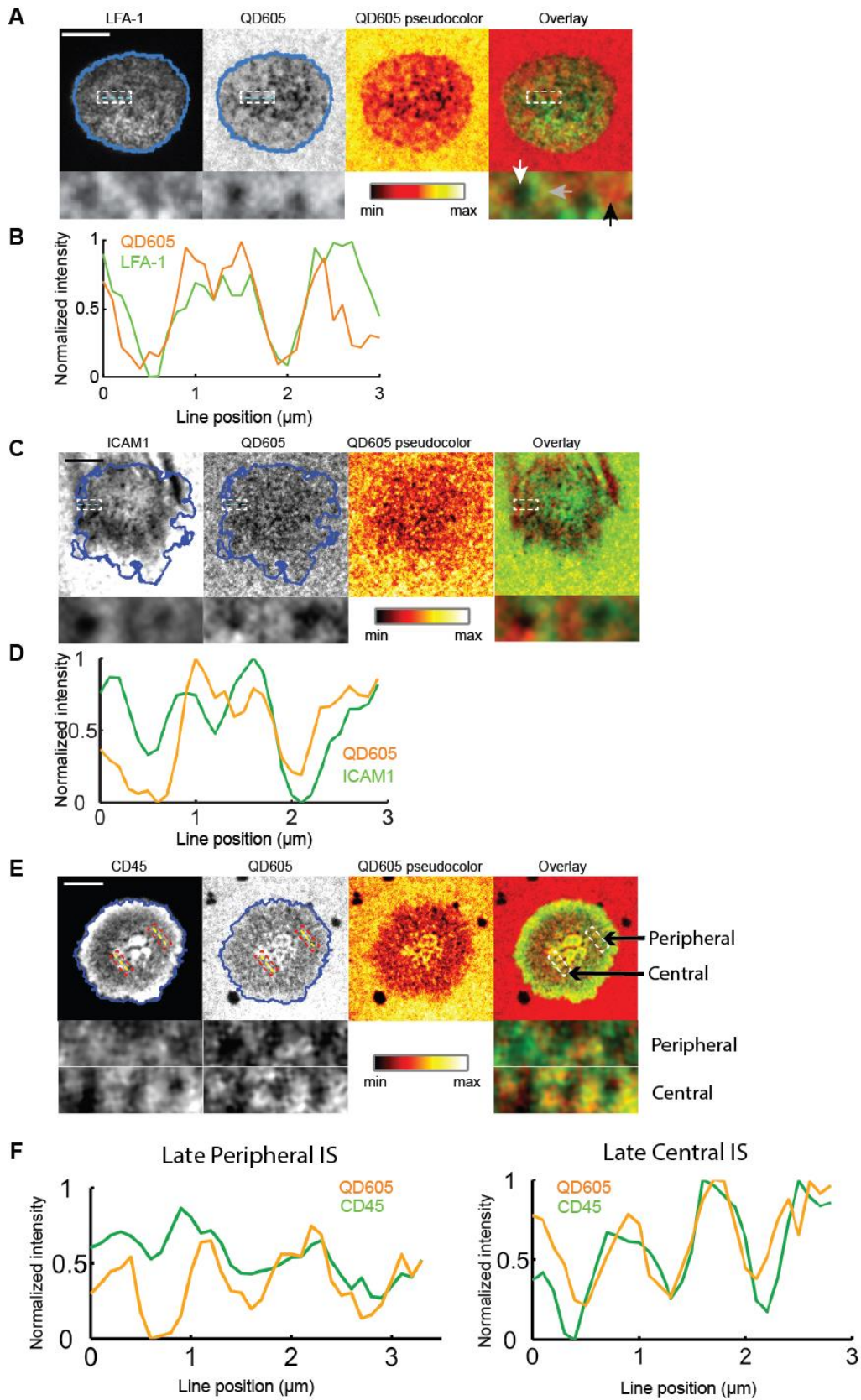
Figure 2.11. Molecular segregation relative to contacts.

SCM images of QD605 and TIRF images of:
(A) LFA-1, **(C)** ICAM, and **(E)** CD45 in OT-I IS formed on bilayers containing both ICAM and pMHC. Bottom images correspond to the boxed regions above. Scale bar: 5 µm. The zoomed-in region of overlay image in (A) shows an example of exclusion of LFA-1 from the contacts. Arrows over the lower-left inset image correspond to: a QD605-low intensity/LFA-1 low intensity region (white arrow), a QD605-high intensity/LFA-1 high intensity region (grey arrow), and a QD605-high intensity/LFA-1 low intensity region (black arrow). **(B), (D)** Normalized line scan intensity for the light blue lines in (A),(C) correspondingly. **(F)** Normalized line scan intensity for the yellow lines in central and peripheral regions in (E) which represents a late synapse in which CD45 is occasionally found to be excluded along with Qdots. Intensity was normalized for both the central and peripheral line scans showing that whereas CD45 is excluded from 'holes' in central regions, it is contained within them in peripheral contacts.
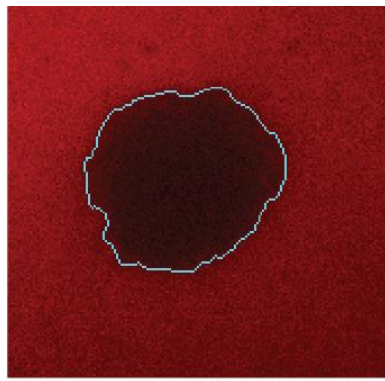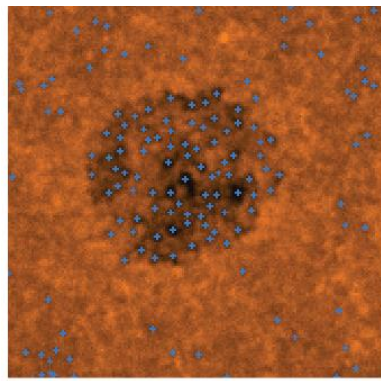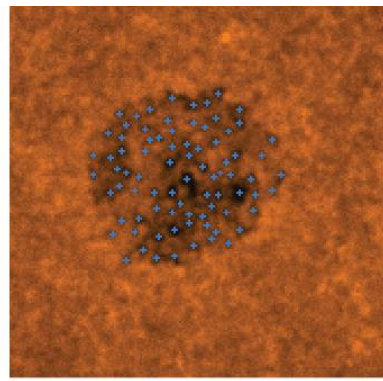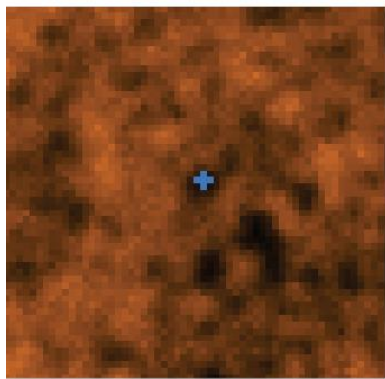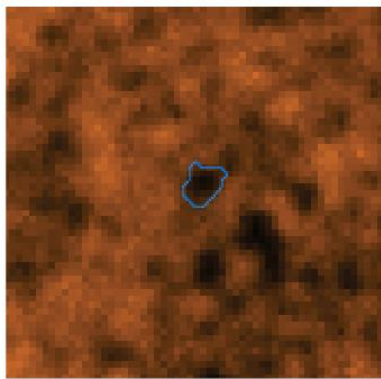
Figure 2.12. SCM contact segmentation.
The overall footprint of a cell on the bilayer is segmented from the IRM images using an active contour. Candidate contacts are identified as local minima, which are filtered to consider only minima within the cell footprint. Individual minima are dilated and used as seed points for the active contour algorithm to identify the borders of each contact.
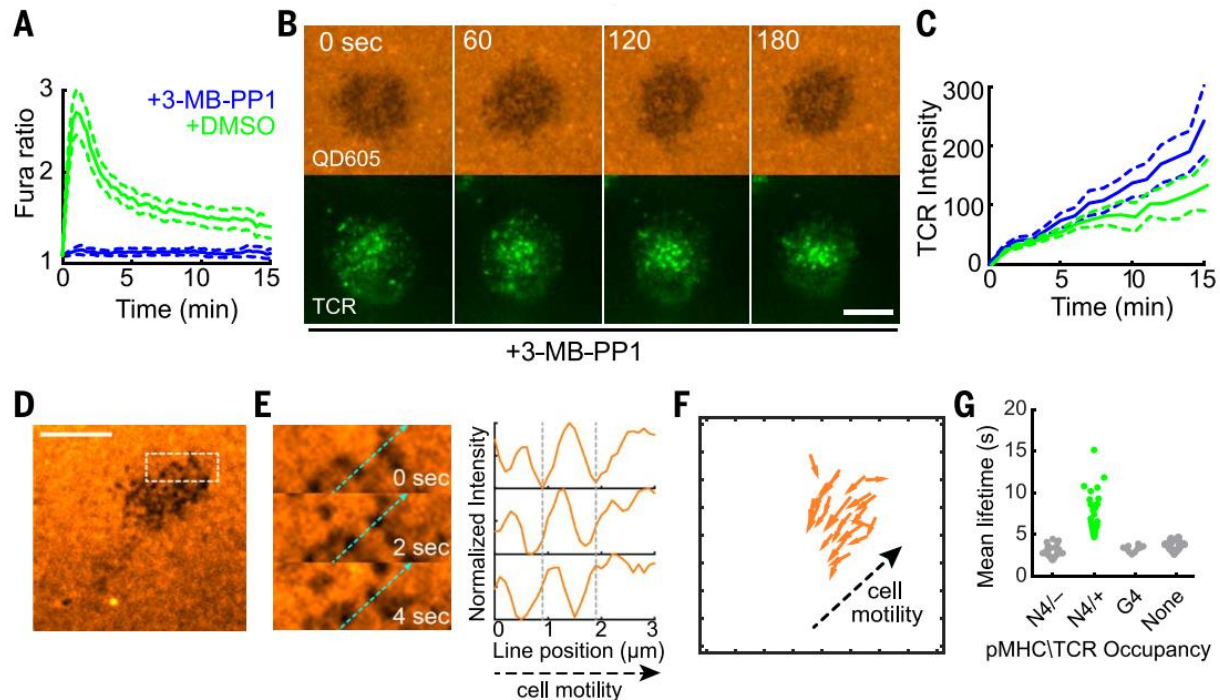
Figure 2.13. Signaling independence of TCR-mediated protrusion stabilization.
(A) Fura-2 calcium ratios measured in ZAP70(AS)/OT-I T cells on activating bilayers after treatment with vehicle or 10 μM 3-MB-PP1. Plots represent the average Fura-2 ratio measured in over 100 cells pooled from 2 separate experiments. Error bar corresponds to the 95% CI. **(B)** QD605-streptavidin and TCR TIRF time lapse images of ZAP70(AS)/OT-I synapses after treatment with 10 μM 3-MB-PP1. Scale bars: 5 microns. **(C)** TCR intensity in contacts in ZAP70(AS)/OT-I T cell synapses. 3-MB-PP1: N = 12; DMSO vehicle: N = 9 cells. Data is pooled from 3 experiments. Error bars correspond to the standard error of the mean. **(D)** SCM images of bilayer-bound QD605-SA during encounter of OT-I T cell, without bilayer-bound pMHC but with ICAM-1. Scale bar: 5 μm. The boxed region measured 5 μm × 2 μm. **(E)** Left: Boxed region shown in (D). Light blue dashed line indicates direction of cell motility. Right, normalized intensity line scans for the light blue dashed line shown at left. The vertical gray dashed lines correspond to the starting point along the line for two contacts. The contacts moved against the direction of cell motility. **(F)** Displacement vectors for contacts shown in (D). For clarity, only tracks longer than 1 μm are shown. **(G)** Mean lifetimes for contacts based on the bilayer-bound pMHC complex and TCR occupancy. For the N4, the contacts are categorized based on whether it acquired TCR microclusters. For the G4 and null conditions, TCR+ microclusters were not observed. Data are pooled from at least 3 separate experiments for each condition.
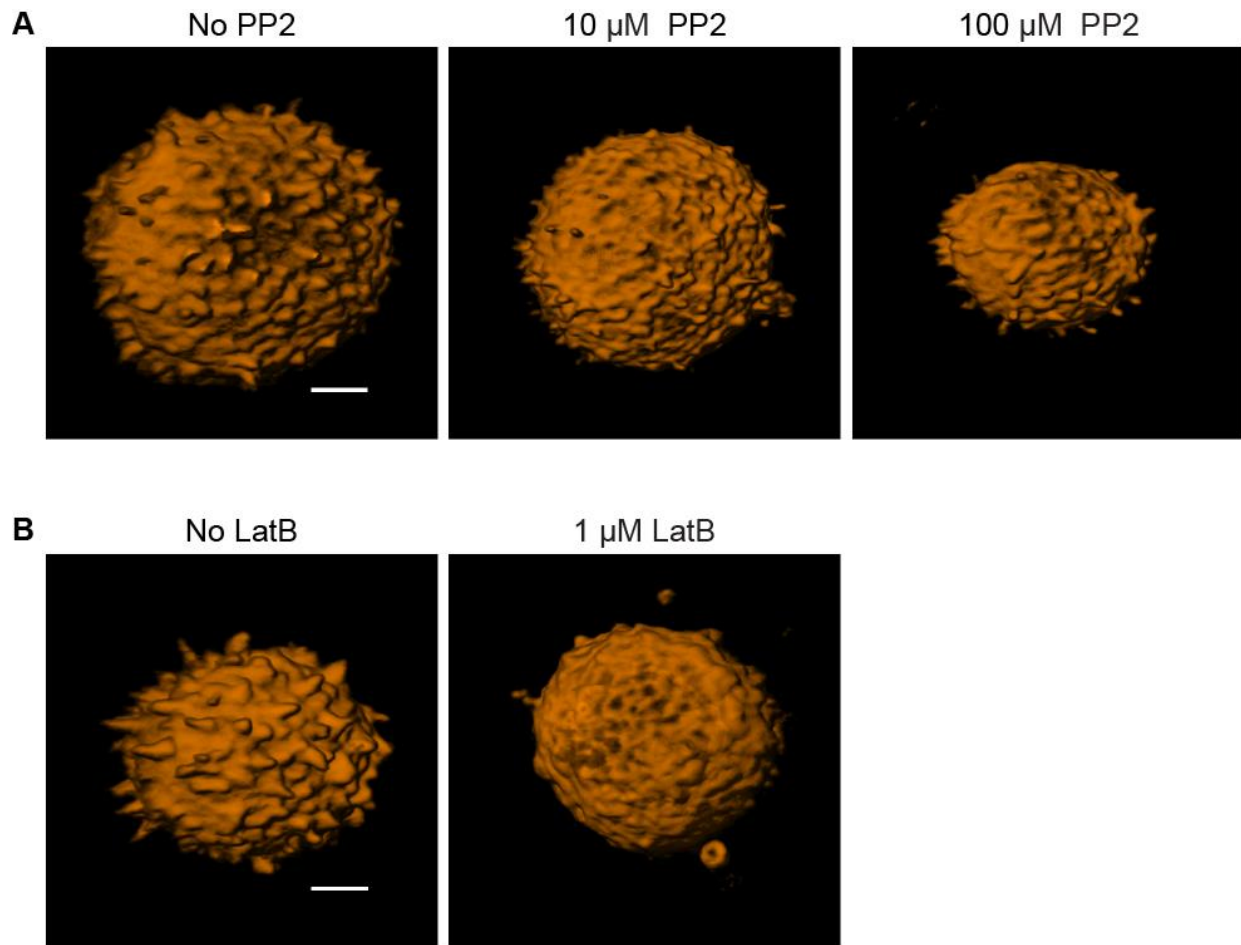
Figure 2.14. Surface morphologies of T cells with Latrunculin and PP2 treatments.
(A) Left panel shows an untreated T cell imaged by lattice light sheet microscopy. Central and right panels show images of T cells pretreated with, and imaged in media containing 10 µM and 100 µM PP2, respectively. Microvilli were present on the surfaces of these T cells. Scale bar: 3 microns. **(B)** Left panel shows an untreated T cell imaged by lattice light sheet microscopy. Microvilli were observed on the surface of this cell. Right panel shows a T cell imaged in media containing 1 µM Latrunculin B. Microvilli were reduced on this cell, resulting in a "smoother" cell surface. Scale bar: 3 microns.
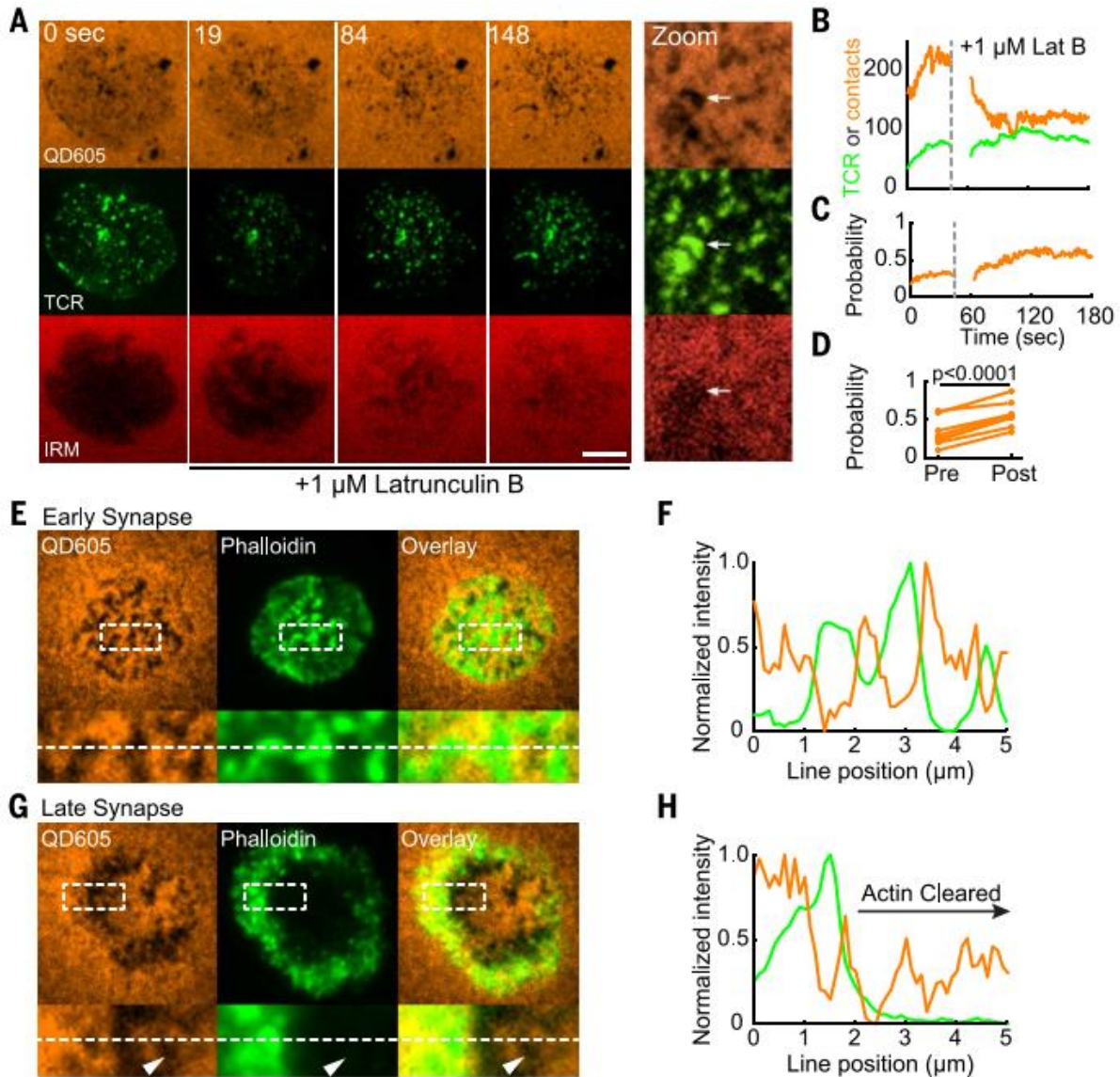
Figure 2.15. Cytoskeletal independence of TCR-mediated protrusion stabilization.
(A) Bilayer-bound QD605-streptavidin, TCR and IRM time lapse images of an OT-I IS during Latrunculin B (LatB) challenge. 1 μM LatB was added after acquisition of the t = 0 sec image. Scale bar: 5 microns. At right, a zoomed view of a region of the synapse 3 minutes after LatB addition. The white arrow points to a remaining patch of contacts with TCR microclusters and low IRM intensity. **(B)** Number of contacts (orange) and TCR microclusters (green) before and after LatB challenge for the IS shown in (A). **(C)** The fraction of contacts occupied by TCRs before and after LatB challenge for the IS shown in (A). **(D)** Average fraction of contacts occupied before and after LatB treatment. Each plot point represents the average fraction of contacts occupied in a cell measured over the 60 seconds before (pre-) and after (post-) LatB treatment. N = 7 cells pooled from 3 independent experiments. The significance test was paired t-test. **(E,G)** Top: QD605-streptavidin SCM and Phalloidin TIRF images of OT-I IS on activating bilayers. IS in (E) was fixed 3 minutes after addition of the cell to the bilayer. IS in (G) was fixed after 6 minutes and represents a mature synapse. Bottom: images of inset regions from images at top. Inset regions measure 5 μm × 2 μm. Images are representative of at least 25 cells imaged in 3 independent experiments. **(F,H)** Normalized line scan intensities for the dashed white line at bottom in (E) and (G), respectively.

43

Supplemental Files

Movie 2.1. Microvillar dynamics in T cells – Surface.

Surface projection of an OT-I T cell labeled with anti-CD45-Alexa488 and imaged by LLS microscopy. Time resolution is 2.25 s. For this movie, the cell's position in space was stabilized using the center of mass.

Movie 2.2. Microvillar dynamics in T cells – Maximal intensity projection.

Maximal intensity projection of an OT-I T cell labeled, as a result of membrane-tomato expression from the mTmG allele in the absence of Cre expression and imaged by LLS microscopy. Time resolution is 2.25 s. Movie suggests the protrusion size and dynamics are not affected by labeling method.

Movie 2.3. Saturating coverage by ongoing microvillar scanning.

Time series movie of microvillar movement. Time resolution is 2.25 s. Top left: Maximal intensity projection of the cell surface. Top Right: selected region captured as a mask. Bottom left: application of a threshold to define instantaneous contacts. Bottom right: Logical OR movie of all timepoints up to and including the current, taken from the binary map of instantaneous contacts. Instantaneous and cumulative coverages were calculated from bottom left and bottom right results, respectively.

Movie 2.4. The immunological synapse formed between a T cell and an APC.

This movie shows an IS formed between a T cell and an APC captured by time-lapse LLS microscopy. For synapse side view, the T cell, labeled with anti-CD45-Alexa488, is shown in red; the APC (BMDC), labeled with DiD, is shown in green. The top-right panel shows the en face view of this synapse. The lower-left panel shows a 3D surface of the synapse rendered in Imaris. The lower-right panel shows the synapse with the z scale color coded.

Movie 2.5. Stable and labile protrusions in an IS revealed by LLS imaging.

Membrane topology of the synaptic region of a T cell, labeled with anti-CD45-Alexa488, interacting with a peptide-loaded BMDC at various times. Visually identified stable protrusions are highlighted in red. Time resolution is 4.16 s.

Movie 2.6. T cells forming IS on an activating lipid bilayer imaged by LLS microscope make multiple microvillar-like contacts.

Movie created from 3D view of OT-I T cells interacting with an activating lipid bilayer imaged by the LLS microscope. OT-I T cells were labeled with anti-CD45-Alexa647, allowed to interact with lipid bilayer before fixation and imaging**.**

Movie 2.7. SCM time-lapse imaging of IS contacts and TCRs.

Movie created from QD605-streptavidin SCM and TCR TIRF images of an OT-I synapse during spreading on an activating bilayer. The borders of the identified contacts are indicated by the blue (left) and magenta (right) lines. The movie then pauses, zooms in on a region and continues to highlight TCR accumulation within a newly formed contact. Arrows during pause period point to the nascent contact that then fills with TCRs. TCRs were stained with Alexa Fluor 488-conjugated H57-597 anti-TCRβ. Full movie region measures 16 μm × 16 μm. Zoomed region measures 4 μm × 4 μm. Elapsed time is 23 seconds in the first segment, then 28 seconds in the zoomed segment. Original acquisition rate was 1 frame/sec. Movie is played at 6 frames/sec (6× real time).

Movie 2.8. Comparison of dynamic behaviors of TCR+ and TCR- contacts.

Overlay of the TCR+ contact population (shown in yellow) with the TCR- contact population (shown in red). Movie demonstrates the stability of the TCR+ compared to TCR- contacts.

Movie 2.9. SCM time-lapse imaging of IS TCR/contact merging dynamics for two contacts that are both TCR+.

Movie created from QD605-streptavidin SCM and TCR TIRF images of a region of an OT-I synapse formed on an activating bilayer. The borders of two TCR microcluster-containing contacts are indicated by the blue (left) and magenta (right) lines. As the movie plays, the two contacts move to the left and merge. TCRs were stained with Alexa Fluor 488-conjugated H57-597 anti-TCRβ. Initial region measures 12.5 μm × 12.5 μm. Zoomed movie region measures 3 μm × 3 μm. Total time elapsed is 28 seconds. Original acquisition rate was 1 frame/sec. Movie is played at 6 frames/sec (6× real time).

Movie 2.10. SCM time-lapse imaging of TCR+ and TCR- contacts merging.

Movie created from QD605-streptavidin SCM and TCR TIRF images of a region of an OT-I synapse formed on an activating bilayer. The borders of a TCR⁻ contact (left) and TCR microcluster-containing contact (right) are indicated by the blue and magenta lines. As the movie plays, the two contacts move to the left and merge. TCRs were stained with Alexa Fluor 488-conjugated H57-597 anti-TCRβ. Initial region measures 17.5 μm × 17.5 μm. Zoomed movie region measures 3 μm × 3 μm. Total time elapsed is 30 seconds. Original acquisition rate was 1 frame/sec. Movie is played at 6 frames/sec (6× real time).

Movie 2.11. SCM time-lapse imaging of contact splitting and merging dynamics.

Movie created from QD605-streptavidin SCM and TCR TIRF images of a region of an OT-I synapse formed on an activating bilayer. The border of a TCR microcluster-containing contact is indicated by the blue (left) and magenta (right) lines. As the movie plays, the contact and associated TCR microcluster split into a pair of contacts and microclusters. After translating inward for several seconds, the structures re-merge. TCRs were stained with Alexa Fluor 488-

conjugated H57-597 anti-TCRβ. Initial region measures 15 μm × 15 μm. Zoomed movie region measures 5 μm × 5 μm. Total time elapsed is 85 seconds. Original acquisition rate was 1 frame/sec. Movie is played at 6 frames/sec (6× real time).

Movie 2.12. SCM time-lapse imaging of surface contacts generated by multiple cell types demonstrates a diversity of search patterns.

Movies created from height projections of QD605-streptavidin SCM time lapse images of the T cell (OT-I T cell), B cell (CH27 B cell), macrophage (J774A.1) and dendritic cell (BMDC) interacting with ICAM-bearing lipid bilayers. Contacts were evident on all cells when interacting with bilayers. Movie regions measures 20 × 20 μm. Images are representative of at least 10 cells of each type from 3 independent experiments.

Movie 2.13. SCM time-lapse imaging of IS contacts and TCRs of a ZAP70(AS)/OT-I T cell during 3-MB-PP1 treatment.

Time-lapse movie of QD605-streptavidin SCM and TCR TIRF images of a ZAP70(AS)/OT-I synapse formed on an activating bilayer after treatment with 10 μM 3-MB-PP1 to inhibit ZAP70(AS). Top-to-bottom: TCR TIRF, QD605-streptavidin SCM and IRM images. TCRs were stained with Alexa Fluor 488-conjugated H57-597 anti-TCRβ. Movie region measures 14 μm × 14 μm. Total time elapsed is 257 seconds. Original acquisition rate was 1 frame/sec. Movie is played at 12 frames/sec (12× real time).

Movie 2.14. SCM time lapse imaging of IS contacts and TCRs during Latrunculin B challenge.

Time-lapse movie created from QD605-streptavidin SCM and TCR TIRF images of an OT-I synapse formed on an activating bilayer. Top-to-bottom: QD605-streptavidin, IRM and TCR images. TCRs were stained with Alexa Fluor 488-conjugated H57-597 anti-TCRβ. Movie region

measures 17.5 μm × 17.5 μm. Total time elapsed is 4 minutes. Latrunculin was added after ~45 seconds. Original acquisition rate was 1 frame/sec. Movie is played at 12 frames/sec (12× real time).

Materials and Methods

Mice

All mice were housed and bred at the University of California, San Francisco, according to Laboratory Animal Resource Center guidelines. Protocols were approved by the Institutional Animal Care and Use Committee of the University of California. mTmG mice[184] were used in the absence of a corresponding Cre allele, resulting in membrane-tomato expression in all cells. ZAP70AS mice were as previously described[178].

Cell culture and retroviral transduction

OT-I T cells were maintained in RPMI supplemented with 10% fetal bovine serum, 100 U/mL penicillin, 0.1 mg/mL streptomycin, 2 mM L-glutamine, 10 mM HEPES and 50 µM β-mercaptoethanol (complete RPMI). Single cell suspensions were prepared from the lymph nodes and spleens of OT-I TCR transgenic mice. Splenocytes were incubated in complete RPMI with 100 ng/mL of SIINFEKL peptide for 30 minutes at 37 °C. The splenocytes were washed three times and suspended in media. Lymphocytes and splenocytes were then mixed 1:1 at 2×10^6 total cells/mL, and 1 mL of the cell mix was transferred into each well of a 24-well plate. After 48 hours, 1 mL of media with IL-2 was added to each well (final concentration of IL-2: 100 U/mL). After 72 hours, cells were removed from the plate, transferred into fresh media with IL-2 and held in culture for an additional 24–48 hours before use.

For retroviral transduction, Phoenix cells were transfected with pCL-Eco and pIB2-Zap70-EGFP or pIB2-CD3ζ-GFP using Calcium Phosphate transfection. Supernatants were harvested and supplemented with IL-2. The supernatants were added to wells with T cells, and the plates centrifuged for 1 hour at room temperature. T cells were treated with supernatants from the

Phoenix cells 48 and 72 hours after stimulation and then transferred to fresh complete RPMI. Phoenix cells were maintained in DMEM supplemented with 10% fetal bovine serum, 100 U/mL penicillin, 0.1 mg/mL streptomycin, 2 mM L-glutamine, 10 mM HEPES and 50 µM β-mercaptoethanol (complete DMEM).

CH27 cells were maintained in complete DMEM and sub-cultured 1:10 every other day. J774.1 and RAW264.7 macrophages were maintained in complete DMEM and sub-cultured by scraping from plates with a cell scraper. Bone marrow derived dendritic cells (BMDCs) were prepared as described previously[185].

Cell preparation for imaging, fixation and staining

To prepare OT-I T cells for imaging, live cells were harvested using Ficoll-paque, washed with complete RPMI, and then held at 37 °C. To label TCRs for live cell imaging, 2×10^6 cells were stained with 1 µg of H57-597 non-blocking monoclonal antibody conjugated to either Alexa Fluor 488 or Alexa Fluor 568 on ice for 30 minutes, then rinsed once with complete RPMI. Live cells were imaged in RPMI supplemented with 2% fetal bovine serum, 100 U/mL penicillin, 0.1 mg/mL streptomycin, 2 mM L-glutamine, 10 mM HEPES and 50 µM β-mercaptoethanol (imaging media). For time lapse image sequences, 2×10^5 cells were added to the bilayer well. Once cells began interacting with the bilayer, imaging was initiated.

For SAIM imaging, 5×10^5 cells were added to each well, allowed to bind for 3 minutes, and then fixed with 20 mM HEPES, 0.2 M Sucrose, 4% paraformaldehyde (PFA), and 0.01% Glutaraldehyde for 10 minutes. The fixed cells were washed with 8 mL of PBS and then washed six times for five minutes with 1 mg/mL NaBH$_3$. Chambers were then washed with PBS, and blocked with 2% Donkey or Goat serum. Cells were stained for two hours with 2 µg/mL anti-LFA-1 (M17.4) and then washed with PBS. Cells were then stained for 1 hour with 2µg/mL

Donkey or Goat anti-Rat conjugated to Alexa Fluor 488 and 2 µg/mL H57-597 conjugated to Alexa Fluor 568. Cells were then rinsed with PBS for imaging.

To prepare for LLS live cell imaging, BMDCs were washed with IMDM supplemented with 10% fetal bovine serum, 100 U/mL penicillin, 0.1 mg/mL streptomycin, 2 mM L-glutamine, and 50 µM β-mercaptoethanol (complete IMDM), and then incubated in complete IMDM with 100 ng/mL of SIINFEKL peptide for 30 minutes at 37 °C and rinsed 3 times in complete IMDM. For experiments with labeled BMDCs, 4×10^6 cells were incubated in 500 µl of serum-free IMDM with 4 µl/ml DiD, which are lipophilic tracers for labeling the cell membrane, for 15 min at room temperature and rinsed 3 times in complete IMDM before use. OT-I T cells were harvested using Ficoll-paque, washed with complete RPMI and then held at 37 °C. 2×10^6 OT-I T cells were stained with 2.5 µg of CD45 non-blocking monoclonal antibody conjugated to either Alexa Fluor 488 or Alexa Fluor 647 on ice for 30 minutes, then rinsed once with complete RPMI. For LLS imaging of non-treated T cells, cells were imaged in complete RPMI (no phenol red) supplemented with 10 mM HEPES. For LLS imaging of PP2-treated OT-I T cells, cells were incubated with either 10 or 100 µM PP2 for 1 hour at 37 °C. Cells remained in 10 or 100 µM PP2 throughout imaging.

For LLS fixed cell imaging on activating lipid bilayers, 2×10^6 OT-I T cells were stained with 2.5 µg of CD45 non-blocking monoclonal antibody conjugated to Alexa Fluor 647 on ice for 30 minutes and then rinsed once with complete RPMI. 5×10^5 cells were added to a 5 mm in diameter round coverslip sitting in an imaging well of 8-well Nunc Lab-Tek II chamered coverglass, allowed to bind for 6 minutes, and then fixed with 20 mM HEPES, 0.2 M Sucrose, 4% paraformaldehyde (PFA) and 0.01% Glutaraldehyde for 10 minutes. The fixed cells were washed with 8 mL of PBS for imaging.

Supported lipid bilayers

Preparation and use of supported lipid bilayers was performed as previously described[50]. Briefly, phospholipid mixtures consisting of 96.5% POPC, 2% DGS-NTA (Ni), 1% Biotinyl-Cap-PE and 0.5% PEG5,000-PE in Chloroform were mixed in a round bottom flask and dried, first under a stream of dry nitrogen, then overnight under vacuum. All phospholipids were products of Avanti Polar Lipids. Crude liposomes were prepared by rehydrating the phospholipid cake at a concentration of 4 mM total phospholipids in PBS for one hour. Small, unilamellar liposomes were then prepared by extrusion through 100 nm Track Etch filter papers (Whatman) using an Avestin LiposoFast Extruder (Avestin).

8-well Nunc Lab-Tek II chambered coverglass were cleaned with 1 M HCl/70% Ethanol for 30 mins, followed by a rinse with water, then cleaned with 10 M NaOH for 15 mins. After cleaning, the chambers were washed repeatedly with 18 MΩ water and then dried. Lipid bilayers were set up on the chambered coverglass by adding 0.25 mL of a 0.4 mM liposome solution to the wells. After 30 minutes, wells were rinsed with 8 mL of PBS by repeated addition of 0.5 mL of PBS, then aspiration of 0.5 mL of the overlay. Non-specific binding sites were then blocked with 1% BSA in PBS for 30 minutes. After blocking, 25 ng of unlabeled streptavidin was added to each well and allowed to bind to bilayers for 30 minutes. After rinsing, protein mixes containing 63 ng ICAM-1 and 6 ng pMHC in 2% BSA were injected into each well. ICAM-1 preparation was described previously[50] while pMHC was provided by the NIH Tetramer Facility. After binding for 30 minutes, wells were rinsed again and 25 ng of QDot-streptavidin, TRITC-streptavidin, or unconjugated streptavidin was added to each well. Bilayers were finally rinsed with imaging media before being heated to 37 °C for experiments.

For LLS fixed cell imaging on activating lipid bilayers, 5 mm in diameter round coverslips were cleaned with 1 M HCl/70% Ethanol for 30 mins, followed by a rinse with water, then cleaned with 10 M NaOH for 15 mins. After cleaning, the coverslips were washed repeatedly with 18 MΩ water, and then dried. The coverslips were dropped into cleaned 8-well Nunc Lab-Tek II

chambered coverglass, and lipid bilayers were set up on the 8-well chambered coverglass as described above except that Qdots were not added to the lipid bilayer.

Analysis of Actin

For Latrunculin B challenge imaging by SCM, 2×10^5 cells were added to wells, and imaging was initiated for each cell as it began interacting with the bilayer. The cell was allowed to commence IS formation for about 45 seconds before injection of Latrunculin B to a final concentration of 1 µM. Injectant was a 0.5 mM solution of Latrunculin B in imaging media. Injectant was prepared from a 10 mM DMSO stock held at -20 °C until use. For LLS imaging of Latrunculin B-treated OT-I T cells, LatB was added to the imaging well to a final concentration of 1 µM.

To stain for F-actin, cells were added to bilayers and allowed to bind for 3-6 minutes, then fixed by addition of PFA to a final concentration of 4%. Cells were fixed for 10 min at room temperature, washed with PBS, then permeabilized for 2 min with 1% Triton X-100. Cells were again washed, and nonspecific binding blocked by incubating for 30 minutes with 1% BSA. Cells were then stained for F-actin with 1 Unit of Alexa Fluor 488-Phalloidin (Invitrogen) for 30 minutes at room temperature. Cells were finally washed in PBS before imaging.

Lattice Light Sheet Microscopy

Lattice light-sheet (LLS) imaging was performed in a manner previously described[77]. Briefly, 5 mm in diameter round coverslips were cleaned by a plasma cleaner, and coated with 2 µg/ml fibronectin in PBS at 37°C for 1 hour before use. BMDCs were dropped onto the coverslip and incubated at 37 °C, 5 % CO_2 for 20-30 min. Right before imaging, OTI T cells were dropped onto the coverslip which had BMDCs. The sample was then loaded into the previously conditioned sample bath and secured. Imaging was performed with a 488 nm, 560 nm, or 642 nm laser (MPBC, Canada) dependent upon sample labeling in single or two-color mode.

Exposure time was 10 ms per frame leading to a temporal resolution of 2.25 s and 4.5 s in single and two-color mode respectively.

Synaptic Contact Mapping (SCM) and Interference Reflection Microscopy (IRM)

The TIRF microscope is based on a Zeiss Axiovert 200M with a manual Laser TIRF I slider[50]. To image nanocontacts and TCRs, image sequences consisting of TCRs (TIRF), QD-streptavidin (widefield), and interference reflection microscopy (IRM, widefield) images were collected. For TIRF images, a 488 nm Obis laser (Coherent) was used for excitation of Alexa Fluor 488-labeled TCRs (or CD3ζ-GFP or ZAP70-GFP), and a 561 nm Calypso laser (Cobolt) was used for Alexa Fluor 568-labeled TCRs.

SCM used a combination of TIRF detection of TCR or GFP fusions together with wide-field excitation/emission of Quantum dots. Widefield QD images were acquired using a 405/10x excitation filter (Chroma Technology) in a DG-4 Xenon light source (Sutter). TCR and QD fluorescence were split using a DV2 with a 565 nm long-pass dichroic and 520/35m and 605/70m emission filters (Photometrics). Split images were collected using an Evolve an electron-multiplying charged-coupled device (emCCD) in quantitative mode (Photometrics). IRM images were acquired using a 635/20x excitation filter (Chroma Technology), and reflected light was collected onto the long-pass side of the DV2 imaging path. For time lapse image series, image sequences were typically acquired at 1 second intervals.

Scanning angle interference microscopy (SAIM) imaging

N-type [100]-orientation silicon wafers with 1933 nm silicon oxide (Addison Engineering) were cut into ~0.5 cm^2 chips using a diamond pen. Chips were cleaned with warm 20% 7✕ detergent, then washed with copious amounts of 18 MΩ water. After cleaning, chips were placed into wells

of an 8-well Nunc Lab-Tek II chambered coverglass. Bilayers were prepared on the chips using the same procedures as for coverslip supported bilayers. To measure bilayer heights, liposomes for supported lipid bilayers were labelled with 200:1 Vybrant DiO lipophilic dye (Molecular Probes) in PBS for 5 minutes, and then applied to the chips. Imaging was performed on an inverted Ti-E Perfect Focus System (Nikon) controlled by Metamorph software, equipped with 488 nm and 561 nm lasers, a motorized laser Ti-TIRF-E unit, a 1.49 NA 100× TIRF objective, emCCDcamera (QuantEM 512; Photometrics), and with a linear glass polarizing filter (Edmunds Optics) in the excitation laser path. Preparation of SAIM calibration wafers, and SAIM imaging and analysis were performed as described previously[186]. All images were filtered with a 1 pixel σ Gaussian filter to smooth background noise. For quantitative image analysis, local background subtraction followed by intensity thresholding was used to create whole cell and microcluster masks.

ZAP-70AS Mutations

For 3-MB-PP1 challenge imaging, 2×10^5 cells were incubated with 10 µM 3-MB-PP1 for 5 minutes at room temperature before introduction to bilayers. Bilayer wells were equilibrated with 10 µM 3-MB-PP1 before imaging. Cells were added to wells, and imaging initiated for a cell as it began interacting with the bilayer.

General Image analysis

All computational image analysis for SCM imaging was performed in Matlab (The Mathworks) and Fiji. Figure images were created by pseudocoloring images as needed in Fiji or in Matlab, then resizing to 600 dpi using bicubic interpolation in Matlab, Fiji or Photoshop (Adobe). Statistical analysis was performed using Prism (Graphpad). Analysis for LLS was performed in Imaris (Bitplane) and Matlab. The unique analysis code has been made available through

GitHub and can be found at the following URL: https://github.com/BIDCatUCSF/science-visualizingmicrovillarsearch.

Lattice Light Sheet: Post Processing

Raw data were deconvolved utilizing the iterative Richardson-Lucy deconvolution process with a known point spread function that was recorded for each color prior to the experiment[77]. The code for this process was provided by the Betzig lab at Janelia Farms. It was originally written in Matlab (The Mathworks) and ported into CUDA (Nvidia) for parallel processing on the graphics processing unit (GPU, Nvidia GeForce GTX Titan X). A typical sample area underwent 15-20 iterations of deconvolution.

Regions of interest (ROI) within the sampling area were cropped down to size and compressed from 32-bit TIFFs to 16-bit TIFFs using in-house Matlab code to allow immigration into Imaris. Within Imaris, the ROI was reoriented in 3D and the plane of interest (POI), such as the immunological synapse, was selectively cropped. The POI was then exported as TIFF files, which were recombined to produce maximum intensity projections (MIPs) at each time point using in-house Matlab code.

Plane of Interest Stabilization

To separate the lateral motion of the T cell from the motion of the surface protrusions, the POI was stabilized to the field of view (FOV) using one of two intensity unweighted center-of-mass calculations performed using in-house Matlab code. In the first method, a binary mask was created of the POI, which was then rounded to offset the effect of small surface protrusions before calculating the average x and y positions. The second method followed the same procedure but included eroding the mask to compensate for larger surface protrusions before calculating the average x and y positions. The evaluation of the method was performed

manually before a new image stack was created using the average x and y positions as the center of the FOV.

Mask Creation

To isolate ROIs for further analysis a non-regularly shaped mask was created to maximize information collection. Within Matlab each frame of the previously stabilized movie was converted to binary using a threshold above background. The image was then thickened to round out surface protrusions extending from the surface in the visualization plane, the holes were filled, and the gaps were closed. The mask was then shrunk by 3-5 pixels to exclude the intensity collected from the cell surface oriented orthogonal to the visualization plane. The final mask consisted only of pixels where the mask was colocalized throughout the entire observation period.

Surface Dynamics

Calculation of the dynamics of the surface protrusions was performed using in-house Matlab code. The membrane was thresholded by (membrane mean (within the mask area) + 3x standard deviation of the background) at each time point. The resulting binary image was used to determine instantaneous and cumulative surface coverage. To track microvillar protrusion, the "spots" function was used in Imaris, using a target spot size of 0.535 μm, followed by manual validation of spots and automated tracking using a "Brownian" model with a minimum duration above 13.5 seconds and maximum movement of 0.4 μm per timepoint.

Fractal Analysis

The fractal determination and fractal dimensions were calculated using an in-house Matlab script following the "box counting" method as previously described, which was validated using the ImageJ plugin FracLac (https://imagej.nih.gov/ij/plugins/fraclac/FLHelp/Introduction.htm). Briefly, a grid with an individual box length L was placed on top of the image. The image was shifted methodically in x and y dimensions to minimize the number of boxes needed to cover the entire active area of the cell. This process was repeated for a range of box lengths. The data are then fit to the equation $N = Ce^{-Fd}$ where N equals the number of boxes needed to cover the image, F_d is the fractal dimension and C is a constant, and e is the size of the box.

TIRF Contact / TCR co-localization

The contact TCR co-location was performed using an in-house Matlab script. Briefly, the contact "footprints" were used as a mask to isolate fluorescence intensity associated with TCRs. The intensity in each TCR "object" was then averaged and plotted in a histogram. A Gaussian distribution curve centered at the background fluorescence median was then overlayed. The contacts that fell within 3 sigma of the Gaussian distribution were then considered TCR$^-$, while the higher intensity contacts were considered TCR$^+$ and the binary representations were split into two separate image stacks.

Track Kymographs

To create kymographs from TCR microcluster tracks, microcluster centroids at each point in the track were converted to pixel indices. The track pixel indices were then used to create horizontal image lines of the TCR and QD605-SA intensity. Image lines at each time point were stacked to

create track kymographs in which the horizontal locations represent points along the track and the vertical positions represents time points.

SCM based contact segmentation and analysis

To identify and segment contact regions, the IRM images were first filtered with a high-frequency emphasis filter, then segmented using an active contour to identify the synapse footprint region on the bilayer. Intensity local minima inside the synapse region with intensities less than the median intensity in the synapse region were detected. Each local minimum was dilated with 3-pixel diameter disk structuring element (a cross) and used as a mask input for active contour segmentation of the Qdot image. If the active contour failed to detect a region in the Qdot image, the contour collapsed and the minima was discarded. After independent segmentation of all regions, regions that shared >50% of their area were merged to produce a final segmentation. Pixel indices for identified contact regions that remained after active contour analysis were saved. The centroid and equivalent radius of the contacts were used to create Spots objects in Imaris (Bitplane) for tracking analysis.

Contacts, TCR microclusters and ZAP70-GFP microclusters were tracked using the Imaris autoregressive motion-tracking algorithm with a 0.25 µm frame-to-frame distance criterion and 1 frame gap allowance.

Qdot Surface Projections

To generate Qdot image surface projections, images were first intensity normalized, then filtered with a 0.1 µm σ Gaussian filter, and then converted to surfaces. Surfaces were pseudocolored using the "hot" colormap in Matlab. To overlay TCR intensities on the surfaces, a duplicate of

the intensity surface was generated, pseudocolored green, and its alpha (opacity) values mapped to the normalized TCR intensity multiplied by 2.

TCR Dwell Time

Within Matlab, using a "rolling sum", frames of the binary TCR$^+$ and TCR$^-$ contacts were summed within an 18.9 second (30 frame) interval.

Statistics

Statistical tests as indicated by figure legends were performed using Prism 6 (GraphPad).

Chapter 3 – Visualizing and manipulating hyperstabilization of T cell microvilli contacts by engineered chimeric antigen receptors

Abstract

T cells typically recognize their ligands using a defined cell biology—the scanning of their membrane microvilli to palpate their environment—while that same membrane scaffolds T cell receptors (TCRs) that can signal upon ligand binding. Chimeric antigen receptors (CARs) present both a therapeutic promise as well as a tractable means to study the interplay between receptor affinity, microvillar dynamics and T cell function. CARs are often built using single-chain variable fragments (scFvs) with far greater affinity than that of natural TCRs. We used high resolution lattice lightsheet (LLS) and total internal reflection fluorescence (TIRF) imaging to visualize microvillar scanning in the context of variations in CAR design. This demonstrated that conventional CARs hyper-stabilized microvillar contacts relative to TCRs. Reducing the affinity and/or avidity of binding brought synapse microvillar dynamics into natural ranges, normalized synapse resolution and improved downstream effector function. This work highlights the importance of understanding the underlying cell biology when designing receptors for optimal antigen engagement.

Introduction

While epithelial cell microvilli are historically well characterized for their cell biology[71,187], advancements in microscopy have shown dynamic microvilli on T cells[68] to be critical for the cell's antigen search process[188–190]. During the antigen scanning phase of early immunological synapse formation, microvilli enable close contact with antigen-presenting surfaces and become stabilized specifically upon recognition of cognate antigen[188]. Furthermore, microvilli have been shown to contribute to T cell signaling by promoting optimal kinetic segregation of phosphatases away from signaling domains[191], and inducing the formation and confinement of microvilli has even been shown to be sufficient for T cell activation in the absence of TCR agonists[192].

T cell recognition occurs at immune synapses (IS), which are well studied in two dimensions on supported lipid bilayers (SLBs). TCR signaling at the prototypical immune synapse involves the local accumulation of signaling components colocalizing with microclusters of TCRs. After a few minutes, these can internalize[61,65] and/or migrate toward the center of the synapse into canonical central supramolecular activation clusters (cSMAC)[1,51,55]. The cSMAC – where active kinases are rare – is a site where TCR signaling is thought to end[51,53]. Microclusters are thought to be conducive to signal initiation and amplification – allowing two-dimensional segregation of phosphatases away from signaling domains. More recent work has revealed that TCR microclusters form on the tips of dynamically probing microvilli, facilitating their stabilization, and it is upon these microvillar protrusions that microclusters move laterally within the early synaptic interface[188].

Chimeric antigen receptor-bearing T cells (CAR T cells) present both a therapeutic promise, given their success in the treatment of B cell malignancies[109–112], and a tractable system for understanding how affinity and avidity affect topological synapse antigen scanning, given that they are easily engineered molecules. Typical CAR designs used for therapy incorporate a

tumor antigen-binding scFv, along with a hinge/transmembrane domain (commonly from either CD8 or CD28) and intracellular CD3ζ and co-stimulatory domains (commonly from either 4-1BB or CD28). Signaling events initiated by scFv binding and subsequent phosphorylation of intracellular components at the immune synapse lead to the acquisition of CAR T cell effector functions. Prior to this work, a recent study demonstrated aberrant synapse architecture formed by T cells downstream of CAR binding[143], although factors leading to that synaptic phenotype were not obvious. Whether and how CARs engage the underlying native cell biology remain largely unknown.

The antigen binding domains of engineered CARs and the T cell's natural antigen receptor differ significantly. CAR scFvs bind tumor antigen with nano- and even picomolar affinities whereas TCRs bind agonist peptide-major histocompatibility complex (pMHC) with micromolar affinity[147], although functional binding strength is improved by contributions of co-receptor[193]. The effect of such variation in binding on the dynamics of topological antigen scanning is unknown. This is an especially interesting question given that CARs generate inefficient intracellular signaling relative to TCRs[144,148,194]. It therefore seems plausible that improving the already ultra-high affinity binding might be beneficial. On the other hand, it is well accepted that T cells achieve high sensitivity through serial engagement[155,195] and thus the T cell's biology may be tuned to respond to a specific range of receptor binding dynamics[150–153,158]. Recent work shows that even within natural TCR affinity ranges, there is a "sweet spot" for binding strength[196]. We thus sought to understand how CARs interact with the natural cell biology, relative to TCRs, and how varying the binding dynamics of an antigen receptor affects topological antigen scanning.

To address these questions, we combined high-resolution lattice lightsheet (LLS) and synaptic contact mapping (SCM) total internal reflection fluorescence (TIRF) imaging – first, to establish the distribution of CAR relative to TCR on the T cell surface both prior to and during antigen

detection, and second, to establish the effects of receptor affinity and avidity on the dynamics of topological scanning. In order to study how topological scanning dynamics are affected by receptor affinity and avidity in isolation, point mutations were incorporated into the extracellular domains of the engineered receptor while all other aspects of CAR design were held constant – hinge and transmembrane domain (CD8), co-stimulatory domain (4-1BB), and CD3ζ signaling domain. In doing so, we found that CARs distributed similarly to TCRs. However, CARs based on conventional nanomolar high affinity dimer yielded hyperstabilization of the underlying microvillus relative to that of the natural TCR, which could be improved by reducing receptor affinity or avidity. Hyperstabilization was correlated with aberrant synapse resolution, decreased effector function, and increased propensity for exhaustion.

TCR and CAR distribution relative to microvilli on isolated T cells

TCRs have been reported to form patches[76,197,198] and localize to microvilli to varying degrees[75,76,188]. We expressed anti-HER2 CARs in primary human CD8+ T cells by lentiviral transduction and first sought to compare how they distribute on the T cell surface, compared to conventional TCR. To do this, we first fixed CAR T cells, stained them with antibodies that bound to TCR and CAR, and imaged them by LLS. Visually, this revealed that CARs were distributed across the surface of the cell with patches of increased fluorescence intensity, similar to that of TCR[76] although not necessarily overlapping in position (**Fig. 3.1A-C, Fig. 3.2A-B** and **Movie 3.1**). Although examined here on fixed cells, similar patches have also been described for TCRs by live imaging[76]. Zooming in to a region of the cell membrane, microvilli were thus noted as variably high for CAR alone, TCR alone, or both (**Fig. 3.1B** and **Fig. 3.2C**). About half of microvilli tips observed were high for TCR (either with or without CAR), and most but not all (83%) microvilli tips were CAR high (**Fig. 3.1C** and **Fig. 3.2D**), likely resulting from high CAR expression induced by lentiviral expression. Random distribution of CAR and TCR based off these proportions would predict ~40% co-occupied tips. By our count, 32% of tips are co-occupied, consistent with the co-occupancy being a random event.

Of note, not all CAR or TCR patches occurred on microvilli – TCR high, CAR high, and TCR/CAR high patch-like regions could be seen in both tips and areas of cell cortex, here referring to the regions on the body of the cell between microvilli (**Fig. 3.1D**). This was further demonstrated by overlaying the surface of the T cell based off CD45 expression with surfaces of high intensity TCR and CAR "patches" (**Fig. 3.1E**). To quantify this patchiness, the fluorescence intensity at the membrane was mapped to radial intensity profiles (**Fig. 3.1F** and **Fig. 3.2E**). Taking a moving average with a bin size of 10 pixels (~3° degrees), patches of increased local fluorescence were identified for TCRs, as expected[198], but less so for the

abundant CD45 molecule. Using this method, CARs were found to form patches at frequencies similar to TCRs (**Fig. 3.1G**) despite not obligately co-localizing.

In order to assess TCR and CAR patches relative to surface curvature in three dimensions, membrane surface curvature was mapped based off CD45 (**Fig. 3.3A** and **Fig. 3.4A**) and regions of high convexity were thresholded to show microvilli (**Fig. 3.3B**). CAR and TCR patches were assigned by identifying individual domains of locally high intensity along the cell boundary using Pearson correlation calculations for variable sized kernels followed by segmentation and watershed[76] (**Fig. 3.3C-D** and **Fig. 3.4A**). Surface areas of individual patches were then mapped by color (**Fig. 3.3E-F**). A histogram overlay and dot plots of hundreds of patches compiled from three cells show similar distribution of patch surface area for TCR and CAR, with median patch sizes of 0.34 μm^2 (TCR) and 0.38 μm^2 (CAR) (**Fig. 3.3G**). Surface curvature values on cells were mean-centered and both TCR and CAR patch localization were similarly mean-centered, indicating that there is not a preference for patches to reside in regions of high or low surface curvature values (**Fig. 3.3H**). Two-dimensional projections of the three-dimensional surface curvature and antigen receptor intensity were made and overlaid, revealing regions of membrane tips and valleys both with and without antigen receptor (**Fig. 3.3I**). Relative co-localization of TCR and CAR patches was assessed by counting the number of TCR and CAR patches that met varying thresholds of overlap with CAR and TCR patches, respectively. Total number of identified patches (0% colocalization threshold) was similar for CAR and TCR in a given cell, and the majority of patches for each receptor had <50% overlap with clusters of the other (**Fig. 3.4B-C**).

CAR enrichment at synaptic microvillar close contacts

Next, in order to determine the location of CARs following interaction with a target cell, live anti-HER2 CAR T cells were added to coverslips loaded with HER2+ SKBR3 cells and imaged by

LLS at intervals of 4.7 (**Fig. 3.5A-C, Fig. 3.6A** and **Movie 3.2**) or 6.75 (**Fig. 3.6B**) secs. This live

cell imaging revealed accumulation of CAR patches at projections into the synapse.

To further study the localization of CARs to these microvillar close contacts, mEmerald-tagged

CAR T cells were analyzed on HER2-loaded lipid bilayers using SCM TIRF microscopy. This

method allows for facile visualization of both the density of receptors near the surface by TIRF

in a green fluorescent channel, and the location of microvillar close contacts, as seen by holes

in fluorescent quantum dot (QD605) signal[188] (**Fig. 3.5D**). As previously demonstrated for

TCR[188], microclusters of CAR-mEmerald fluorescence were found to form and localize to areas

of microvillar close contacts, as seen by line scans revealing segregation between the two

signals (**Fig. 3.5E-F** and **Fig. 3.6D, F**). As with TCR, not all microvillar close contacts at the

synapse were occupied by CAR microclusters (**Fig. 3.6C**). To determine whether this

localization was dependent simply on the formation of a stabilized close-contact or depended

specifically on binding of CAR to its ligand, anti-HER2 CARs were expressed in OT-I mouse T

cells and allowed to interact with bilayers loaded with only the TCR ligand, pMHC:SL8

(SIINFEKL). In these HER2-negative synapses microvillar contacts were still formed but CARs

did not accumulate as microclusters nor localize within those contacts (**Fig. 3.5G-H** and **Fig.

3.6E, G**). Thus, we found that the recruitment of CAR microclusters to the microvillar close

contacts relied upon the binding of CAR antigen on the interacting surface, and that TCR

engagement was not sufficient to coordinate the CAR's reorganization at the interface.

Effects of affinity and avidity of receptor binding on synaptic microvillar

dynamics

We next sought to understand how microvillar close contacts, hallmarks of TCR-induced

activation[188,199], were modulated by the affinity of the antigen receptor. To do this, we compared

the wild-type high-affinity scFv (4D5) with a mutated scFv of ~70-fold reduced affinity (mut4D5,

Fig. 3.7A and **Table 3.1**). We then analyzed microvillar close contacts by SCM at high temporal

resolution in the presence of a range of ligand densities to measure microvillar persistence times (**Fig. 3.7B-D**). Ligand densities were standardized against two breast cancer cell lines that differed significantly in their HER2 levels, and addition of 62.5 ng per 0.7 cm^2 well yields expression levels comparable to a cell line representing healthy breast tissue, MCF7[200–202] (**Fig. 3.8A-B**). In the examples in **Fig. 3.7C** and **Movie 3.3,** individual microvillar close contacts mediated by low-HER2 bilayers remained stable in the case of a high-affinity CAR contact, while the low-affinity CAR close contact dispersed within seconds. The lifetime of individual microvillar close contacts was measured using automated scripts that identify regions of QD605-exclusion. This revealed that the persistence time of CAR-occupied close contacts increases with ligand density for low affinity CARs, but that high affinity CAR resulted in very stable contacts at all tested ligand densities (**Fig. 3.7D**). All conditions tested induced stabilization of microvilli above background non-receptor-occupied contacts, which had uniformly short persistence times. Notably, at high HER2 density, the persistence of low-affinity CAR close contacts reached ~17 secs on average, a value that was achieved by high-affinity CAR even at 100x lower antigen densities – lower even than the low-HER2 MCF7 standard. Importantly, both low (62.5 ng/well) and high (625 ng/well) antigen densities led to calcium flux for both receptors, as detected by Fura-2 ratiometric imaging (**Fig. 3.8C-D** and **Movie 3.4**). At high density of antigen, calcium imaging demonstrated a decrease in the magnitude of the maximal ratio achieved, specifically for the high-affinity CAR (**Fig. 3.8D**), suggesting altered signaling dynamics in the high-affinity setting.

We next sought to directly compare CAR- and TCR-mediated persistence times. We thus expressed the low-affinity CAR in OT-I mouse T cells and compared interactions with SL8:pMHC- and HER2-loaded bilayers. On bilayers with SL8:pMHC, normalized to levels displayed on APCs[203], we measured TCR-mediated persistence to be an average of 12.3 seconds. Low-affinity CAR with low-HER2 bilayers yielded similar persistence times whereas

persistence times on high HER2 were again found to be significantly greater (**Fig. 3.7E**). We hypothesized that we could further engineer the low-affinity CAR to yield TCR-like persistence times in high antigen-density conditions by minimizing CAR avidity contributions. Thus, we created a monomeric CAR by incorporating two cysteine to serine point mutations in the CD8α hinge to prevent formation of the disulfide bridge[100] (**Fig. 3.8E**). Comparing the persistence time of monomers to dimers on high HER2-loaded bilayers (625ng/well) revealed that only the low-affinity monomers produced microvillar persistence similar to that of the TCR (**Fig. 3.7F**). Average CAR fluorescence intensity of close contacts was not significantly different between monomers and dimers and did not appear to correlate with persistence times under the conditions tested (**Fig. 3.8F-G**).

Hyperstable microvillar dynamics are associated with altered synapse resolution, decreased effector function, and increased propensity for exhaustion

TCR-mediated synapses formed on antigen-loaded lipid bilayers result in TCR microcluster formation and radial motion of microclusters toward the center[51–53]. Although alternative synapse architectures characterized by the formation of CAR microclusters without centripetal movement or cSMAC formation have been revealed for CAR-mediated synapses[143], we sought to relate binding dynamics resulting in hyperstabilization of microvilli to synapse dynamics and centralization. Measurement of the distance across T cell microclusters following TIRF imaging of synapses – a means of assessing centralization – revealed that dimeric CAR microclusters only formed a central dense cluster under conditions of low affinity and low antigen density, whereas the monomers reliably formed this structure (**Fig. 3.9A-B**).

In order to determine whether this phenotype was the result of a lack of mobility of microclusters, as opposed to direct accumulation of CARs in the center vs. periphery, we tracked the microclusters over time (**Fig. 3.10** and **Movies 3.5-10**). On high-HER2 bilayers, the

low-affinity CAR monomer yielded mobile microclusters, whereas both CAR dimers showed impaired mobility as demonstrated by flower plots of microcluster displacement, and analysis of displacement and speed (**Fig. 3.9C-D** and **Fig. 3.11A-B**). The mobility of low-affinity but not high-affinity CAR dimer microclusters was restored on low HER2-loaded bilayers (**Fig. 3.9C-D** and **Fig. 3.11A-B**). Analysis of the direction of microcluster movement revealed no significant differences (**Fig. 3.11C**). Therefore, we found that a monomerized low-affinity CAR supported the formation of synapse architectures and dynamics characteristic of TCRs on antigen-loaded lipid bilayers, whereas high-affinity dimerized CARs did not.

Given these proximal effects on synapse dynamics, we sought to determine the downstream effects of the hyper-stable or more physiological receptors. In order to compare between HER2 levels for T cell stimulation experiments, we first used two breast cancer cell lines: the MCF7 luminal breast cancer cell line, which does not over-express HER2[200–202], and the SKBR3 cell line, which endogenously over-expresses HER2 and thus mirrors HER2-positive breast cancers[204] (**Fig. 3.9E** and **Fig. 3.8A, 3.12A**). In coupling assays to assess overall synapse formation[205], all combinations yielded robust coupling (**Fig. 3.12B-E**). Early activation, as measured by CD69 staining at 18 hours following stimulation, and entry into cell cycle, measured by Ki67 staining at 96 hours, were similarly robust for all CAR interactions with either low- or high-HER2 targets (**Fig. 3.12F-H**). While all conditions induced a proliferative burst as measured by VPD dilution after 96 hours, rounds of proliferation varied significantly, with the greatest proliferation observed using low-affinity dimeric CAR (**Fig. 3.9F-G**).

Assaying effector function by intracellular staining for IFN-γ at 18 hours post-stimulation also revealed increased production of this cytokine in cells bearing low-affinity CAR dimers relative to high-affinity ones (**Fig. 3.9H**). In these cocultures, less IFN-γ was produced by dimeric CAR T cells when incubated with high-HER2 SKBR3s than with low-HER2 MCF7s. In this regard, while

the low-affinity monomeric CAR displayed a decreased magnitude of response, likely in part due to a lack of constitutively paired intracellular CD3ζ, it improved the expected dose-dependent response pattern.

Finally, we incubated mouse CAR T cells with MC38 tumor cells expressing variable HER2 levels – using this strategy to also minimize the effect of varying the background gene effects of using two cell lines. Low and high affinity receptors performed similarly for cytokine production (**Fig. 3.13A-B**) but when we shifted these cultures to hypoxia, mimicking the tumor microenvironment and licensing deeper progression into exhaustion[206], the conventional high affinity dimer was more susceptible to exhaustion as measured by TOX and PD1 co-expression (**Fig. 3.9I**), in line with recent work[196] using native TCRs.

Discussion

Factors that control the dynamics of T cell microvilli are not well understood. This is in part because this dynamic microvillar biology is somewhat unique – the well-studied microvilli at the intestinal brush border are relatively much less dynamic[71,72]. Here, using LLS and synaptic contact mapping TIRF imaging, we show that CARs and TCRs distribute as patches that occupy regions of both microvilli and cell cortex on isolated T cells much like TCR, although not obligately overlapping in position. The distinctness of the synthetically engineered transmembrane domain – taken from CD8 – and intracellular domains appear to result in an initial propensity to segregate as patches independently of TCRs. We hypothesize that this results from differential miscibility and recruitment of membrane lipids related to combinations of transmembrane and cytoplasmic domains although studies of this represent a significant tangent from our work. Future studies will be needed to reveal the factors that lead to the formation of patches, or "condensates"[207], prior to TCR triggering and how to manipulate them. Following receptor binding, we show that CAR microclusters accumulate at the tips of microvilli, which are hyperstabilized in comparison to those mediated by TCRs. The finding that contact stability is directly related to receptor affinity and avidity is consistent with previous work showing that stabilization by TCR was maintained even following inhibition of TCR-proximal signaling or actin blockade[188]. Taken together, this suggests that microvillar stabilization is highly related to the strength of physical binding of extracellular receptors.

The actin cytoskeleton is a key regulator of T cell function, not just for successful migration[208], but also for optimal immune synapse formation and T cell activation[209]. In fact, even the T cell's synaptic partners can contribute to the cytoskeletal dance – dendritic cell (DC) actin dynamics promote efficient T cell activation, and notably favor a multifocal distribution of microclusters at the T:DC synapse[210]. A multifocal synapse also forms during thymic negative selection[66], where TCRs that bind too strongly to self-ligands induce cell death. Slower receptor unbinding kinetics

have also been associated with reduced actin velocity[211]. Given these findings, it is tempting to speculate that multifocal patterns may be a general indicator of relatively "strong" contacts[212], although as the above examples demonstrate, the implications of that phenotype vary by context. We see here on SLBs that it represents a super-physiological outcome of ultra-high affinity/avidity binding that does not correlate with optimal effector function. Many prior works also demonstrate that increasing the binding strength of antigen receptors does not reliably predict the efficiency of T cell activation and ultimate effector function, both for natural TCR[150–153,158,213] and engineered CAR[142,148,149,201].

Future studies to further characterize the regulators of T cell microvillar dynamics and better sub-classify actin-based synaptic protrusions, especially those present during early and late synapses, will reveal new mechanisms of control of T cell activation[214]. The experiments performed here reveal that receptor binding affinity and avidity control the dynamics of synaptic microvilli. Given that microvillar persistence in TCR-occupied contacts was not dependent on downstream signaling through ZAP70[188], these findings indicate that affinity and avidity of binding directly affect the movements of the opposing cell surfaces. Thus, discovering how engineered receptors interact with the cell biological processes underlying recognition contributes to our understanding of the mechanism both of the therapy and the system itself. This work opens up new avenues for future research to determine whether better quality T cells could be produced for cell therapies by boosting the intracellular signal downstream of physiologically normalized binding dynamics. The formation of receptor-ligand complexes at cell-cell interfaces is integral to intercellular communication. However, the 3-dimensional structure of cellular interfaces and how movements of the plasma membrane affect the formation of and signaling through such complexes is relatively understudied. Similar mechanisms are likely at play in other cell:cell interfaces.

Figures
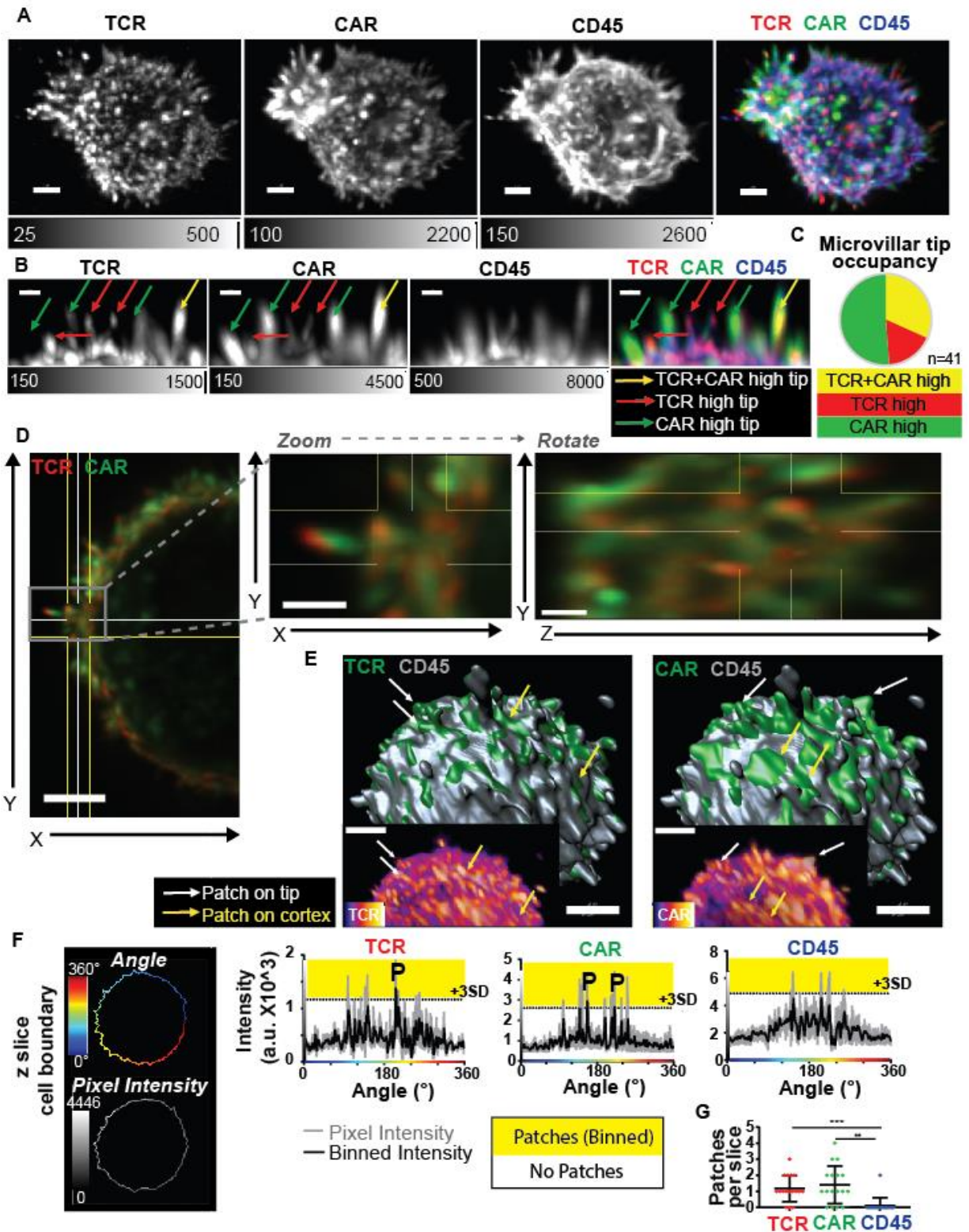
Figure 3.1. CARs distribute similarly to TCRs on both microvilli and cell cortex, but do not obligately co-localize.

(A) Fixed anti-HER2 CAR T cell showing maximum intensity projection of TCR, CAR, CD45 and overlay imaged by lattice light-sheet. Scale bar = 2 µm. Human CD8+ T cell expressing anti-HER2 CAR (mut4D5) was labelled with antibodies to MYC (CAR)-Alexa488, TCR (OKT3)-APC, and CD45-Alexa594. **(B)** Region of cell membrane, as described in A, where microvilli tips are marked as being high for TCR (red arrow), CAR (green arrow), or both (yellow arrow). Scale bar = 1 µm. **(C)** 41 tips across 5 regions and 3 cells were scored as in B. **(D)** Left panel shows zoomed out membrane region in extended view for multiple z slices of a cell labelled as described in A (scale bar = 3 µm). Middle panel shows zoom in on outlined region (scale bar = 1 µm). Right panel shows the same zoom region with the perspective rotated to show the YZ plane (scale bar = 1 µm). **(E)** Large panels show CD45 surface (gray) overlaid with TCR (left) and CAR (right) surfaces marking areas of high intensity (green). Arrows mark examples of patches on microvilli tips (white) or cell cortex (yellow). Inset panels show a region of the same cell with the raw TCR and CAR intensity in Fire colorscale. Scale bar = 4 µm. **(F)** Left: Schematic showing the cell boundary as mapped to radial intensity profile by angle (x-axis) and pixel intensity (y-axis). Right: Pixel intensity (gray line) and binned intensity (black line), defined by taking a moving average of 10 pixels, showing one z-slice for TCR, CAR, and CD45. Dashed line with yellow above indicates 3 standard deviations (+3SD) above mean pixel intensity. P indicates binned intensity peaks above +3SD threshold (patches). **(G)** Number of patches/z-slice for each receptor was defined by the number of excursions of binned intensity above the +3SD threshold. Tukey's multiple comparisons test was performed on data compiled from multiple slices of 3 cells (n = 17 slices per group). Error bar represents standard deviation (s.d.).
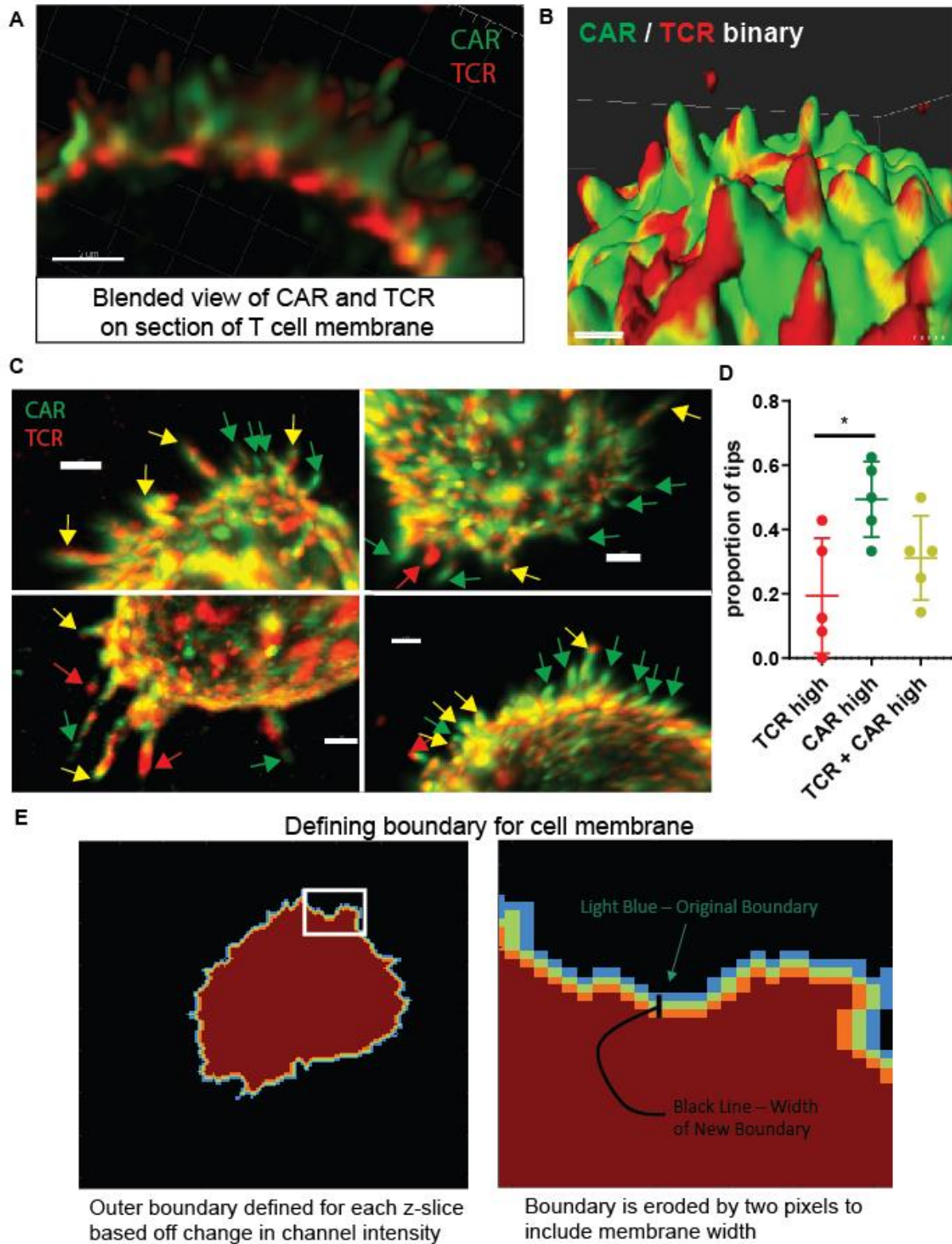
Figure 3.2. LLS imaging of TCR and CAR on the surface of isolated T cells.
(A-B) Blended view (A) and shaded binary (B) Imaris rendering of fixed anti-HER2 CAR T cell surface, as described in Fig. 3.1A. Blended rendering shows section of 40 z slices. Scale bars are 2 μm. **(C)** Regions of interest (in addition to Fig. 1B) that were used for the manual count of

microvillar tip receptor occupancy in Fig. 3.1C and (D). Microvilli tips are marked as being high for TCR (red arrow), CAR (green arrow), or both (yellow arrow). Scale bars = 2 µm. **(D)** Proportion of microvillar tips per region of interest that were marked as high for, CAR, or both. 41 tips across 5 regions and 3 cells were scored. **(E)** Schematic of method used to define the cell membrane boundary used in radial intensity profiles.
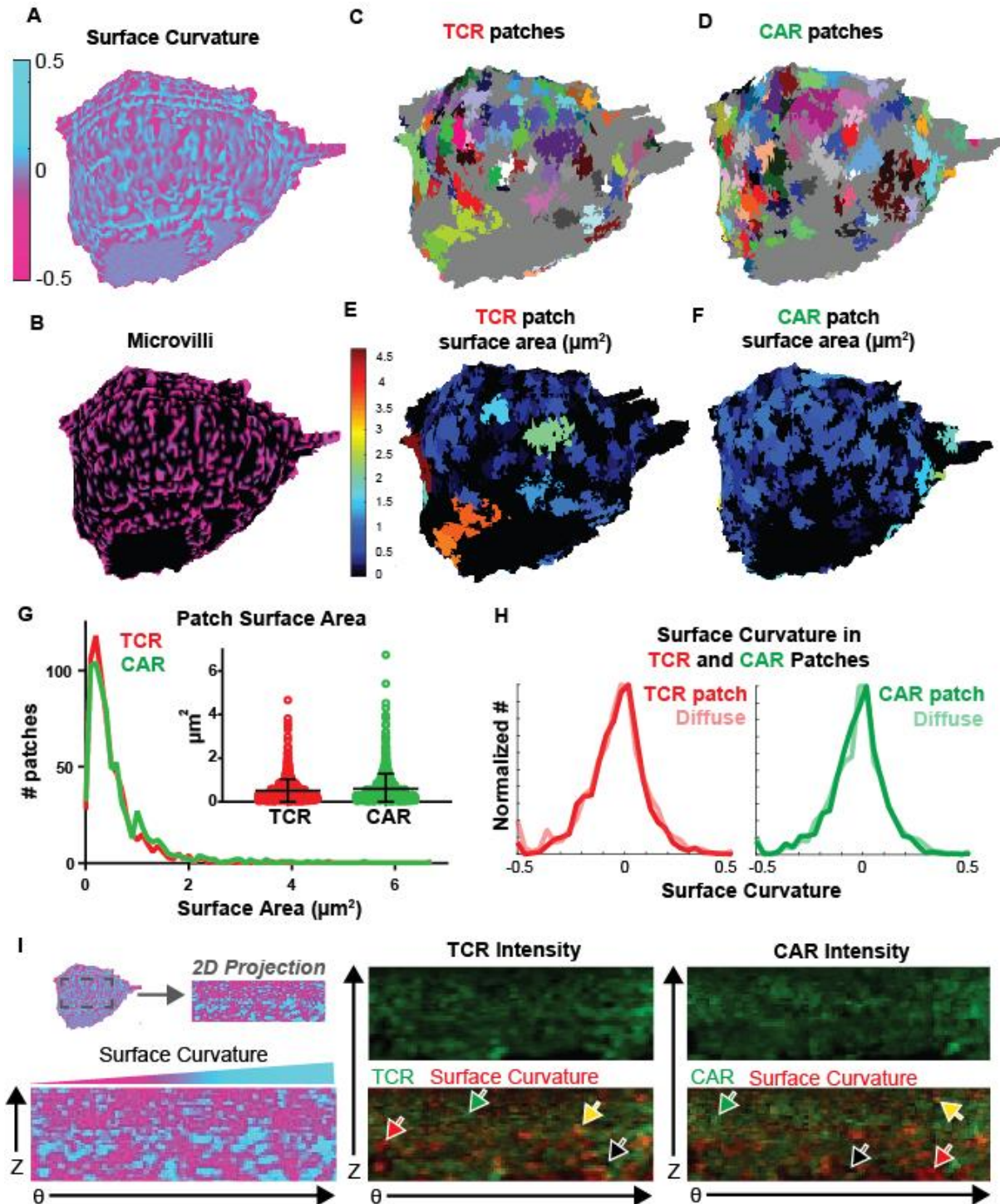
Figure 3.3. Quantification of TCR and CAR patches relative to surface curvature.
(A) Curvature of the cell surface was mapped based off the cell boundary defined by CD45, with valleys marked by cyan and tips marked by magenta. Fixed CAR T cell was labelled with antibodies to MYC (CAR)-Alexa488, TCR (OKT3)-APC, and CD45-Alexa594. **(B)** Microvilli are highlighted by masking the surface curvature in A based on convexity. **(C-F)** TCR (C,E) and CAR (D,F) clusters defined by regions of high local (3D) intensity are shown as different colors (C-D) and colored according to surface area of cluster (E-F). **(G)** Histogram and dot plot (inset)

of cluster surface area is shown for TCR and CAR. TCR and CAR median values are 0.34 and 0.38 µm^2, respectively. Data is compiled from three cells. Dot plot shows mean and s.d. **(H)** Histograms of surface curvature for TCR (left) and CAR (right) found in patches or outside of patches. **(I)** 2D projections from the surface show curvature increasing from convex (magenta on left, black in overlay) to concave (cyan on left, red in overlay); TCR intensity (middle); and CAR intensity. Yellow and red arrows mark membrane valleys with high and low receptor intensity, respectively. Green and black arrows mark membrane peaks with high and low receptor intensity, respectively.
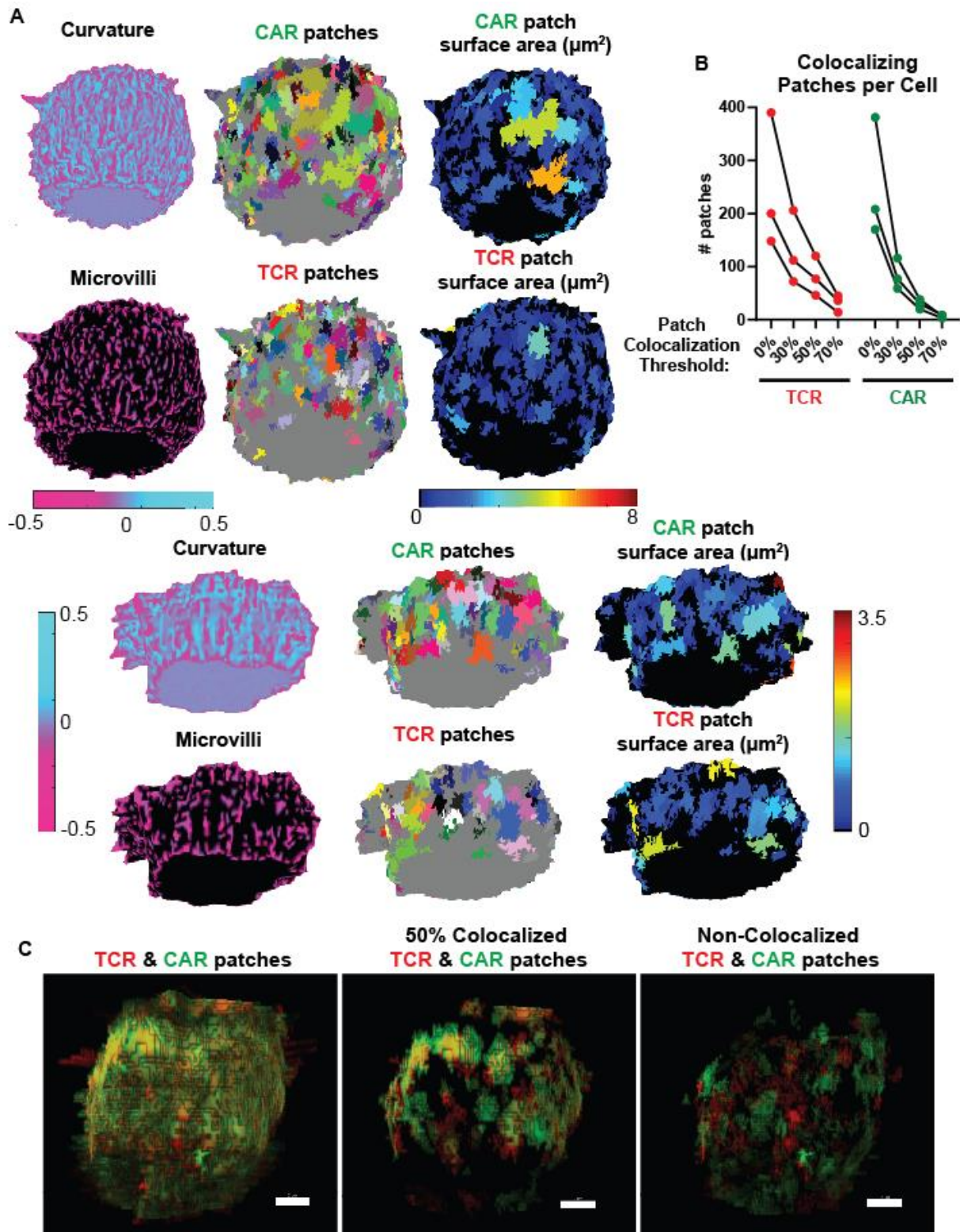
Figure 3.4. Quantifying the colocalization of TCR and CAR patches.
(A) Two additional examples of cells analyzed as described in Figure 3.3A-F. **(B)** Clusters are quantified for increasing thresholds of co-localization. Left: TCR clusters are quantified which have 0, 30, 50, or 70% overlap with CAR clusters. Right: CAR clusters are quantified which

have 0, 30, 50, or 70% overlap with TCR clusters. **(C)** Maximum intensity projection of TCR and CAR patches rendered in Imaris. For each patch, the intensity is defined by the integrated intensity for that patch. All patches are shown on the left. Patches which are ≥50% co-localized (i.e. 50% of the CAR patch overlaps with TCR, and vice versa) and <50% co-localized are shown in middle and left panels, respectively.
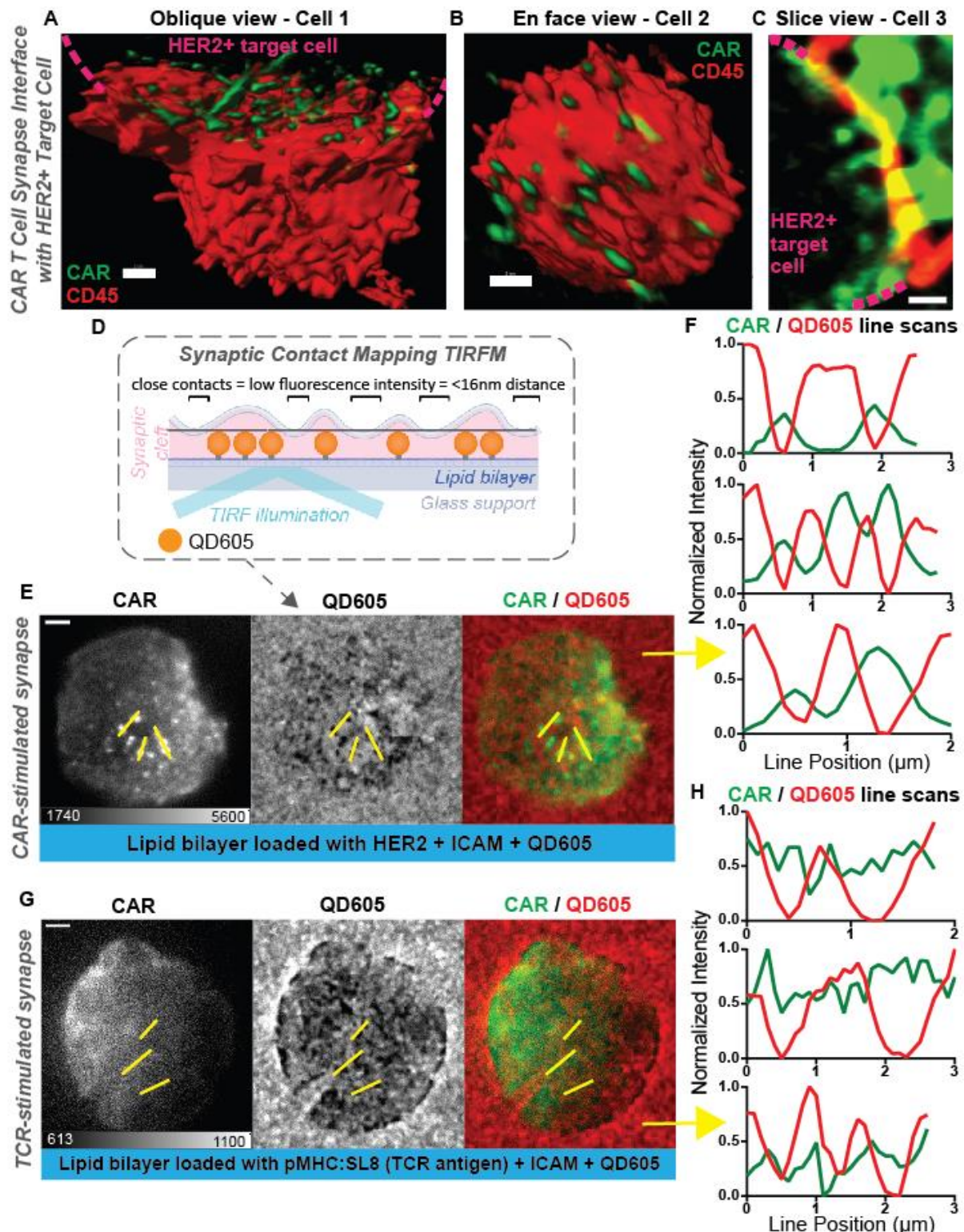
Figure 3.5. CAR is enriched at sites of microvilli close contacts in synapses with cognate antigen, but not following engagement of endogenous TCR.
(A-C) Three examples of anti-HER2 CAR T cells interacting with HER2+ SKBR3 are shown from an oblique view of the synapse interface (A, Imaris blended view, scale bar = 2 μm), en face synapse view (B, Imaris blended view, scale bar = 2 μm), and a single z-slice (C, scale bar

= 1 μm). The SKBR3 target cell location is marked by dashed magenta lines (A, C). Human CD8+ T cell expressing anti-HER2 CAR (4D5) was labelled with antibodies to MYC (CAR)-Alexa488 and CD45-Alexa647. **(D)** Schematic of synaptic contact mapping method. Lipid bilayer on glass support is loaded with Qdot 605, which is a red-fluorescent probe that occupies ~16nm in height. Areas where the cell makes a close contact (<16nm distance) appear as holes in the QD605 signal. **(E)** CAR T cell synapse imaged by TIRF showing CAR-mEmerald, microvillar projections (as seen by holes in QD605 signal), and overlay. Human CD8+ T cell expressing anti-HER2 CAR (mut4D5) interacting with lipid bilayer loaded with 625ng HER2 + ICAM + QD605. Scale bar = 2 μm. **(F)** Line scans from F show anti-correlation of CAR-mEmerald and QD605, indicating enrichment of CARs within microvillar contacts. **(G)** OT-I mouse T cells were retrovirally transduced with anti-HER2 CAR (mutCD45). Synapse shown was formed on lipid bilayer loaded with pMHC:SL8 + ICAM + QD605. TIRF imaging of CAR-mEmerald, QD605, and overlay are shown. Scale bar = 2 μm. **(H)** Line scans from H showing the lack of enrichment in CAR signal within QD605 holes, indicating that CAR microclusters do not accumulate in microvillar close contacts in absence of the CAR's cognate antigen.
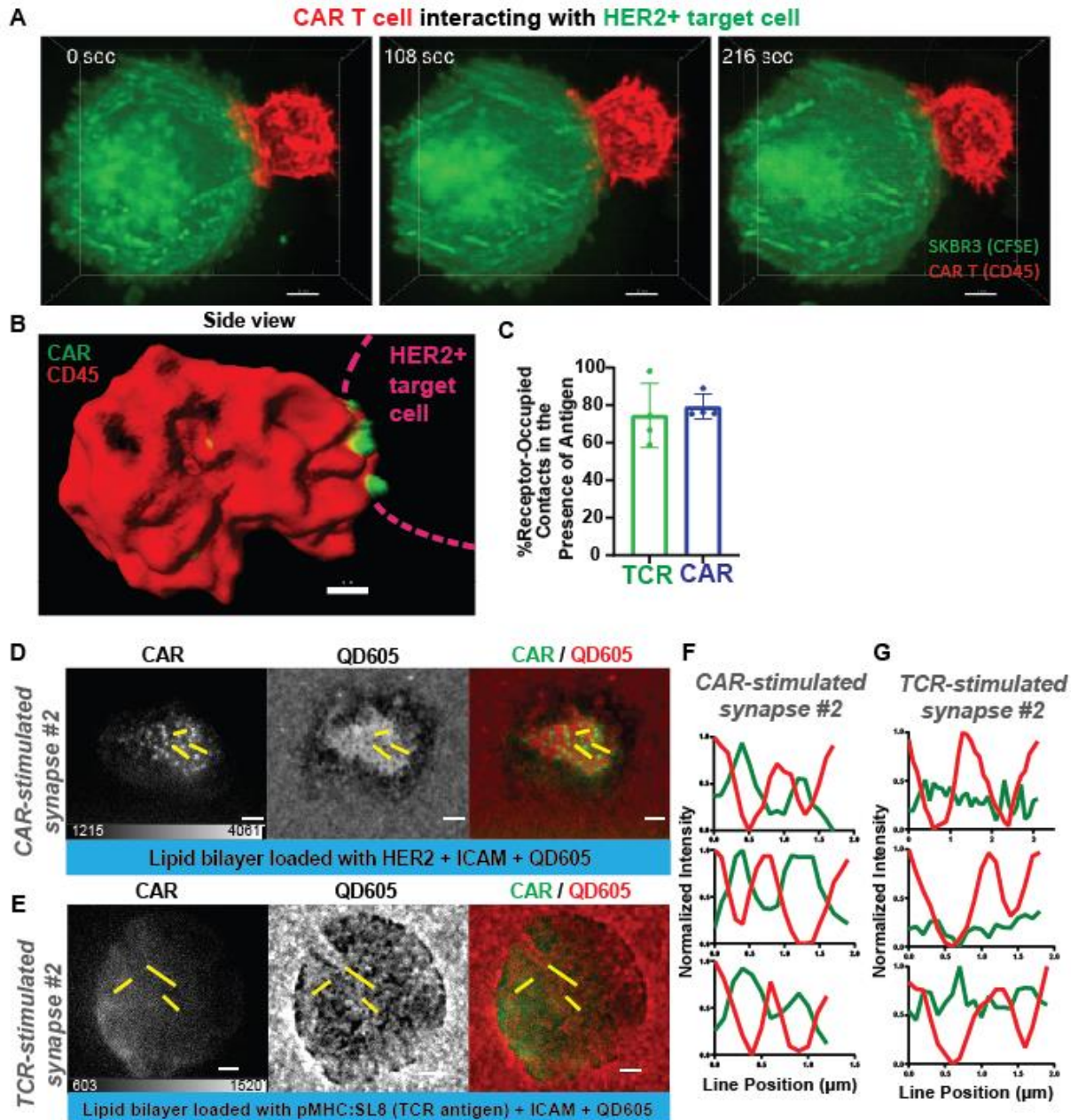
Figure 3.6. Imaging CAR T cell:target cell interactions.
(A) Time-lapse of anti-CD45-Alexa647-stained CAR T cell interacting with CFSE-labelled HER2+ SKBR3 tumor cell by LLS imaging shows stable cell:cell interaction. Maximum intensity projection from Imaris is shown. Scale bar = 3 μm. **(B)** Additional example of a side-view of CAR T cell synapse with HER2+ SKBR3 target prepared as in Fig. 3A-C but with intensity based off endogenous mEmerald tag alone, without additional anti-MYC labelling. CAR localization without anti-MYC labelling shows the same enrichment of CAR in synaptic projections. Maximum intensity projection from Imaris is shown. Scale bar = 2 μm. **(C)** The percentage of microvillar close contacts occupied by receptor was not significantly different between the OT-I TCR and the low-affinity CAR murine T cell synapses with cognate antigen (SL8:pMHC and 625 ng/well HER2). n = 4 cells. **(D-G)** Additional examples of cells prepared and analyzed by line scan as in Fig. 3F-I.
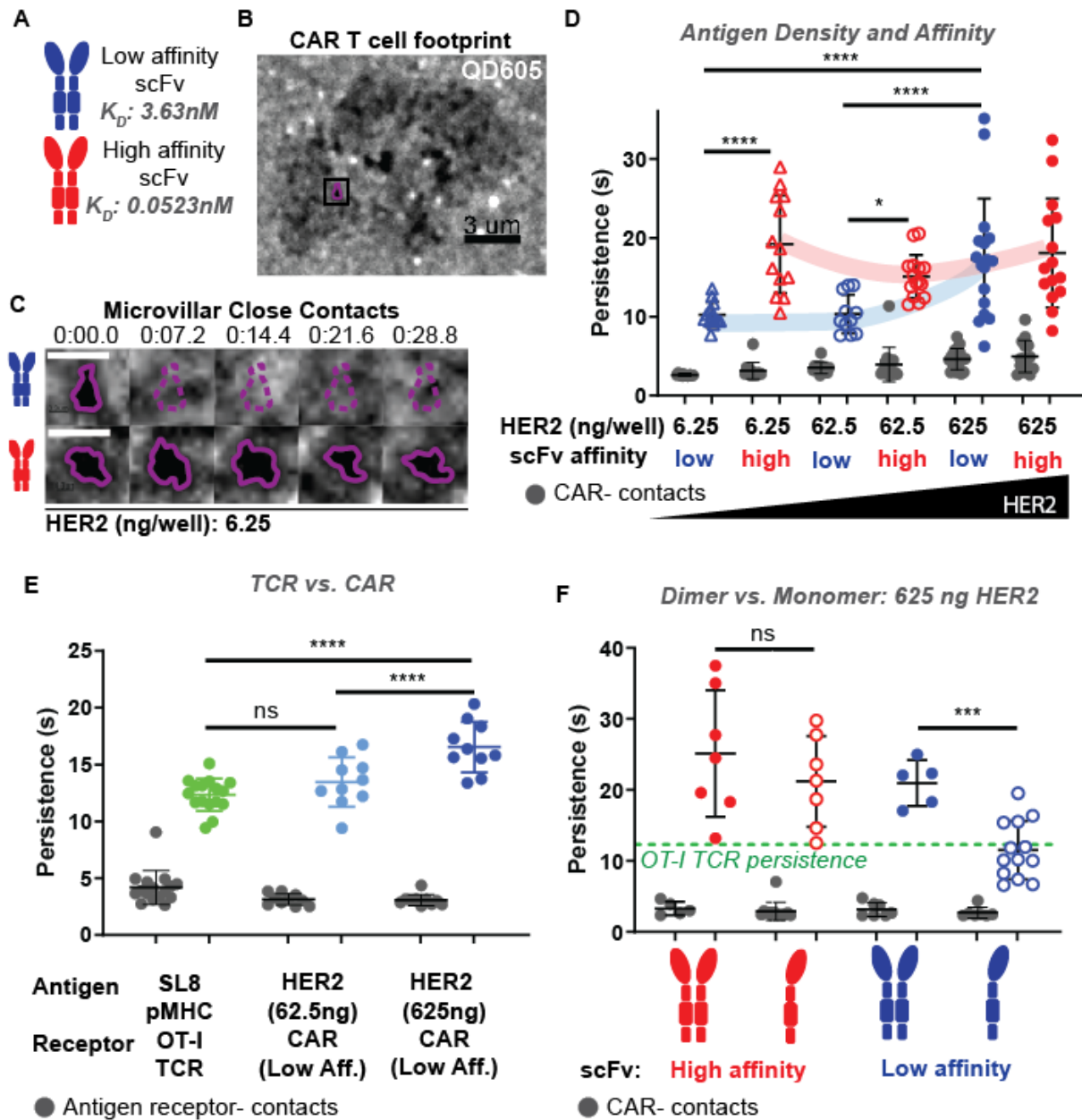
Figure 3.7. Conventional CAR interactions of high affinity or high antigen density result in hyper-stabilization of underlying microvillar protrusion, which can be reduced by using monomeric CAR.

(A) Experiments were performed comparing CARs with a high-affinity scFv against HER2-based off trastuzumab (4D5, KD = 0.0523nM, red) and a lower affinity scFv made by substitution of three amino acids (see Table 3.1, mut4D5, KD = 3.63nM, blue). **(B)** Bilayers were loaded with fluorescent quantum dots (QD605) with a height of 16nm. Locations where the cell makes close contact with the bilayer (<16nm) are visualized as holes in QD605 signal due to their size-based exclusion. QD605 signal is shown for a low-affinity CAR T cell interacting with a lipid bilayer loaded with 6.25 ng HER2. Outlined contact is shown in C. Scale bar = 3 μm. **(C)** QD605 signal across 5 time points are shown for the same field of view, each on low HER2 bilayers (6.25 ng/well). Top: Microvillus from low-affinity CAR T cell moves out of view. Bottom: Microvillus from high-affinity CAR T cell remains across time points. White scale bar = 1 μm. **(D)** CAR-

occupied close contact persistence times (blue, red) and CAR-negative close contact persistence times (gray) are shown for varying antigen densities and affinities. All CAR:HER2 interactions tested result in CAR-occupied microvillar contact stabilization above background CAR-negative contacts (gray). Persistence time is further increased in interactions of high-affinity CAR (red), even at lowest HER2 densities on the bilayer. For low-affinity CAR (blue), only high levels of HER2 yield similar persistence times to high-affinity CAR. Data is shown for at least 11 cells per condition across four experiments (n = 84, 13, 13, 11, 15, 17, 15 cells per group from left to right, respectively). **(E)** Low-affinity CAR was retrovirally expressed in primary mouse OT-I T cells. Receptor-occupied microvillar persistence times are shown for OT-I:SL8 (green), Low-affinity CAR:Low HER2 (light blue), and Low-affinity CAR:High HER2 (dark blue) interactions. All cognate interactions are stabilized above background receptor-negative contacts (gray). CAR:High HER2 persistence is hyper-stable relative to TCR:pMHC stabilization. Data is shown for at least 10 cells per condition across three experiments (n = 36, 16, 10, 10 cells per group from left to right, respectively). **(F)** Dimers (filled dots) and monomers (open dots) are compared on high HER2 bilayers (625ng/well). Only monomeric low-affinity CAR regains natural persistence time of TCR:pMHC contacts (green dashed line). All receptor-occupied contacts are stabilized above non-cognate antigen interactions (gray). Data is shown for at least 5 cells per condition across three experiments (n = 32, 7, 7, 5, 13 cells per group from left to right, respectively). All error bars represent s.d. and analyses shown are Šídák's multiple comparisons tests.
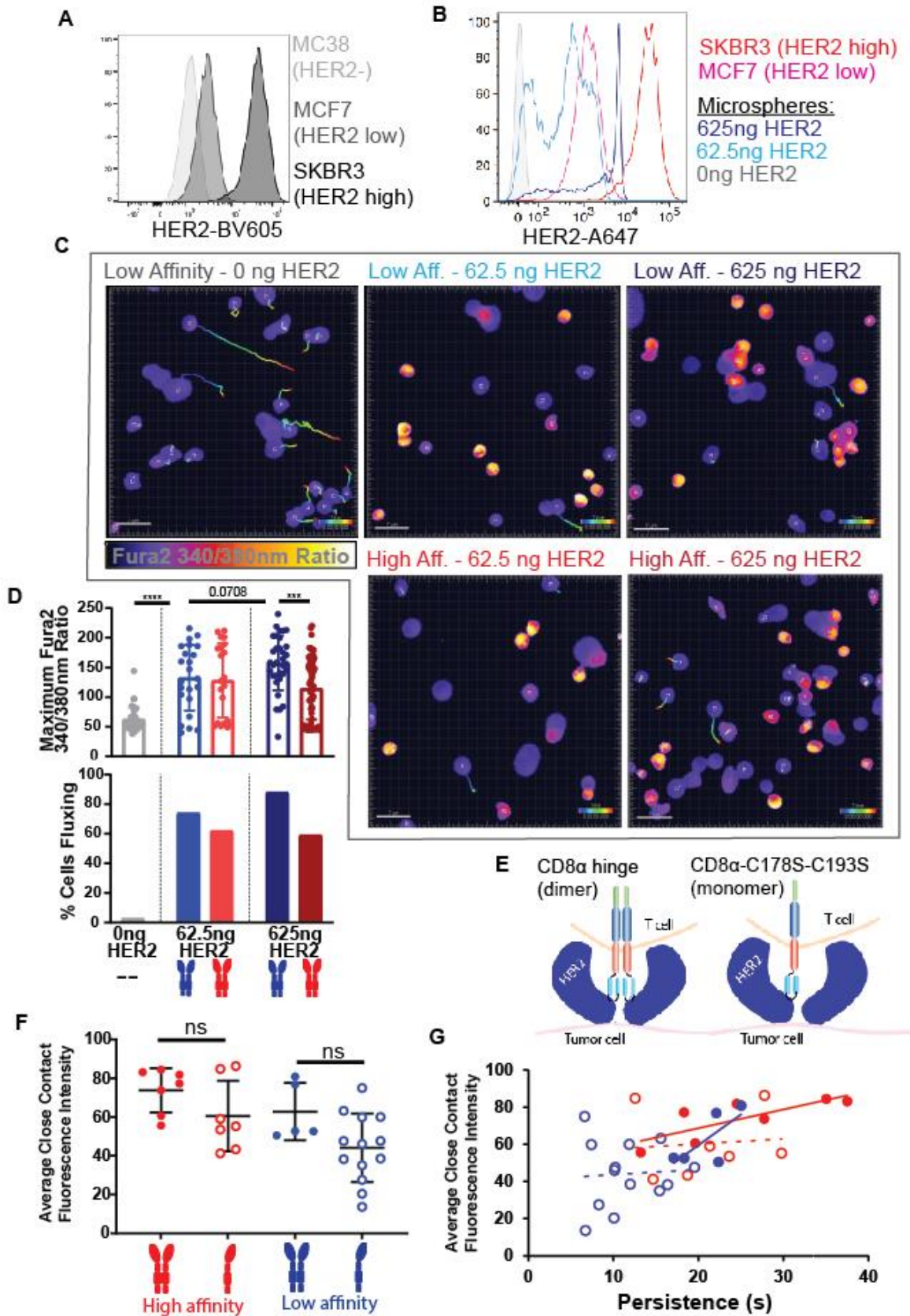
Figure 3.8. CAR T cell interactions across affinity and antigen densities.

(A) Anti-HER2-BV605 staining was performed on the human breast cancer cell lines MCF7 and SKBR3, plus murine MC38 cells as a HER2-negative control. Histogram overlay shows low and high HER2 expression for MCF7 and SKBR3, respectively. **(B)** Lipid bilayers with varying HER2 densities were built on 5 μm microspheres as standards for comparison to high-HER2 expressing SKBR3 and low-HER2 expressing MCF7s. Representative histogram from two independent experiments. **(C)** Fura-2 ratio images showing calcium flux (yellow) with tracks for interactions of CAR T cells with HER2-bilayers across antigen density and CAR affinity. Control well with no HER2 is shown on left. Images shown are at 3 min following addition of T cells. Scale bars are 7 μm. **(D)** Fura-2 ratio imaging shows calcium flux across affinity and HER2 density, with low-affinity CAR T cells outperforming high-affinity CAR T cells on high-HER2 loaded bilayers. Top: Maximum Fura-2 ratio for cells was quantified at 5.5 min following addition of T cells. Error bars represent s.d. (n = 37, 23, 21, 33, 66 cells per condition from left to right, respectively). Analyses are unpaired t tests. Bottom: Percentage of cells fluxing (defined as maximum Fura-2 ratio > 100) for each condition was quantified at 5.5 min following addition of T cells. **(E)** Schematic of original anti-HER2 CAR, including two cysteines in the CD8 hinge region that form disulfide bond, and monomeric CAR made by mutation of those cysteines to serine hinge[100]. **(F)** The average close contact CAR-mEmerald fluorescence intensity was not significantly different between monomers and dimers. Data is shown for at least 5 cells per condition across three experiments (n = 7, 7, 5, 13 cells per group from left to right, respectively). Error bars represent s.d., analyses shown are unpaired t tests. **(G)** Average close contact CAR-mEmerald fluorescence intensity was plotted against persistence time following color schema in F. Linear trend lines were added for each CAR type (monomers dashed).
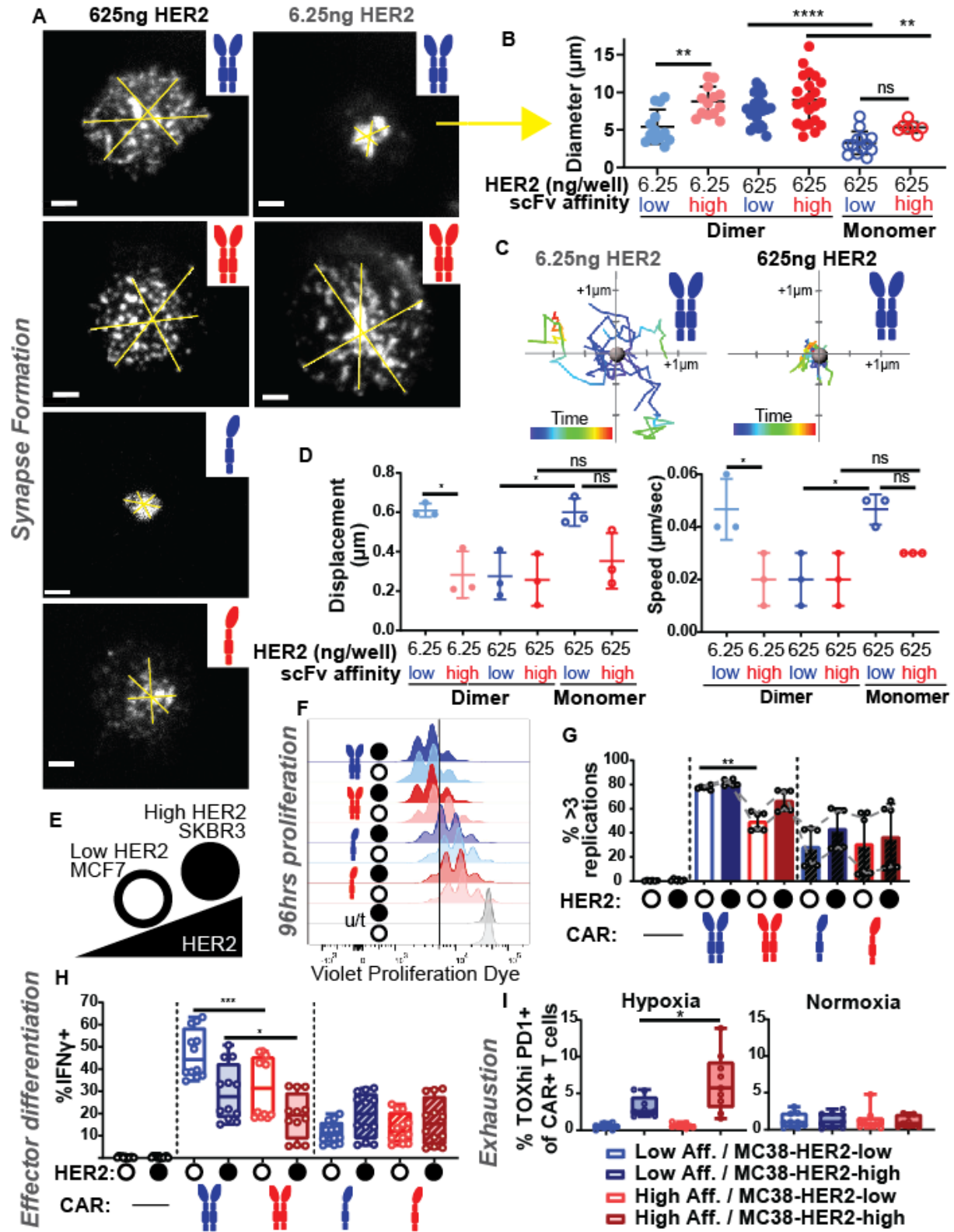
Figure 3.9. Impaired movement of high affinity dimer CAR microclusters in synapses and reduced effector function.

(A-B) TIRF imaging of CAR-mEmerald is shown for synapses with low- or high-affinity CAR interacting with low or high HER2-loaded bilayers (A). Time point shown is 93.6 seconds following the initiation of imaging, which began as synapses were starting to form. Yellow lines were drawn to span CAR microclusters in synapse, indicating diameter quantified in B. Three lines were averaged and line assignment was blinded to account for manual drawing. For dimeric CARs, only low affinity:low HER2 synapses result in accumulation of CAR microclusters at the center, indicated by lower diameter. Monomerization of CARs improves centralization on high HER2. Data is shown for at least 7 cells pooled from a minimum two independent experiments per condition (n = 13, 13, 20, 20, 13, 7 cells per group from left to right, respectively). Error bars represent s.d. Analyses shown are Šídák's multiple comparisons tests. Scale bars = 2 μm. **(C-D)** Spots with tracking were assigned to CAR microclusters in Imaris. Examples of mobile (left, low affinity dimer on low HER2) and immobile (right, low affinity dimer on high HER2) microclusters are shown as a flower plot for 10 random tracks (C). Quantification is shown for the average displacement (left) and speed (right) of all CAR microclusters for a given cell (D, n = 3 cells per group). Limited mobility is apparent for dimeric CARs on high-HER2 loaded bilayers. On low-HER2 bilayers, low-affinity CAR microclusters show increased mobility. Error bars represent s.d. Analyses shown are Šídák's multiple comparisons tests. **(E)** Low HER2-expressing MCF7 (open circle) and high HER2-expressing SKBR3 (solid circle) cell lines were used to assess differences between HER2 levels in cell-cell interactions in vitro. **(F)** Proliferation is induced across all CAR+ conditions with low and high HER2, as seen by VPD dilution at 96 hrs following co-incubation. Line marks VPD dilution indicating at least 3 replication cycles (quantified in F). **(G)** Percentage of cells that have undergone at least 3 replication cycles. Replicates from 2 independent experiments of different donors are pooled (n = 6). Dashed lines indicate individual donor trends. Error bars represent s.d. Analysis shown is Šídák's multiple comparisons test. **(H)** Intracellular staining with anti-IFN-γ-APC at 18hrs following co-incubation. Low-affinity CAR induces greater IFN-γ than high-affinity. Monomeric low-affinity CAR has overall lower magnitude of response, but improves the dose response. Box and whiskers plot error bars showing minimum and maximum values (n = 12 samples per group pooled from four independent experiments and two donors). Analyses shown are Šídák's multiple comparisons tests. **(I)** Low-affinity (blue) and high-affinity (red) CARs were retrovirally expressed in primary mouse CD8+ T cells and co-cultured with MC38s expressing low- or high-HER2 for 24 hrs in normoxia (20% oxygen) before separation into normoxic or hypoxic (1.5% oxygen) cultures for an additional six days. Hypoxic co-cultures of high-affinity CAR T cells with MC38-HER2-high cells have significantly more TOX high/ PD1+ cells than low-affinity CAR T cells, indicative of development towards an exhausted state. Box and whiskers plot error bars showing minimum and maximum values (n = 9 samples pooled from 3 independent experiments). Analysis shown is unpaired t test.
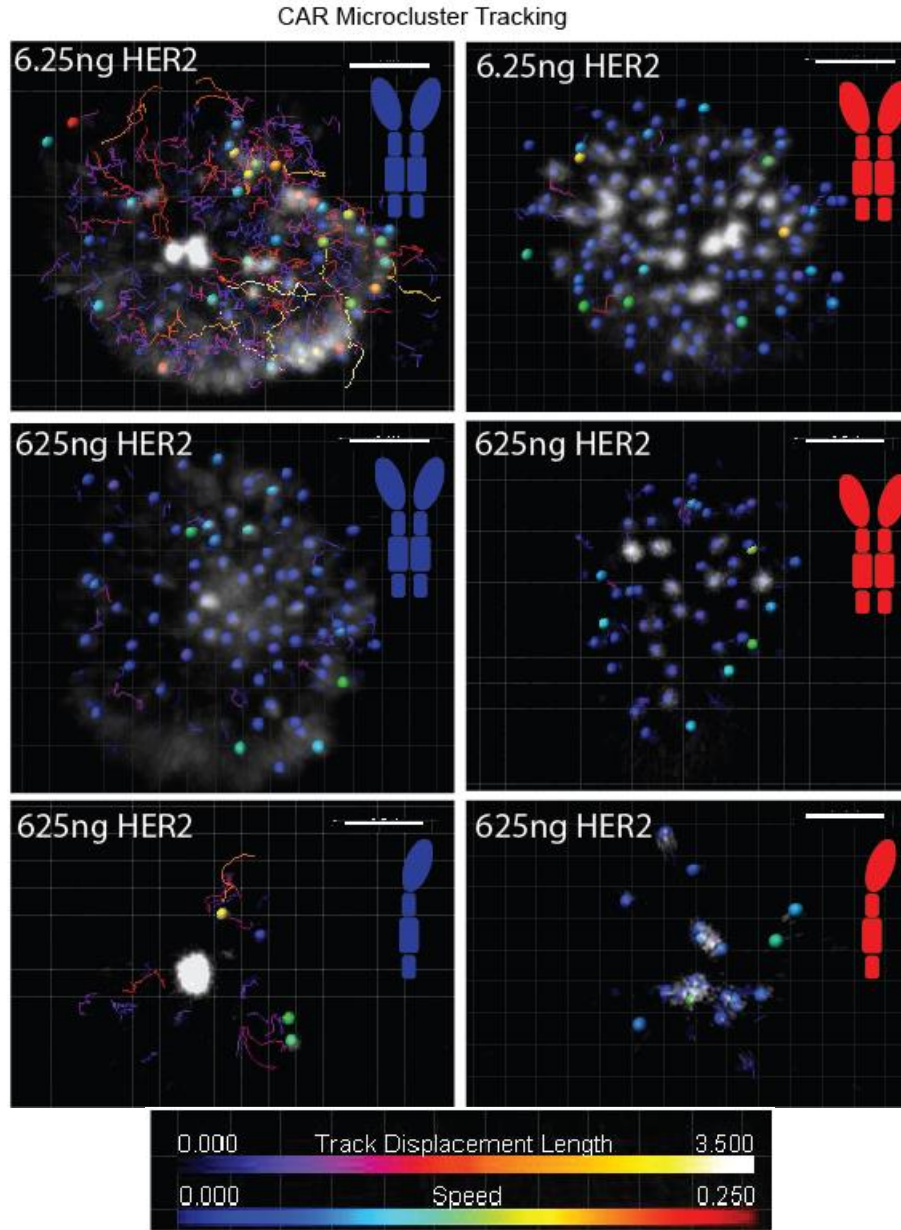
Figure 3.10. CAR microcluster tracking.
TIRF imaging of CAR-mEmerald is shown with spots and tracks made in Imaris. Tracks analysis shows that high-affinity CAR microclusters on low HER2 (6.25 ng/well) are not mobile, and on high HER2 (625 ng/well) only low-affinity monomer is mobile. Scale bars = 3 μm.
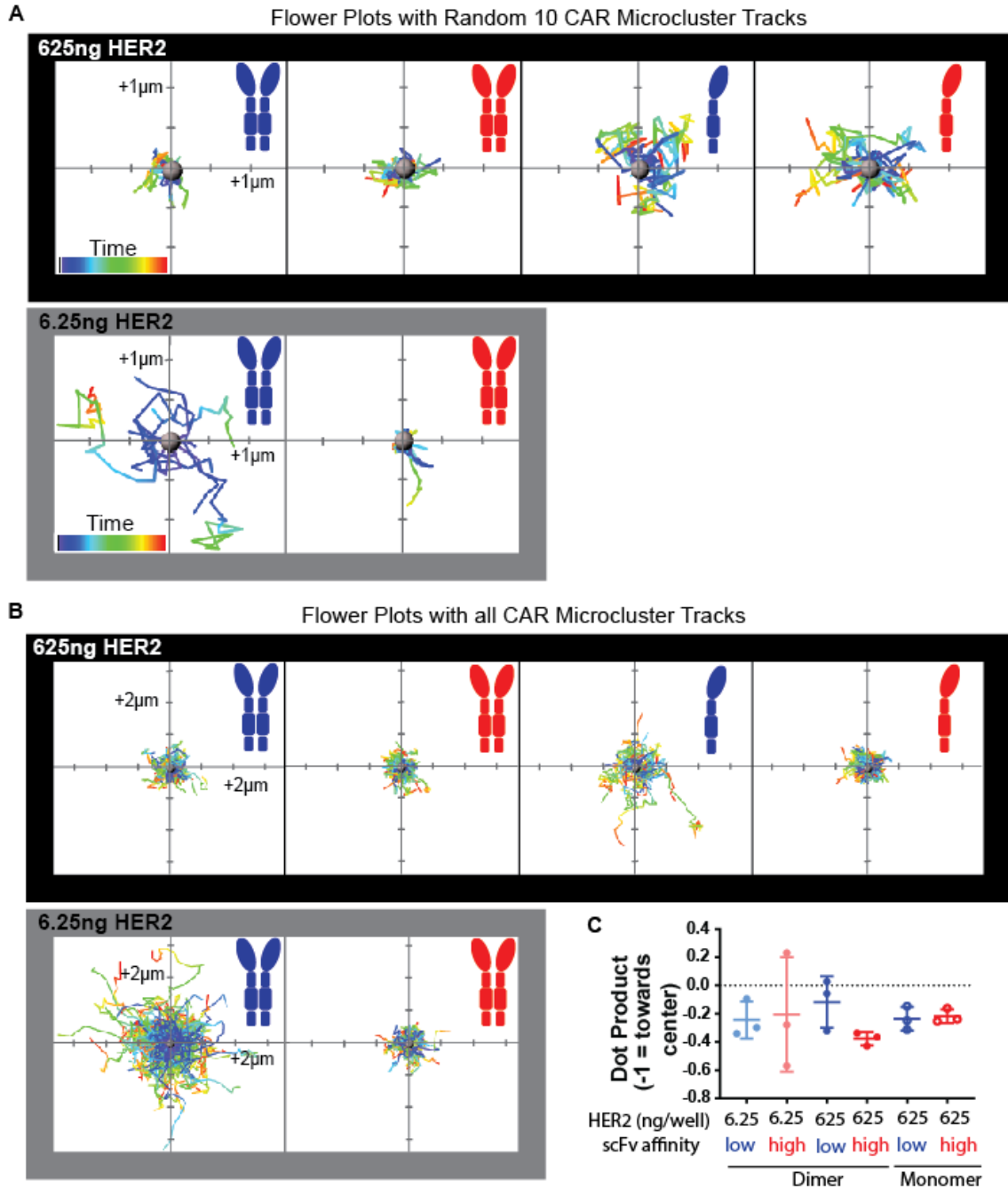
Figure 3.11. CAR microcluster dynamics.
(A-B) A random 10 (A) or all (B) tracks are shown in flower plots for each condition. Top: Limited mobility is apparent for dimeric CARs on high-HER2 loaded bilayers. Bottom: On low-HER2 bilayers, low-affinity CAR microclusters show increased mobility. Plots of low affinity dimer from Fig. 3.9c are shown again here for comparison. **(C)** The normalized dot product of V(rad) and V(i) was calculated for all tracks, where V(rad) = vector from synapse center to track start position and V(i) = vector from track start to track final position. Using this calculation, movements directly towards the center equal -1 and movements directly away from center equal 1. The average dot product for all tracks in a cell are quantified. No significant differences are identified in the direction of CAR microcluster movement across conditions. All n.s. by Tukey's multiple comparisons test.

93
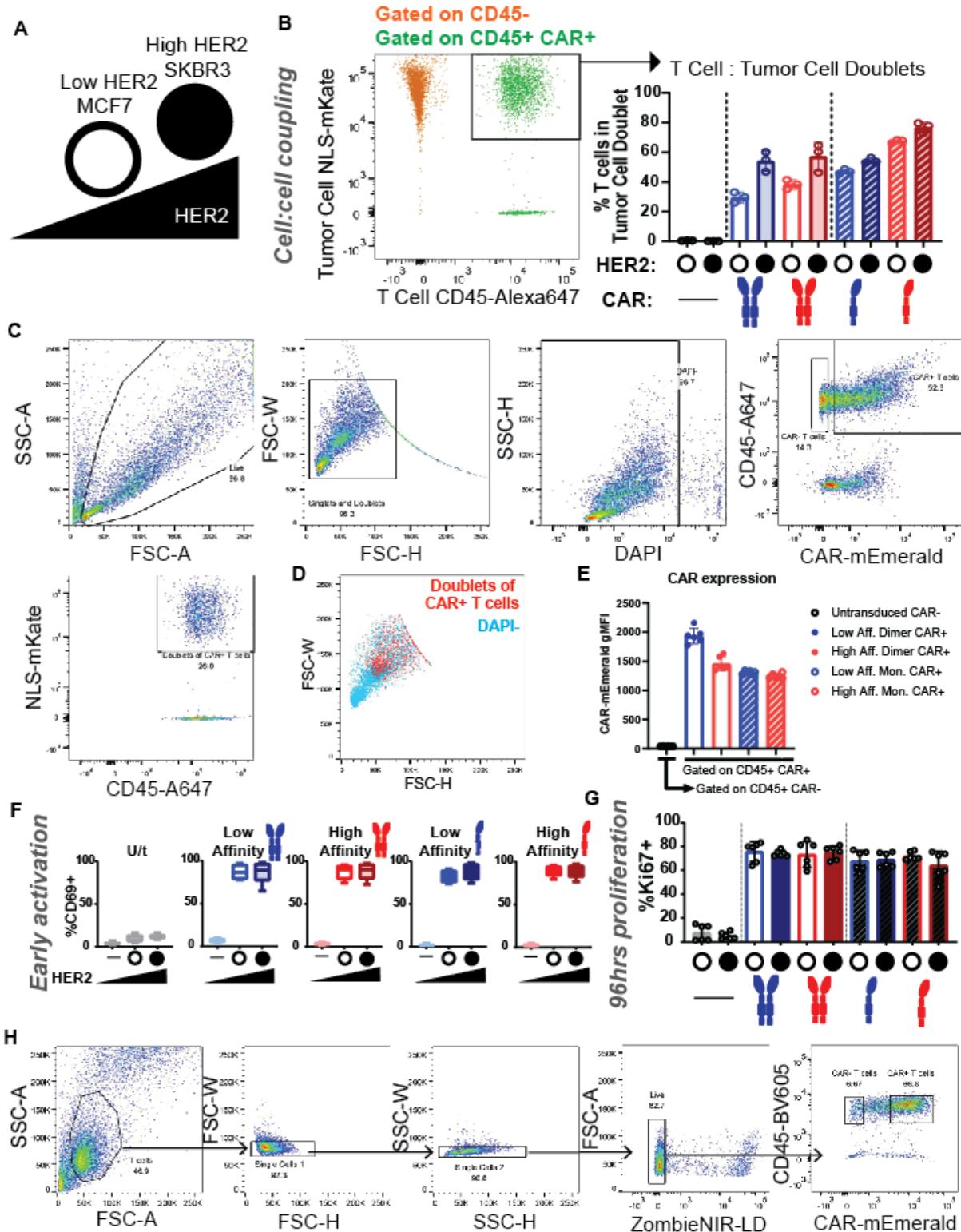
Figure 3.12. CAR T cell:target cell co-cultures.
(A) Low HER2-expressing MCF7 (open circle) and high HER2-expressing SKBR3 (solid circle) cell lines were used to assess differences between HER2 levels in cell-cell interactions in vitro. **(B)** MCF7 and SKBR3 cells expressing nuclear localization signal (NLS)-tagged mKate were incubated with anti-CD45-Alexa647-labelled T cells for 30 minutes. Coupling analysis was

performed by gating inclusively for singlets and doublets. Cells were then gated on DAPI-, CD45+, and CAR+ (or CAR- for untransduced controls). Percentage of these cells that are mKate+ was reported as T cells in doublets with tumor cells (right). Representative dot plot for the high affinity monomeric CAR T cell / SKBR3 co-culture is shown overlaying the CD45- and CD45+CAR+ populations (left). Representative of three independent experiments is shown. **(C)** Gating strategy for coupling assay in (B). Example data here is from a co-culture of low-affinity dimeric CAR T cells with MCF7 target cells. **(D)** The entire DAPI- population in (C) is overlaid with the Doublets of CAR+ T cells population. Plotting by FSC-H vs FSC-W shows that the Doublets of CAR+ T cells population falls in the expected region (above the singlets). **(E)** CAR gMFIs are shown for each receptor type. While there is some variability in expression, differences are within ~2/3rds of the highest gMFI. **(F)** Early activation is similar across all CAR+ conditions with low and high HER2 at 18 hours following co-incubation, as seen by anti-CD69-BUV395 positivity. Box and whiskers plot error bars showing minimum and maximum values (n = 12 samples per group pooled from four independent experiments and two donors). **(G)** Percentage of anti-Ki67-PE-eFluor 610 positive cells, indicating entry into cell cycle, is similar across all CAR+ conditions with low and high HER2. Replicates from 2 independent experiments of different donors are pooled (n = 6). Error bars represent s.d. **(H)** Gating strategy used for defining human CAR+ (and CAR-) T cells in flow cytometry experiments is shown. Example data shown here is from a co-culture of low-affinity dimeric CAR T cells with SKBR3 target cells.
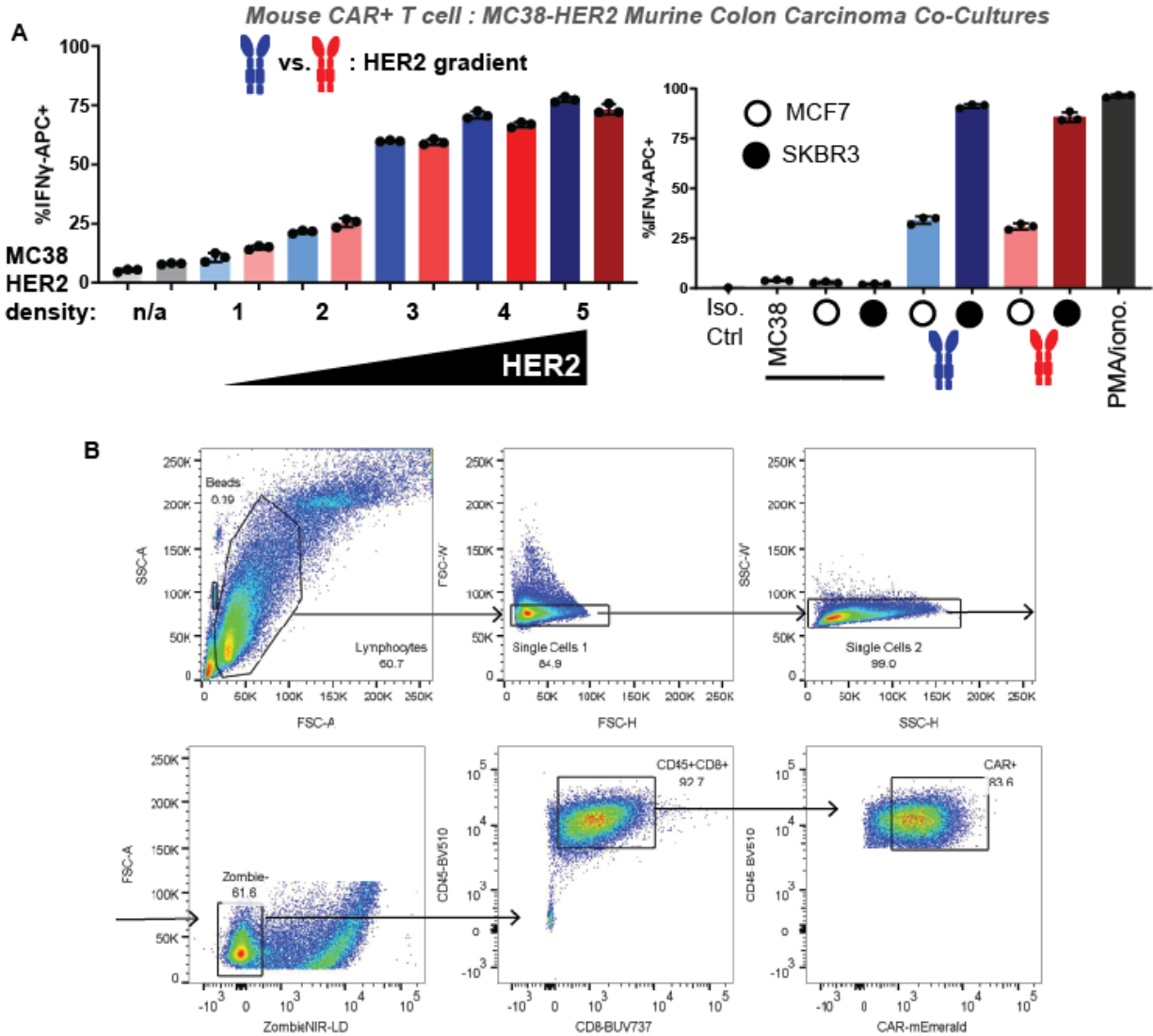
Figure 3.13. Mouse CAR T cell co-cultures with MC38-HER2.
(A) Low-affinity (blue) and high-affinity (red) CARs were retrovirally expressed in primary mouse CD8+ T cells. HER2-expressing MC38 cells were sorted into 5 bins of expression levels. MC38-HER2 (1-5) and parental MC38 (n/a) were cultured with CAR T cells for 18 hours and then stained for IFN-γ. Low- and high-affinity CARs performed similarly. Isotype control, untransduced T cell, MCF7 (open circle), SKBR3 (filled circle), and PMA/ionomycin controls are shown on the right. n = 3 replicates per group. Data shown is representative of 3 independent experiments. **(B)** Gating strategy used for defining mouse CAR+ T cells in flow cytometry experiments following in vitro co-culture is shown. Example data shown here is from a co-culture of low-affinity dimeric CAR T cells with MC38-HER2-high targets in normoxia.

Tables

Table 3.1. Mutations in CAR scFv (mutCD45) and CD8α hinge/TMD (monomer).

scFv sequence

```
4D5                  1  DIQMTQSPSSLSASVGDRVTITCRASQDVNTAVAWYQQKPGKAPKLLIYS 50
mut4D5_Low Affinity  1  .................................................. 50

4D5                 51  ASFLYSGVPSRFSGSRSGTDFTLTISSLQPEDFATYYCQQHYTTPPTFGQ 100
mut4D5_Low Affinity 51  ....E..........G.................................. 100

4D5                101  GTKVEIKRTGSTSGSGKPGSGEGSEVQLVESGGGLVQPGGSLRLSCAASG 150
mut4D5_Low Affinity 101 .V................................................ 150

4D5                151  FNIKDTYIHWVRQAPGKGLEWVARIYPTNGYTRYADSVKGRFTISADTSK 200
mut4D5_Low Affinity 151 .................................................. 200

4D5                201  NTAYLQMNSLRAEDTAVYYCSRWGGDGFYAMDVWGQGTLVTVSSGS 246
mut4D5_Low Affinity 201 .............................................. 246
```

CD8α hinge/TMD sequence

```
CD8alpha_WT        1  TTTPAPRPPTPAPTIASQPLSLRPEACRPAAGGAVHTRGL 40
CD8alpha_monomer   1  ............................S........... 40

CD8alpha_WT       41  DFACDIYIWAPLAGTCGVLLLSLVITLYC 69
CD8alpha_monomer  41  ...S......................... 69
```

Table 3.2. Antibodies referenced for flow cytometry and imaging experiments.

Anti-	Clone	Fluorophore	Company	Cat. No.
Myc-Tag	9B11	Alexa Fluor 488	Cell Signaling Tech.	2233S
human CD3	OKT3	APC	BioLegend	317318
human CD340 (HER2)	24D2	Brilliant Violet 605	BD Biosciences	747615
human CD340 (HER2)	24D2	Alexa Fluor 647	BioLegend	324412
human CD340 (HER2)	24D2	PerCP/Cy5.5	BioLegend	324416
human CD45	HI30	Alexa Fluor 594	BioLegend	304060
human CD45	HI30	Alexa Fluor 647	BioLegend	304056
human CD45	HI30	Brilliant Violet 605	BioLegend	304042
human CD69	FN50	BUV395	BD Biosciences	564364
human IFN-γ	4S.B3	APC	BioLegend	502512
human/mouse Ki67	SolA15	PE-eFluor 610	eBioscience	61-5698-82
mouse CD223 (LAG3)	C9B7W	Brilliant Violet 785	BioLegend	125219
mouse CD279 (PD-1)	29F.1A12	Brilliant Violet 421	BioLegend	135221
mouse CD279 (PD-1)	29F.1A12	Brilliant Violet 605	BioLegend	135220
mouse CD39	Duha59	PE-Cy7	BioLegend	143806
mouse CD4	GK1.5	BUV395	BD Biosciences	563790
mouse CD44	IM7	BUV737	BD Biosciences	564392
mouse CD45	30-F11	Brilliant Violet 421	BioLegend	103134
mouse CD45	30-F11	Brillian Violet 510	BioLegend	103138
mouse CD45	30-F11	Brilliant Violet 785	BioLegend	103149
mouse CD45.1	A20	PE-Cy7	BioLegend	110730
mouse CD62L	MEL-14	APC	BioLegend	104411
mouse CD69	H1.2F3	BUV395	BD Biosciences	740220
mouse CD69	H1.2F3	Brillian Violet 650	BioLegend	104541
mouse CD8a	53-6.7	BUV737	BD Biosciences	564297

Anti-	Clone	Fluorophore	Company	Cat. No.
mouse CD8a	53-6.7	PerCP/Cy5.5	BioLegend	100734
mouse CD90.2	30-H12	Alexa Fluor 700	BioLegend	105320
mouse IFN-γ	XMG1.2	APC	BioLegend	505810
mouse NK1.1	PK136	Brilliant Violet 785	BioLegend	108749
mouse TCR β chain	H57-597	Alexa Fluor 488	BioLegend	109215
mouse/human CD11b	M1/70	Brilliant Violet 785	BioLegend	101243
mouse/human CD324 (E-cadherin)	DECMA-1	PE	BioLegend	147303
mouse/human CD45R	RA3-6B2	Brilliant Violet 785	BioLegend	103246
mouse/human TOX	REA473	APC	Miltenyi Biotec	130-118-335

Supplemental Files

Movie 3.1. LLS imaging of anti-HER2 CAR T cell.

Maximum intensity projection of anti-HER2 CAR-expressing T cell shown in Fig. 1a. Location of coverslip, where signal intensity is low, is annotated in yellow. Anti-CD45-Alexa594, anti-MYC (CAR)-Alexa488 and TCR (OKT3)-APC signal is shown in cyan, green and red, respectively.

Movie 3.2. LLS live cell imaging of anti-HER2 CAR T cell in synapse with HER2+ SKBR3 cell.

The blended view of the Imaris volume is shown for anti-HER2 CAR-expressing T cell shown in Fig. 3.5a. The SKBR3 target cell is located above, as annotated in Fig. 3.5a. Anti-CD45-Alexa647 and anti-MYC (CAR)-Alexa488 signals are shown in red and green, respectively. Scale bar = 2 μm. Time resolution per frame is 4.7 secs and total video is 20 frames (89.3 secs).

Movie 3.3. Individual close contacts imaged by SCM TIRF microscopy.

QD605 signal is shown for one field of view for low-affinity (top) and high-affinity (bottom) CAR T cells interacting with HER2-loaded bilayer. Holes in QD605 signal show location of microvillar close contacts. High-affinity close contact stably persists in same field of view, while low-affinity CAR T cell contacts appear and disappear from field of view throughout imaging. Scale bar is 0.2 μm. Time resolution per frame is 2.4 secs and total video is 40 frames (93.6 secs).

Movie 3.4. Fura-2 calcium flux imaging of low- and high-affinity CAR T cells on low- and high-HER2 bilayers.

Fura-2 340nm/380nm ratio channel with tracking is shown for A) low affinity/0 ng HER2, B) low affinity/62.5 ng HER2, C) low affinity/625 ng HER2, D) high affinity/62.5 ng HER2, and E) high affinity/625 ng HER2 (from top to bottom) CAR T cells interacting with loaded bilayers. Calcium

flux (yellow) is seen for interactions of CAR T cells with HER2-bilayers across antigen density and CAR affinity, relative to no HER2 control (A). Scale bar is 7 µm. Imaging was initiated at 3 min following addition of T cells to wells. Time resolution per frame is 1.5 secs and total video is 100 frames (148.5 secs).

Movie 3.5. CAR microcluster tracking analysis – low-affinity dimer on low HER2 bilayer.

TIRF imaging of CAR-mEmerald is shown for low-affinity dimeric CAR on bilayer loaded with 6.25 ng/well. Spots show position of microclusters used for tracking. Scale bar is 3 µm. Time resolution per frame is 2.4 secs and total video is 40 frames (93.6 secs).

Movie 3.6. CAR microcluster tracking analysis – high-affinity dimer on low HER2 bilayer.

TIRF imaging of CAR-mEmerald is shown for high-affinity dimeric CAR on bilayer loaded with 6.25 ng/well. Spots show position of microclusters used for tracking. Scale bar is 3 µm. Time resolution per frame is 2.4 secs and total video is 40 frames (93.6 secs).

Movie 3.7. CAR microcluster tracking analysis – low-affinity dimer on high HER2 bilayer.

TIRF imaging of CAR-mEmerald is shown for low-affinity dimeric CAR on bilayer loaded with 625 ng/well. Spots show position of microclusters used for tracking. Scale bar is 3 µm. Time resolution per frame is 2.4 secs and total video is 40 frames (93.6 secs).

Movie 3.8. CAR microcluster tracking analysis – high-affinity dimer on high HER2 bilayer.

TIRF imaging of CAR-mEmerald is shown for high-affinity dimeric CAR on bilayer loaded with 625 ng/well. Spots show position of microclusters used for tracking. Scale bar is 3 µm. Time resolution per frame is 2.4 secs and total video is 40 frames (93.6 secs).

Movie 3.9. CAR microcluster tracking analysis – low-affinity monomer on high HER2 bilayer.

TIRF imaging of CAR-mEmerald is shown for low-affinity monomeric CAR on bilayer loaded with 625 ng/well. Spots show position of microclusters used for tracking. Scale bar is 3 µm. Time resolution per frame is 2.4 secs and total video is 40 frames (93.6 secs).

Movie 3.10. CAR microcluster tracking analysis – high-affinity monomer on high HER2 bilayer.

TIRF imaging of CAR-mEmerald is shown for high-affinity monomeric CAR on bilayer loaded with 625 ng/well. Spots show position of microclusters used for tracking. Scale bar is 3 µm. Time resolution per frame is 2.4 secs and total video is 40 frames (93.6 secs).

Materials and Methods

Lentiviral and retroviral CAR constructs

All CARs were fused to C-terminal MYC tag, CD8α hinge/transmembrane domain, 4-1BB co-stimulatory domain, CD3ζ signaling domain, and an N-terminal mEmerald tag. Monomeric versions of each CAR were created by using the Q5 Site Directed Mutagenesis Kit (NEB #E0554S) yielding two cysteine to serine point mutations in the CD8α hinge[100] (**Table 3.1**).

Human T cell culture, lentiviral transduction, and co-incubations

Lenti-X 293T cells (Takara Bio) were transfected with pHR SIN including cloned transgene and packaging vectors pMD2.G and pCMVdR8.91 using TransIT-Lenti Transfection Reagent (Mirus #MIR6603). On the day of transfection, primary human CD8+ T cells were thawed into complete human T cell media: X-VIVO 15 (Lonza # 04-418Q), 5% Human AB serum (Valley Biomedical #HP1022) and 10 mM neutralized N-acetyl L-Cysteine (Sigma Aldrich #A9165-25G) supplemented with 30 U/mL recombinant human IL-2 (R&D Systems #202-IL), and 55 μM beta-mercaptoethanol (Thermo # 21985023). The following day, Human T-Activator CD3/CD28 Dynabeads (Thermo #11161D) were added at 1:1 ratio with thawed T cells. The next day, T cell media was replaced with Lenti-X 293T viral supernatant. For lentiviral transduction of monomeric CARs, virus was concentrated by PEG/NaCl precipitation, and stored at -80° C prior to use. Viral supernatant was replaced with fresh T cell media the next day, and T cells were allowed to recover for one day prior to Dynabead removal and sort. Cells were sorted for CAR-mEmerald expression in the range of 1-2 logs above background. Cells were then rested and used at 10-21 days post initial stimulation. Lenti-X 293T cells were cultured in Dulbecco's modified Eagle's medium (DMEM, Gibco #11995) with 10% fetal bovine serum (MilliporeSigma), penicillin (50 U/ml) and streptomycin (50 μg/ml) (MP Biochemicals #MP091670049), and 1 mM sodium pyruvate (Sigma-Aldrich #S8636). For early activation and intracellular cytokine assays,

5×10^4 T cells were added at a 1:1 ratio to 96-well flat-bottom plates with MCF7 (ATCC) or SKBR3 (ATCC) cells for 18 hours. BD GolgiPlug (#555029) was added for the final 10 hours. For proliferation assays, T cells were stained with Violet Proliferation Dye (BD #562158) prior to plating of 2×10^4 T cells at 1:1 ratio with MCF7s or SKBR3s. Complete T cell media was supplemented the following day, and cells were analyzed by flow cytometry at 96 hours following plating.

Flow cytometric analysis

Zombie NIR Fixable Viability Kit (BioLegend #423106) was used for exclusion of dead cells. Surface staining was performed with anti-mouse Fc receptor antibody (clone 2.4G2, UCSF Hybridoma Core) or Human TruStain FcX (BioLegend #422302) in PBS with 2% FCS for 30 min on ice. **Table 3.2** lists all antibodies referenced for flow cytometry and imaging experiments. For experiments with staining of nuclear proteins, eBioscience Foxp3 / Transcription Factor Staining Buffer Set (Fisher Scientific #00-5523-00) was used for fixation and permeabilization. For all other experiments involving intracellular staining, BD Cytofix/Cytoperm (#554722) was used. Following fixation and permeabilization, cells were incubated with Fc block for 10 min on ice prior to addition of intracellular stain. Flow cytometry was performed on a BD Fortessa instrument, and sorting was performed on BD FACSAria or BD FACSAria Fusion instruments. FlowJo software (BD Biosciences) was used for all analyses. Flow-cytometry based coupling assay was performed as previously described[205] on unfixed cells using DAPI for live/dead discrimination.

Mice

C57BL/6J and B6.SJL-Ptprc[a] Pepc[b]/BoyJ (CD45.1) mice, used as sources of primary mouse T cells, were housed and bred at the University of California, San Francisco, according to Laboratory Animal Resource Center guidelines. Protocols were approved by the Institutional Animal Care and Use Committee of the University of California.

MC38-HER2 retroviral transduction

Truncated HER2, without intracellular signaling domains, (NP_004439.2; amino acids 1 to 730) was cloned into pIB2 retroviral vector. Phoenix cells were transfected using FuGENE 6 Transfection Reagent (Promega #E2691), and retroviral supernatant was collected and used immediately for transfection of MC38s on days 2 and 3 following transfection. Two days after the second transduction, cells were sorted for expression of HER2 (stained with anti-HER2-A488). MC38-HER2 cells were then expanded and the retroviral transduction process was repeated. Following the second transduction, cells were then sorted into high-, medium-, and low-expression levels using MCF7 and SKBR3 cells as standards for low and high expression, respectively. MC38 cells were cultured in DMEM (Gibco #11995) supplemented with 10% fetal bovine serum (Benchmark), 100 U/mL penicillin, 0.1 mg/mL streptomycin, 2 mM L-glutamine (Gibco #10378), 10 mM HEPES (Thermo #15630106), and 55 µM beta-mercaptoethanol (Thermo # 21985023).

Murine T cell culture, retroviral transduction, and functional assays

The mouse OT-I TCR system was chosen as a comparator to the anti-HER2 CAR for its affinity near the top of the common range, and in order to avoid double-transfection (of a human TCR along with a CAR) which otherwise would create significant experimental inefficiencies. For all experiments using murine T cells, cells were maintained in RPMI (Gibco #11875) supplemented with 10% fetal bovine serum (Benchmark), 100 U/mL penicillin, 0.1 mg/mL streptomycin, 2 mM L-glutamine, 10 mM HEPES (Thermo #15630106), 55 µM beta-mercaptoethanol (Thermo # 21985023), non-essential amino acids (Thermo #11140050), 1mM sodium pyruvate (Sigma-Aldrich #S8636), and supplemented with 100 U/ml IL-2, which is referred to as complete RPMI. Single cell suspensions were prepared from the lymph nodes and spleens of C57BL/6J, *Ptprc^a* (CD45.1), or OT-I TCR transgenic mice. Following red blood cell lysis of splenocytes, negative selection using the EasySep Mouse T Cell or CD8+ T cell Isolation Kit (STEMCELL

Technologies #19853) was used to isolate CD8+ T cells. T cells were activated in complete RPMI using CD3/CD28 Mouse T activator Dynabeads (Thermo #11-453-D) for 24 hours before the first round of retroviral transduction.

For retrovirus production, Platinum-E cells were transfected with pMIG including CAR transgene using FuGene. Transfections were performed in DMEM (Gibco #11995) supplemented with 10% fetal bovine serum (Benchmark) and 10 mM HEPES (Thermo #15630106), which was replaced with complete RPMI (without IL-2) the following day. Retroviral supernatants were harvested at day 2 and 3 and stored in -80°C. Platinum-E cells were maintained in DMEM (Gibco #11995) supplemented with 10% fetal bovine serum (Benchmark), 100 U/mL penicillin, 0.1 mg/mL streptomycin, 2 mM L-glutamine (Gibco #10378), 10 mM HEPES (Thermo #15630106), 10 µg/ml blasticidin (Fisher Scientific #A1113903) and 1 µg/ml puromycin (Gibco #A1113803).

For T cell retroviral transduction, retroviral supernatant was added to T cells in retronectin-coated plates at 24 and 48 hours following initial stimulation, and the plates were centrifuged for 1 hour at 2,000g and 30°C. After the second spinfection, cells were rested two days prior to Dynabead removal (4 days post-stim). T cells were then sorted for imaging or rested for an additional 6-7 days in 10 ng/ml recombinant murine IL-7 (PeproTech #217-17) and 100 U/ml IL-2 and used for in vitro co-culture experiments.

For binned HER2 expression level experiments, MC38-HER2 lines were sorted into 5 consecutive bins by HER2 expression using MCF7s and SKBR3s as the low and high HER2 standards, respectively. MC38-HER2 cells, sorted as described, were then plated at $5x10^4$ cells/well in flat-bottom 96 well plates, and $5x10^4$ T cells were then added, bringing the total volume to 200 µl/well complete RPMI. For hypoxia experiments, T cells were rested 6 days and then plated at $5x10^4$ cells at a 1:1 ratio with MC38-HER2-high or MC38-HER2-low cells in two

96-well plates in complete RPMI. At 24 hours, wells were replenished with complete RPMI + IL-2, and $5x10^4$ MC38-HER2-high and -low cells were added. One plate was moved to 1.5% oxygen while the second was maintained at 20% oxygen. MC38-HER2-high and -low cells and media + IL-2 were then replenished every two days until analysis on day 7 after start of co-culture (6 days in hypoxia).

Surface plasmon resonance affinity measurements

Measurements were taken using a Biacore T200 instrument with CM4 sensor chip and HBs-EP+ buffer. HER2-mIgG2aFc (ACROBiosystems #HE2-H5255) was captured using anti-mIgG (50 RUs). Association and dissociation times were 120 and 900 sec, respectively. Concentrations of scFv used for single cycle kinetics analysis: 0.33, 1, 3, 9, 27 nM.

Lattice Light-Sheet Microscopy

Lattice light-sheet imaging was performed as described previously[188]. 5 mm round coverslips were cleaned by a plasma cleaner and coated with 2 μg/ml fibronectin in PBS at 37°C for 1 hour, or at 4°C overnight, before use. ~3×10^5 CAR T cells were loaded onto the coverslip and incubated at 37°C for 30 min. Cells were then fixed in $d_2h_2 0$ with 20 mM HEPES (Thermo #15630106), 0.2 M sucrose (RPI #S240600, 4% paraformaldehyde (Election Microscopy Sciences #15710), and 8% glut-aldehyde (Election Microscopy Sciences #16019) for 10 min at room temperature. Coverslip was washed gently in 1 ml PBS and then stained with antibodies to CD45 and/or MYC with anti-mouse Fc receptor antibody (clone 2.4G2, UCSF Hybridoma Core). Samples were stained for at least 30 min and kept at 4°C until use. Prior to imaging, coverslip was gently washed with 1 ml warmed RPMI without phenol red (Gibco #11835) supplemented with 2% fetal bovine serum, 100 U/mL penicillin, 0.1 mg/mL streptomycin, 2 mM L-glutamine, 10 mM HEPES and 50 μM β-mercaptoethanol (imaging media). For imaging of live CAR T cell interactions with MCF7 and SKBR3 targets, MCF7 or SKBR3 cells were plated onto fibronectin-coated coverslips 1-2 days prior to imaging, or onto Cell-Tak (Corning #354240)

coated coverslips with a 10 min spin at 1400 rpm and 4°C. CAR T cells were stained with antibody to CD45-Alexa647 for 30 min on ice. Target cells on coverslip were stained with CFSE (Invitrogen #C34554) for 20 min at 37°C, or were identified by nuclear-localized mKate expression. Cells were then washed and T cells were added onto the coverslip prior to being loaded into the sample bath with warmed imaging media and secured. Imaging was performed with a 488 nm, 560 nm, or 642 nm laser (MPBC, Canada) dependent upon sample labeling. Exposure time was 10 ms per frame leading to a temporal resolution of ~4.5 and ~6.75 seconds in two- and three-color mode respectively.

Supported lipid bilayers, synaptic contact mapping, and calcium flux imaging

Preparation and use of supported lipid bilayers was performed as described previously[50,188]. Mixtures of 96.5% POPC, 2% DGS-NTA (Ni), 1% Biotinyl-Cap-PE and 0.5% PEG5,000-PE (Avanti Polar Lipids #850457C, 790404C, 870273C, 880230C) were made in a round bottom flask and dried under a stream of nitrogen and then overnight under vacuum. The phospholipids were then rehydrated at a total concentration of 4 mM in PBS for one hour to create crude liposomes. Small, unilamellar liposomes were then made by extruding through 100 nm Track Etch filter papers (Whatman #800309) with an Avestin LiposoFast Extruder (Avestin).

8-well Nunc Lab-Tek II chambered coverglass (Thermo #155360) were cleaned by submersion in 5% Hellmanex III (Sigma-Aldrich #Z805939). Flask containing chamber in solution was microwaved for 25 sec and then allowed to clean at room temperature overnight. The chambers were then washed repeatedly with 18 Milli-Q water and then dried. Finally, 250 µl 3M NaOH was added to each well for 15 min at 55°C. Wells were washed with 300 µl Milli-Q water and the NaOH cleaning was repeated. Wells were then washed thoroughly and dried prior to use. Lipid bilayers were set up on the chambered coverglass by adding 0.25 mL of a 0.4 mM liposome solution to the wells. After 30 minutes, wells were rinsed with 8 mL of PBS by repeated addition

of 0.5 mL of PBS, then aspiration of 0.5 mL of the overlay. Non-specific binding sites were then blocked with 1% BSA in PBS for 30 minutes. After blocking, 25 ng of unlabeled streptavidin (Invitrogen #43-4301) was added to each well and allowed to bind to bilayers for 30 minutes. After rinsing, protein mixes containing 63 ng recombinant human ICAM-1 (Abcam #AB151393) and 6.25-625 ng biotinylated HER2 (ACROBiosystems #HE2-H822R) or 6 ng pMHC in 2% BSA were injected into each well. pMHC was provided by the NIH Tetramer Facility. After binding for 30 minutes, wells were rinsed again and 25 ng of QDot605-streptavidin (Thermo #Q10101MP) was added to each well. For calcium flux imaging, QDot605-streptavidin was not added. Bilayers were finally rinsed with imaging media before being heated to 37°C for experiments. Experiments using 5 µm diameter silica microspheres (Bangs Laboratories #SS05003/SS05N) were performed as previously described[203]. Briefly, the same protocol was used for building a lipid bilayer on chamber coverglass as for $4x10^5$ beads, based off equivalent surface area, but with washes performed by centrifugation instead of repeated aspiration.

For synaptic contact mapping (SCM) experiments, 5×10^5 T cells were added to the well prior to imaging. Once cells began interacting with the bilayer, imaging was initiated. For imaging of OT-I TCR, $1-2\times10^6$ OT-I T cells were stained with 2.5 µg H57-597 non-blocking monoclonal antibody conjugated to Alexa Fluor 488 on ice for 30 minutes, then rinsed once with complete imaging media. Imaging for synaptic contact mapping was performed as described previously[188]. The TIRF microscope is based on a Zeiss Axiovert 200M equipped with a 100x 1.45NA oil immersion objective, DG-4 Xenon light source (Sutter) and Zeiss TIRF slider[50,188]. All images were collected using a DV2 image splitter (Photometrics) positioned in front of an Evolve EMCCD (Photometrics). A 4 band multi-color TIRF dichroic located in the microscope separated the excitation and emission light for imaging (Chroma Technology). Images of CAR or TCR were collected by imaging CAR-mEmerald (or Alexa Fluor 488-labeled TCRs) using TIRF mode, by imaging QD605-streptavidin in widefield mode, and by imaging cells with

interference reflection microscopy (IRM), also in widefield mode. Widefield QD605-strepavidin images were collected using a 405/10 nm excitation filter (Chroma Technology) located in the DG4 light source, while samples imaged with TIRF were excited by an Obis 488nm laser (Coherent). IRM images were acquired using a 635/20 nm excitation filter (Chroma Technology) positioned in the DG4 light source. The CAR/TCR and QD605 emitted fluorescence signals were separated using a DV2 image splitter with a 565 nm long-pass dichroic mirror installed along with 520/35 nm and 605/70 nm emission filters (Chroma). Images containing the IRM signal were acquired through the long-pass dichroic and 605/70 nm emission filter in the image splitter. For Fura-2 imaging, cells were stained with 2 µM Fura-2 dye (Thermo #F1221) for 15 min at room temperature. Cells were then washed in imaging media, and 5×10^{5} T cells were added to the imaging well. 3 min after addition of cells, acquisition was initiated. Fura-2 imaging experiments were acquired using a 40x 1.3NA oil immersion objective (Zeiss) and the same light source and dichroic described above. Widefield Fura-2 340 nm and 380 nm images were collected using 340/26 (Semrock, Rochester, NY) and 380/30 (Chroma, VT) excitation filters, respectively, located in the DG4 light source.

Image analysis

All computational image analysis for SCM imaging was performed in Matlab (The Mathworks, Natick, MA), Imaris version 9.2.1 or 7.6.3 (Bitplane), and Fiji. CAR-mEmerald microcluster tracking analysis was performed using the spots function in Imaris with the following parameters: 0.25 µm estimated diameter, autoregressive motion tracking, 0.5 µm maximum distance, gap size 3, track duration > 5 sec. Centroid positions for dot product calculations were defined by making a surface of the synapse CAR-mEmerald interface in Imaris with grain size of 3 µm and largest sphere diameter of 1 µm. Analysis for LLS was performed in Imaris and Matlab. Unique analysis code has been made available through GitHub and can be found at the URLs included below.

Lattice Light-Sheet: post processing

Raw data were deconvolved using the iterative Richardson-Lucy deconvolution process with a known point spread function that was recorded for each color prior to the experiment, as described previously[188]. A typical sample area underwent 15-20 iterations of deconvolution. For live imaging experiments, photobleaching correction was applied in FIJI using the histogram matching method.

Close contact segmentation and persistence analysis

Close contact segmentation, CAR co-localization, and persistence time analysis was performed using Matlab and Imaris as previously described[188]. Briefly, the IRM images were used to define the region of the cell interface. Active contour segmentation of the QD605 image was then used to define close contact regions. These regions were then converted to Spots objects in Imaris. CAR intensity was masked to regions of close contacts, and the average intensity for each contact area was then plotted in a histogram. A Gaussian distribution curve centered at the background fluorescence median was overlayed. Contacts that fell within 3 sigma of the Gaussian distribution were considered CAR$^-$, while the higher intensity contacts were considered CAR$^+$. These contacts were then separated into separate image stacks and persistence time for individual contacts were calculated. Contact persistence time was determined by summing the number of frames each binary connected component object existed for and multiplying by the time per frame. Contacts were assumed to not travel more than their diameter per time point. Code for analysis of persistence times has been made available: https://github.com/BIDCatUCSF/NanocontactsTIRF_V5.

Radial intensity profiles

Definition of cell boundary, assignment of radial coordinates, and plotting of pixel intensities were performed using MatLab (Natick, MA). The outer edge (boundary) of cells was detected using a custom program which primarily applied a two-step kmeans clustering calculation on each of the image slices collected in the z-stack of images describing a single cell. The boundary was then eroded by three pixels to accommodate the resolution of the LLS imaging system. Code for defining the cell boundary: https://github.com/BIDCatUCSF/Exterior-t-Cell-Edge-Detection. Radial coordinates were assigned for plotting of radial intensity profiles using this code: https://github.com/BIDCatUCSF/Outer-Boundary-Profile-Code. Binned intensity was measured by taking a moving average of ten pixels. Excursions of the binned intensity above the channel mean intensity + 3 s.d. were used as the threshold to define patches.

Three-dimensional surface curvature mapping and patch analysis

The surface curvature and patch analysis used here was performed in MatLab as described in Cai et al. 2022[76]. Briefly, the cell boundaries (as defined above for radial intensity profiles) were used to calculate Pearson's correlation coefficients for variable sized kernels in three dimensions, roughly of the shape of the point spread function. These correlation coefficients were then used as the basis for clustering analysis by segmentation and watershed, creating the patches. Surface curvature was calculated for each position of the cell boundary, mapped by color, and thresholded to regions of low curvature to indicate peaks on the cell surface. Projections of the surface curvature and receptor intensity onto two dimensions were created using Map3-2D software[215].

Fura-2 ratio image analysis

Fura-2 340nm/380nm ratio images were created in MetaMorph Version 7.6.5.0 using a maximum ratio of 7 and imported to Imaris for tracking using the surface function with the following parameters: 1 μm grain size, 0.75 μm diameter of largest sphere, 2 μm region growing estimated diameter autoregressive motion tracking, 2 μm maximum distance, gap size 1, track duration above 148 sec. For analysis of final time point, surfaces were made for all cells in field of view without tracking: 0.75 μm grain size, 0.75 μm diameter of largest sphere, 1.5 μm region growing estimated diameter. Maximum 340nm/380nm ratio per cell was compared for all cells in field of view at final imaging time point – 5.5 min after addition of T cells to chamber well.

Statistics

Statistical tests were performed using GraphPad Prism Version 9.0.1. Independent experiments and donors are as noted in figure legends – all other replicates are technical replicates. Significance tests are as described in legends and include: Tukey's multiple comparisons tests, Šídák's multiple comparisons tests, and two-tailed t tests. Scatter plots show mean and s.d (error bars). Box and whisker plots indicate median, 25th to 75th percentile (box), and minimum to maximum (whiskers). P values are reported as follows: ≥ 0.05 as ns, 0.01 to 0.05 as *, 0.001 to 0.01 as **, 0.0001 to 0.001 as ***, and < 0.0001 as ****.

Chapter 4 – Conclusion

This thesis work reveals the topological scanning mechanism used by T cells to search for cognate antigen on the surface of APCs. We show that T cell microvilli are highly dynamic structures that achieve near complete scanning of APCs within in vivo T-APC contact times (**Fig. 2.1**). The formation of microvilli is constitutive, but upon ligand detection TCR-occupied microvilli are specifically stabilized in a manner dependent on the presence of cognate antigen but independent of the actin cytoskeleton and ZAP70 catalytic function[216] (**Fig. 2.9, 2.13, 2.15**). Within these studies, we focused on the IS formed by CD8+ cytotoxic T cells. CD4+ helper T cells, which take on similar IS organizations[61] and also have TCR-occupied microvilli[75], have been studied since then by others and also use microvilli during synaptic antigen scanning[217].

Microvillar scanning and stabilization is not only used in natural ligand detection, but also by engineered CAR T cells. We show that the distribution of a model anti-HER2 CAR relative to microvilli is similar to that of the natural TCR before and after ligand binding (**Fig. 3.1-6**). However, following antigen binding, conventional CARs yield super-physiological stabilization of the underlying microvilli, which is dependent on the receptor's affinity and avidity (**Fig. 3.7**). Of note, this is associated with a multifocal synapse organization, reduced effector function, and increased propensity for exhaustion (**Fig. 3.9**). These findings add to previous work demonstrating the importance of microvillar localization of surface proteins for sensitivity in other leukocyte functions[69,74].

Finding the optimal balance between robust effector function and exhaustion is one of the current challenges in the CAR T cell field. Our work suggests that binding dynamics may be a key feature of CAR design which could modulate this axis. The dimeric lower affinity CAR tested here reduced TOX expression, a known regulator of commitment to exhaustion[218,219], under

hypoxia with continuous stimulation (**Fig. 3.9I**). This is in line with recent work by Shakiba et al., which found that high affinity TCR led to increased propensity for exhaustion[196]. Exhaustion of CAR T cells caused by substantial tonic signaling has been identified as a barrier to successful outcomes and various methods have been designed to minimize these effects[125,220–223]. Compared to those studies, we did not observe substantial exhaustion generated in the absence of antigen stimulation in vitro, which is likely due to minimal multimerization of the CARs tested here – LLS imaging of CARs shows patches of locally high intensity similar to that of the natural TCR (**Fig. 3.1-4**) – but may also be aided by our use of 4-1BB co-stimulation which is thought to be less prone to promoting exhaustion[125].

Desirable outcomes have been ascribed previously to the use of lower affinity CARs. For example, a very low affinity scFv (4D5-3, K_D = 3,910 nM) CAR improved antigen density discrimination[137]. This is an important quality given the desire to minimize toxicities resulting from on-target, off-tumor binding. Of note, the lower affinity scFv tested here (K_D = 3.6 nM) is of much greater affinity than 4D5-3, and the dimeric CAR using this scFv still demonstrates poor antigen density discrimination. While the monomer somewhat improved discrimination, this comes at the cost of reduced effector responses (**Fig. 3.9**). Our work goes beyond those previous studies, linking the affinity effects to a normalization of cell biology, notably the dynamics of membrane-membrane engagements at microvilli.

Previous work by Davenport et al. established the existence of altered CAR T cell synapse structures defined by a multifocal distribution of Lck microclusters, which were associated with more rapid response times relative to those mediated by native TCR[143]. Our work expands on this by showing that an anti-HER2 CAR drives microclusters to form at microvillar contacts but generates hyper-stability of the underlying protrusion (**Fig. 3.7**). Additionally, by variation of affinity and multimerization status of a CAR we show that binding dynamics, and possibly the

115

intracellular multimerization state, are a key regulator of CAR microcluster mobility and synapse structure, with high-affinity/avidity interactions leading to altered IS organization. These interactions are also associated with reductions in T cell quality – scFvs with ~70-fold reduced K_D maintained or enhanced effector function and improved resistance to exhaustion.

In summary, this thesis work, alongside other recent studies[189–192,217], establishes the importance of dynamic microvilli in the T cell's antigen search process. Critically, we show that these dynamics are sufficient for near-complete scanning of surfaces in physiologically relevant timescales. Thus, microvilli enable the T cell to efficiently probe topologically complex surfaces. Furthermore, our finding that microvilli become stabilized specifically upon receptor antigen binding provides the mechanism by which a stable membrane surface is established for recruitment of adaptor proteins and initiation of signal transduction. Using synthetic receptors with supraphysiological binding affinities, we furthermore show that the dynamics of synaptic microvilli are directly related to the affinity and avidity of receptor binding – a critical component of the T cell's ability to appropriately respond to antigen throughout developmental and effector stages. Thus, the cell biological process underlying T cell ligand detection is finely tuned to respond to antigen receptor interactions with cognate antigen.

Future Directions

This body of work opens up important new avenues for future study, both relating to natural T cell biology and for improving clinical outcomes of T cell therapies. Our study of topological scanning dynamics focused entirely on the T cell surface. Future work is warranted to determine the contributions of various APC types to microvillar dynamics at the IS interface. In a study by Leithner et al., dendritic cell actin dynamics were shown to alter the organization of TCRs at the synapse[210]. Such work highlights the active part that some APCs play in antigen scanning, but more studies in this area are needed.

Given that so little is known about the biology of T cell microvilli, there is ample room for future studies of the factors that regulate their formation and movement, as well as the mechanisms by which molecules localize to regions of variable surface curvature. We show here that microvillar dynamics are stabilized by antigen receptor binding and further modulated by affinity and avidity, but stability after binding was independent of actin polymerization and ZAP70 catalytic function[216]. Microvilli form in the absence of any Src-family kinase activity[188], but it is possible that Lck and/or Fyn could be involved in stabilization through other as of yet unknown mechanisms. Future experiments will be needed in order to determine if the adaptor function of ZAP70 is required for stabilization of microvilli. Additionally, although not apparent by the imaging methods used here, recent evidence obtained by expansion microscopy[224] suggests that CD45 is excluded from microvilli tips even prior to antigen binding[217]. This is an intriguing mechanism that would increase a T cell's sensitivity to cognate pMHC, and future studies to establish if, when, and how this affects T cell antigen scanning will be enlightening. Additionally, we do not know what the effects of forcing TCRs to reside specifically in microvilli, more like L-selectin[69], would be for T cell topological antigen scanning and ligand detection.

In this work, avidity of binding was modulated by monomerizing the CAR (as well as by reducing the density of antigen). While monomerizing the CAR decreases its avidity, it also results in a loss of paired intracellular CD3ζ signaling domains, which may contribute to the decreased effector functions observed downstream of monomer binding. Future studies which dissect the contributions of binding as a monomer vs. signaling as a monomer will improve our understanding of CAR T cell triggering. For clinical optimization, future work will be needed to determine whether boosting the intracellular signal downstream of monomeric binding dynamics would yield a balance of both precise antigen density discrimination and robust signaling. It is possible that lowering the avidity of binding whilst radically boosting signal transduction may be key to producing robust, high quality T cells for cancer therapy.

Here we find conventional CAR to be superoptimal in experiments measuring proliferation and IFN-γ in human CAR T cells. However, we have studied only two scFvs, both of which have higher affinities for their ligands compared to typical TCRs. Future work will be needed to determine if the same mechanisms are at play in enforcing upper limits on CAR and TCR binding dynamics. In general, we expect the optimal scFv binding affinity to be greater than that of a TCR, based on the demonstration that CAR intracellular signaling domains are relatively inefficient[148] and that in some cases, higher affinity CARs can lead to increased potency[225]. Optimal binding dynamics will likely vary based on other aspects of CAR design and choice of signaling domains, but our evidence indicates that this optimization step is a critical component of high-quality T cell engineering. This work also highlights another aspect of CAR design which might be optimized for improved signaling output – the localization of the CAR. Here, we find that CARs do not obligately co-localize with TCRs (**Fig. 3.1-4**). By adjusting features of the transmembrane and intracellular domains, the synthetic receptor might be optimized to better co-localize with TCRs which could improve the recruitment of T cell signaling adapters.

Distinct synapse architectures have been reported as being associated with different cell types and signaling strength, as well as variable downstream outcomes[61]. Whether similar mechanisms are at play in multifocal TCR and CAR synapses is unknown. While this work demonstrates that CAR binding dynamics alter synapse architecture and T cell quality, this work does not show whether differences in synapse organization are causal to changes in effector function and exhaustion. Future work is warranted to determine whether altering CAR IS organization to more closely match the natural cell biology would improve T cell quality. For future CAR engineering, synapse dynamics could be an early predictor of ultimate T cell quality.

REFERENCES

(1)   Grakoui, A.; Bromley, S. K.; Sumen, C.; Davis, M. M.; Shaw, A. S.; Allen, P. M.; Dustin, M. L. The Immunological Synapse : A Molecular Machine Controlling T Cell Activation. **1999**, *221* (1999). https://doi.org/10.1126/science.285.5425.221.

(2)   Dustin, M. L.; Cooper, J. a. The Immunological Synapse and the Actin Cytoskeleton: Molecular Hardware for T Cell Signaling. *Nat. Immunol.* **2000**, *1* (1), 23–29. https://doi.org/10.1038/76877.

(3)   Krummel, M. F.; Davis, M. M. Dynamics of the Immunological Synapse: Finding, Establishing and Solidifying a Connection. *Curr. Opin. Immunol.* **2002**, *14* (1), 66–74. https://doi.org/10.1016/S0952-7915(01)00299-0.

(4)   Germain, R. N. MHC-Dependent Antigen Processing and Peptide Presentation: Providing Ligands for T Lymphocyte Activation. *Cell* **1994**, *76* (2), 287–299. https://doi.org/10.1016/0092-8674(94)90336-0.

(5)   Bjorkman, P. J.; Saper, M. A.; Samraoui, B.; Bennett, W. S.; Strominger, J. L.; Wiley, D. C. Structure of the Human Class I Histocompatibility Antigen, HLA-A2. *Nature* **1987**, *329* (6139), 506–512. https://doi.org/10.1038/329506a0.

(6)   Rabinowitz, J. D.; Beeson, C.; Wülfing, C.; Tate, K.; Allen, P. M.; Davis, M. M.; McConnell, H. M. Altered T Cell Receptor Ligands Trigger a Subset of Early T Cell Signals. *Immunity* **1996**, *5* (2), 125–135. https://doi.org/10.1016/S1074-7613(00)80489-6.

(7)   Wu, L. C.; Tuot, D. S.; Lyons, D. S.; Garcia, K. C.; Davis, M. M. Two-Step Binding Mechanism for T-Cell Receptor Recognition of Peptide MHC. *Nature* **2002**, *418* (6897), 552–556. https://doi.org/10.1038/nature00920.

(8)   Borg, N. A.; Ely, L. K.; Beddoe, T.; Macdonald, W. A.; Reid, H. H.; Clements, C. S.; Purcell, A. W.; Kjer-Nielsen, L.; Miles, J. J.; Burrows, S. R.; McCluskey, J.; Rossjohn, J. The CDR3 Regions of an Immunodominant T Cell Receptor Dictate the "energetic Landscape" of Peptide-MHC Recognition. *Nat. Immunol.* **2005**, *6* (2), 171–180. https://doi.org/10.1038/ni1155.

(9)   Falk, K.; Rötzschke, O.; Stevanovié, S.; Jung, G.; Rammensee, H.-G. Allele-Specific Motifs Revealed by Sequencing of Self-Peptides Eluted from MHC Molecules. *Nature* **1991**, *351* (6324), 290–296. https://doi.org/10.1038/351290a0.

(10)   Hunt, D. F.; Hanspeter, M.; A., D. T.; Jeffrey, S.; L., C. A.; Kazuyasu, S.; Ettore, A.; M., G. H.; Alessandro, S. Peptides Presented to the Immune System by the Murine Class II Major Histocompatibility Complex Molecule I-Ad. *Science (80-.).* **1992**, *256* (5065), 1817–1820. https://doi.org/10.1126/science.1319610.

(11)   Hunt, D. F.; A., H. R.; Jeffrey, S.; Kazuyasu, S.; Hanspeter, M.; Noelle, S.; L., C. A.; Ettore, A.; H., E. V. Characterization of Peptides Bound to the Class I MHC Molecule HLA-A2.1 by Mass Spectrometry. *Science (80-.).* **1992**, *255* (5049), 1261–1263. https://doi.org/10.1126/science.1546328.

(12)   de Jong, A. Contribution of Mass Spectrometry to Contemporary Immunology. *Mass Spectrom. Rev.* **1998**, *17* (5), 311–335. https://doi.org/https://doi.org/10.1002/(SICI)1098-2787(1998)17:5<311::AID-MAS1>3.0.CO;2-E.

(13)   Gérard, A.; Patino-Lopez, G.; Beemiller, P.; Nambiar, R.; Ben-Aissa, K.; Liu, Y.; Totah, F. J.; Tyska, M. J.; Shaw, S.; Krummel, M. F. Detection of Rare Antigen-Presenting Cells through T Cell-Intrinsic Meandering Motility, Mediated by

Myo1g. *Cell* **2014**, *158* (3), 492–505. https://doi.org/10.1016/j.cell.2014.05.044.

(14) Springer, T. A. Adhesion Receptors of the Immune System. *Nature* **1990**, *346*, 425–434. https://doi.org/10.1038/346425a0.

(15) Bell, G. I.; Dembo, M.; Bongrand, P. Cell Adhesion. Competition between Nonspecific Repulsion and Specific Bonding. *Biophys. J.* **1984**, *45* (6), 1051–1064. https://doi.org/10.1016/S0006-3495(84)84252-6.

(16) Möckl, L. The Emerging Role of the Mammalian Glycocalyx in Functional Membrane Organization and Immune System Regulation . *Frontiers in Cell and Developmental Biology* . 2020.

(17) Lyons, D. S.; Lieberman, S. A.; Hampl, J.; Boniface, J. J.; Reay, P. A.; Chien, Y.-H.; Berg, L. J.; Davis, M. M. T Cell Receptor Binding to Antagonist Peptide/MHC Complexes Exhibits Lower Affinities and Faster Dissociation Rates than to Agonist Ligands. **1996**, *5*, 53–61.

(18) Alam, S. M.; Travers, P. J.; Wung, J. L.; Nasholds, W.; Redpath, S.; Jameson, S. C.; Gascoigne, N. R. J. T-Cell-Receptor Affinity and Thymocyte Positive Selection. *Nature.* 1996, pp 616–620. https://doi.org/10.1038/381616a0.

(19) Davis, M. M.; Boniface, J. J.; Reich, Z.; Lyons, D.; Hampl, J.; Arden, B.; Chien, Y. Ligand Recognition By Aβ T Cell Receptors. **1998**.

(20) Matsui, K.; Boniface, J. J.; Reay, P. A.; Schild, H.; Fazekas de St Groth, B.; Davis, M. M. Low Affinity Interaction of Peptide-MHC Complexes with T Cell Receptors. *Science* **1991**, *254* (5039), 1788–1791. https://doi.org/10.1126/science.1763329.

(21) Tsourkas, P. K.; Liu, W.; Das, S. C.; Pierce, S. K.; Raychaudhuri, S. Discrimination of Membrane Antigen Affinity by B Cells Requires Dominance of

Kinetic Proofreading over Serial Engagement. *Cell. Mol. Immunol.* **2012**, *9* (1),
62–74. https://doi.org/10.1038/cmi.2011.29.

(22) Batista, F. D.; Neuberger, M. S. Affinity Dependence of the B Cell Response to
Antigen: A Threshold, a Ceiling, and the Importance of off-Rate. *Immunity* **1998**,
8 (6), 751–759. https://doi.org/10.1016/s1074-7613(00)80580-4.

(23) Carrasco, Y. R.; Fleire, S. J.; Cameron, T.; Dustin, M. L.; Batista, F. D. LFA-
1/ICAM-1 Interaction Lowers the Threshold of B Cell Activation by Facilitating B
Cell Adhesion and Synapse Formation. *Immunity* **2004**, *20* (5), 589–599.
https://doi.org/10.1016/s1074-7613(04)00105-0.

(24) Karjalainen, K. High Sensitivity, Low Affinity--Paradox of T-Cell Receptor
Recognition. *Curr. Opin. Immunol.* **1994**, *6* (1), 9–12.
https://doi.org/10.1016/0952-7915(94)90027-2.

(25) Sykulev, Y.; Joo, M.; Vturina, I.; Tsomides, T. J.; Eisen, H. N. Evidence That a
Single Peptide-MHC Complex on a Target Cell Can Elicit a Cytolytic T Cell
Response. *Immunity* **1996**, *4* (6), 565–571. https://doi.org/10.1016/S1074-
7613(00)80483-5.

(26) Schamel, W. W. A.; Arechaga, I.; Risueño, R. M.; van Santen, H. M.; Cabezas,
P.; Risco, C.; Valpuesta, J. M.; Alarcón, B. Coexistence of Multivalent and
Monovalent TCRs Explains High Sensitivity and Wide Range of Response. *J.
Exp. Med.* **2005**, *202* (4), 493–503. https://doi.org/10.1084/jem.20042155.

(27) Huang, J.; Brameshuber, M.; Zeng, X.; Xie, J.; Li, Q. jing; Chien, Y. hsiu; Valitutti,
S.; Davis, M. M. A Single Peptide-Major Histocompatibility Complex Ligand
Triggers Digital Cytokine Secretion in CD4+ T Cells. *Immunity* **2013**, *39* (5), 846–

857. https://doi.org/10.1016/j.immuni.2013.08.036.

(28)   Kersh, G. J.; Kersh, E. N.; Fremont, D. H.; Allen, P. M. High- and Low-Potency Ligands with Similar Affinities for the TCR: The Importance of Kinetic in TCR Signaling. *Immunity* **1998**, *9* (6), 817–826. https://doi.org/10.1016/S1074-7613(00)80647-0.

(29)   Kumar, R.; Ferez, M.; Swamy, M.; Arechaga, I.; Rejas, M. T.; Valpuesta, J. M.; Schamel, W. W. A.; Alarcon, B.; van Santen, H. M. Increased Sensitivity of Antigen-Experienced T Cells through the Enrichment of Oligomeric T Cell Receptor Complexes. *Immunity* **2011**, *35* (3), 375–387. https://doi.org/10.1016/j.immuni.2011.08.010.

(30)   Zhong, L.; Zeng, G.; Lu, X.; Wang, R. C.; Gong, G.; Yan, L.; Huang, D.; Chen, Z. W. NSOM/QD-Based Direct Visualization of CD3-Induced and CD28-Enhanced Nanospatial Coclustering of TCR and Coreceptor in Nanodomains in T Cell Activation. *PLoS One* **2009**, *4* (6). https://doi.org/10.1371/journal.pone.0005945.

(31)   Borger, J. G.; Zamoyska, R.; Gakamsky, D. M. Proximity of TCR and Its CD8 Coreceptor Controls Sensitivity of T Cells. *Immunol. Lett.* **2014**, *157* (1–2), 16–22. https://doi.org/10.1016/j.imlet.2013.11.005.

(32)   Fahmy, T. M.; Bieler, J. G.; Edidin, M.; Schneck, J. P. Increased TCR Avidity after T Cell Activation A Mechanism for Sensing Low-Density Antigen. *Immunity* **2001**, *14* (2), 135–143. https://doi.org/10.1016/S1074-7613(09)00099-5.

(33)   Bunnell, S. C.; Hong, D. I.; Kardon, J. R.; Yamazaki, T.; McGlade, C. J.; Barr, V. A.; Samelson, L. E. T Cell Receptor Ligation Induces the Formation of Dynamically Regulated Signaling Assemblies. *J. Cell Biol.* **2002**, *158* (7), 1263–

1275. https://doi.org/10.1083/jcb.200203043.

(34) Kuhns, M. S.; Girvin, A. T.; Klein, L. O.; Chen, R.; Jensen, K. D. C.; Newell, E. W.; Huppa, J. B.; Lillemeier, B. F.; Huse, M.; Chien, Y.-H.; Garcia, K. C.; Davis, M. M. Evidence for a Functional Sidedness to the AlphabetaTCR. *Proc. Natl. Acad. Sci. U. S. A.* **2010**, *107* (11), 5094–5099. https://doi.org/10.1073/pnas.1000925107.

(35) Gil, D.; Schamel, W. W. A.; Montoya, M.; Sánchez-Madrid, F.; Alarcón, B. Recruitment of Nck by CD3-Epsilon Reveals a Ligand-Induced Conformational Change Essential for T Cell Receptor Signaling and Synapse Formation. *Cell* **2002**, *109* (7), 901–912. https://doi.org/10.1016/S0092-8674(02)00799-7.

(36) Gil, D.; Schrum, A. G.; Alarcón, B.; Palmer, E. T Cell Receptor Engagement by Peptide-MHC Ligands Induces a Conformational Change in the CD3 Complex of Thymocytes. *J. Exp. Med.* **2005**, *201* (4), 517–522. https://doi.org/10.1084/jem.20042036.

(37) Beddoe, T.; Chen, Z.; Clements, C. S.; Ely, L. K.; Bushell, S. R.; Vivian, J. P.; Kjer-Nielsen, L.; Pang, S. S.; Dunstone, M. A.; Liu, Y. C.; Macdonald, W. A.; Perugini, M. A.; Wilce, M. C. J.; Burrows, S. R.; Purcell, A. W.; Tiganis, T.; Bottomley, S. P.; McCluskey, J.; Rossjohn, J. Antigen Ligation Triggers a Conformational Change within the Constant Domain of the ???? T Cell Receptor. *Immunity* **2009**, *30* (6), 777–788. https://doi.org/10.1016/j.immuni.2009.03.018.

(38) Martínez-Martín, N.; Risueño, R. M.; Morreale, A.; Zaldívar, I.; Fernández-Arenas, E.; Herranz, F.; Ortiz, A. R.; Alarcón, B. Cooperativity between T Cell Receptor Complexes Revealed by Conformational Mutants of CD3epsilon. *Sci. Signal.* **2009**, *2* (83), ra43. https://doi.org/10.1126/scisignal.2000402.

(39) Choudhuri, K.; Kearney, A.; Bakker, T. R.; van der Merwe, P. A. Immunology: How Do T Cells Recognize Antigen? *Curr. Biol.* **2005**, *15* (10). https://doi.org/10.1016/j.cub.2005.05.001.

(40) Su, X.; Ditlev, J. A.; Hui, E.; Xing, W.; Banjade, S.; Okrut, J.; King, D. S.; Tauton, J.; Rosen, M. K.; Vale, R. D. Phase Separation of Signaling Molecules Promotes T Cell Receptor Signal Transduction. *Science* **2016**, *352* (6285), 595–599. https://doi.org/10.1017/CBO9781107415324.004.

(41) McKeithan, T. W. Kinetic Proofreading in T-Cell Receptor Signal Transduction. *Proc. Natl. Acad. Sci.* **1995**, *92* (May), 5042–5046. https://doi.org/10.1073/pnas.92.11.5042.

(42) Davis, S. J.; Van Der Merwe, P. A. The Structure and Ligand Interactions of CD2: Implications for T-Cell Function. *Immunol. Today* **1996**, *17* (4), 177–187. https://doi.org/10.1016/0167-5699(96)80617-7.

(43) van der Merwe, P. A.; Davis, S. J.; Shaw, A. S.; Dustin, M. L. Cytoskeletal Polarization and Redistribution of Cell-Surface Molecules during T Cell Antigen Recognition. *Semin. Immunol.* **2000**, *12* (1), 5–21. https://doi.org/10.1006/smim.2000.0203.

(44) Davis, S. J.; van der Merwe, P. A. The Kinetic-Segregation Model: TCR Triggering and Beyond. *Nat. Immunol.* **2006**, *7* (8), 803–809. https://doi.org/10.1038/ni1369.

(45) Chang, V. T.; Fernandes, R. A.; Ganzinger, K. A.; Lee, S. F.; Siebold, C.; McColl, J.; Jönsson, P.; Palayret, M.; Harlos, K.; Coles, C. H.; Jones, E. Y.; Lui, Y.; Huang, E.; Gilbert, R. J. C.; Klenerman, D.; Aricescu, A. R.; Davis, S. J. Initiation

of T Cell Signaling by CD45 Segregation at "Close Contacts." *Nat. Immunol.*
2016, *17* (5), 574–582. https://doi.org/10.1038/ni.3392.

(46)   Groves, J. T.; Dustin, M. L. Supported Planar Bilayers in Studies on Immune Cell
Adhesion and Communication. *J. Immunol. Methods* **2003**, *278* (1), 19–32.
https://doi.org/https://doi.org/10.1016/S0022-1759(03)00193-5.

(47)   Dustin, M. L.; Olszowy, M. W.; Holdorf, A. D.; Li, J.; Bromley, S.; Desai, N.;
Widder, P.; Rosenberger, F.; van der Merwe, P. A.; Allen, P. M.; Shaw, A. S. A
Novel Adaptor Protein Orchestrates Receptor Patterning and Cytoskeletal Polarity
in T-Cell Contacts. *Cell* **1998**, *94* (5), 667–677. https://doi.org/10.1016/S0092-
8674(00)81608-6.

(48)   Dustin, M. L.; Miller, J. M.; Ranganath, S.; Vignali, D. A.; Viner, N. J.; Nelson, C.
A.; Unanue, E. R. TCR-Mediated Adhesion of T Cell Hybridomas to Planar
Bilayers Containing Purified MHC Class II/Peptide Complexes and Receptor
Shedding during Detachment. *J. Immunol.* **1996**, *157* (5), 2014–2021.

(49)   Wülfing, C.; Sjaastad, M. D.; Davis, M. M. Visualizing the Dynamics of T Cell
Activation: Intracellular Adhesion Molecule 1 Migrates Rapidly to the T Cell/B Cell
Interface and Acts to Sustain Calcium Levels. *Proc. Natl. Acad. Sci. U. S. A.*
1998, *95* (11), 6302–6307. https://doi.org/10.1073/pnas.95.11.6302.

(50)   Beemiller, P.; Jacobelli, J.; Krummel, M. F. Integration of the Movement of
Signaling Microclusters with Cellular Motility in Immunological Synapses. *Nat.
Immunol.* **2012**, *13* (8), 787–795. https://doi.org/10.1038/ni.2364.

(51)   Campi, G.; Varma, R.; Dustin, M. L. Actin and Agonist MHC-Peptide Complex-
Dependent T Cell Receptor Microclusters as Scaffolds for Signaling. *J. Exp. Med.*

2005, *202* (8), 1031–1036. https://doi.org/10.1084/jem.20051182.

(52) Yokosuka, T.; Sakata-Sogawa, K.; Kobayashi, W.; Hiroshima, M.; Hashimoto-Tane, A.; Tokunaga, M.; Dustin, M. L.; Saito, T. Newly Generated T Cell Receptor Microclusters Initiate and Sustain T Cell Activation by Recruitment of Zap70 and SLP-76. *Nat. Immunol.* **2005**, *6* (12), 1253–1262. https://doi.org/10.1038/ni1272.

(53) Varma, R.; Campi, G.; Yokosuka, T.; Saito, T.; Dustin, M. L. T Cell Receptor-Proximal Signals Are Sustained in Peripheral Microclusters and Terminated in the Central Supramolecular Activation Cluster. *Immunity* **2006**, *25* (1), 117–127. https://doi.org/10.1016/j.immuni.2006.04.010.

(54) Lillemeier, B. F.; Mörtelmaier, M. A.; Forstner, M. B.; Huppa, J. B.; Groves, J. T.; Davis, M. M. TCR and Lat Are Expressed on Separate Protein Islands on T Cell Membranes and Concatenate during Activation. *Nat. Immunol.* **2010**, *11* (1), 90–96. https://doi.org/10.1038/ni0610-543b.

(55) Monks, C. R.; Freiberg, B. a; Kupfer, H.; Sciaky, N.; Kupfer, a. Three-Dimensional Segregation of Supramolecular Activation Clusters in T Cells. *Nature* **1998**, *395* (6697), 82–86. https://doi.org/10.1038/25764.

(56) Krummel, M. F.; Sjaastad, M. D.; Wülfing, C.; Davis, M. M. Differential Clustering of CD4 and CD3ζ during T Cell Recognition. *Science (80-.).* **2000**, *289* (August), 1349–1352. https://doi.org/10.1126/science.289.5483.1349.

(57) Lee, K.-H.; Holdorf, A. D.; Dustin, M. L.; Chan, A. C.; Allen, P. M.; Shaw, A. S. T Cell Receptor Signaling Precedes Immunological Synapse Formation. *Science* **2002**, *295* (5559), 1539–1542. https://doi.org/10.1126/science.1067710.

(58) Vardhana, S.; Choudhuri, K.; Varma, R.; Dustin, M. L. Essential Role of Ubiquitin

and TSG101 Protein in Formation and Function of the Central Supramolecular Activation Cluster. *Immunity* **2010**, *32* (4), 531–540. https://doi.org/10.1016/j.immuni.2010.04.005.

(59)   Martínez-Martín, N.; Fernández-Arenas, E.; Cemerski, S.; Delgado, P.; Turner, M.; Heuser, J.; Irvine, D. J.; Huang, B.; Bustelo, X. R.; Shaw, A.; Alarcón, B. T Cell Receptor Internalization from the Immunological Synapse Is Mediated by TC21 and RhoG GTPase-Dependent Phagocytosis. *Immunity* **2011**, *35* (2), 208– 222. https://doi.org/10.1016/j.immuni.2011.06.003.

(60)   Choudhuri, K.; Llodrá, J.; Roth, E. W.; Tsai, J.; Gordo, S.; Wucherpfennig, K. W.; Kam, L. C.; Stokes, D. L.; Dustin, M. L. Polarized Release of T-Cell-Receptor-Enriched Microvesicles at the Immunological Synapse. *Nature* **2014**, *507* (7490), 118–123. https://doi.org/10.1038/nature12951.

(61)   Friedl, P.; Den Boer, A. T.; Gunzer, M. Tuning Immune Responses: Diversity and Adaptation of the Immunological Synapse. *Nat. Rev. Immunol.* **2005**, *5* (7), 532– 545. https://doi.org/10.1038/nri1647.

(62)   Brossard, C.; Feuillet, V.; Schmitt, A.; Randriamampita, C.; Romao, M.; Raposo, G.; Trautmann, A. Multifocal Structure of the T Cell - Dendritic Cell Synapse. *Eur. J. Immunol.* **2005**, *35* (6), 1741–1753. https://doi.org/10.1002/eji.200425857.

(63)   Mempel, T. R.; Henrickson, S. E.; Von Andrian, U. H. T-Cell Priming by Dendritic Cells in Lymph Nodes Occurs in Three Distinct Phases. *Nature* **2004**, *427* (6970), 154–159. https://doi.org/10.1038/nature02238.

(64)   Miller, M. J.; Safrina, O.; Parker, I.; Cahalan, M. D. Imaging the Single Cell Dynamics of CD4+ T Cell Activation by Dendritic Cells in Lymph Nodes. *J. Exp.*

Med. **2004**, *200* (7), 847–856. https://doi.org/10.1084/jem.20041236.

(65) Friedman, R. S.; Beemiller, P.; Sorensen, C. M.; Jacobelli, J.; Krummel, M. F. Real-Time Analysis of T Cell Receptors in Naive Cells in Vitro and in Vivo Reveals Flexibility in Synapse and Signaling Dynamics. *J Exp Med* **2010**, *207* (12), 2733–2749. https://doi.org/10.1084/jem.20091201.

(66) Richie, L. I.; Ebert, P. J. R.; Wu, L. C.; Krummel, M. F.; Owen, J. J. T.; Davis, M. M. Imaging Synapse Formation during Thymocyte Selection: Inability of CD3ζ to Form a Stable Central Accumulation during Negative Selection. *Immunity* **2002**, *16* (4), 595–606. https://doi.org/10.1016/S1074-7613(02)00299-6.

(67) Palmer, E. Negative Selection — Clearing out the Bad Apples from the T-Cell Repertoire. *Nat. Rev. Immunol.* **2003**, *3* (5), 383–391. https://doi.org/10.1038/nri1085.

(68) Majstoravich, S.; Zhang, J.; Nicholson-Dykstra, S.; Linder, S.; Friedrich, W.; Siminovitch, K. A.; Higgs, H. N. Lymphocyte Microvilli Are Dynamic, Actin-Dependent Structures That Do Not Require Wiskott-Aldrich Syndrome Protein (WASp) for Their Morphology. *Blood* **2004**, *104* (5), 1396–1403. https://doi.org/10.1182/blood-2004-02-0437.

(69) von Andrian, U. H.; Hasslen, S. R.; Nelson, R. D.; Erlandsen, S. L.; Butcher, E. C. A Central Role for Microvillous Receptor Presentation in Leukocyte Adhesion under Flow. *Cell* **1995**, *82* (6), 989–999. https://doi.org/10.1016/0092-8674(95)90278-3.

(70) Stein, J. V.; Cheng, G.; Stockton, B. M.; Fors, B. P.; Butcher, E. C.; von Andrian, U. H. L-Selectin-Mediated Leukocyte Adhesion in Vivo: Microvillous Distribution

Determines Tethering Efficiency, but Not Rolling Velocity. *J. Exp. Med.* **1999**, *189* (1), 37–50. https://doi.org/10.1084/jem.189.1.37.

(71) Crawley, S. W.; Mooseker, M. S.; Tyska, M. J. Shaping the Intestinal Brush Border. *J. Cell Biol.* **2014**, *207* (4), 441–451. https://doi.org/10.1083/jcb.201407015.

(72) Meenderink, L. M.; Gaeta, I. M.; Postema, M. M.; Cencer, C. S.; Chinowsky, C. R.; Krystofiak, E. S.; Millis, B. A.; Tyska, M. J. Actin Dynamics Drive Microvillar Motility and Clustering during Brush Border Assembly. *Dev. Cell* **2019**, *50* (5), 545-556.e4. https://doi.org/10.1016/j.devcel.2019.07.008.

(73) Linthicum, D. S.; Sell, S.; Wagner, R. M.; Trefts, P. Scanning Immunoelectron Microscopy of Mouse B and T Cells. *Nature* **1974**, *252* (November 8), 173–175.

(74) Berlin, C.; Bargatze, R. F.; Campbell, J. J.; von Andrian, U. H.; Szabo, M. C.; Hasslen, S. R.; Nelson, R. D.; Berg, E. L.; Erlandsen, S. L.; Butcher, E. C. A4 Integrins Mediate Lymphocyte Attachment and Rolling Under Physiologic Flow. *Cell* **1995**, *80* (3), 413–422. https://doi.org/10.1016/0092-8674(95)90491-3.

(75) Jung, Y.; Riven, I.; Feigelson, S. W.; Kartvelishvily, E.; Tohya, K.; Miyasaka, M.; Alon, R.; Haran, G. Three-Dimensional Localization of T-Cell Receptors in Relation to Microvilli Using a Combination of Superresolution Microscopies. *Proc. Natl. Acad. Sci. U. S. A.* **2016**, *113* (40), E5916–E5924. https://doi.org/10.1073/pnas.1605399113.

(76) Cai, E.; Beppler, C.; Eichorst, J.; Marchuk, K.; Krummel, M. F. T Cells Use Distinct Topological and Membrane Receptor Scanning Strategies That Individually Coalesce during Receptor Recognition. *bioRxiv* **2022**,

2022.02.23.481517. https://doi.org/10.1101/2022.02.23.481517.

(77) Chen, B.-C.; Legant, W. R.; Wang, K.; Shao, L.; Milkie, D. E.; Davidson, M. W.; Janetopoulos, C.; Wu, X. S.; Hammer, J. A.; Liu, Z.; English, B. P.; Mimori-Kiyosue, Y.; Romero, D. P.; Ritter, A. T.; Lippincott-Schwartz, J.; Fritz-Laylin, L.; Mullins, R. D.; Mitchell, D. M.; Bembenek, J. N.; Reymann, A.-C.; Bohme, R.; Grill, S. W.; Wang, J. T.; Seydoux, G.; Tulu, U. S.; Kiehart, D. P.; Betzig, E. Lattice Light-Sheet Microscopy: Imaging Molecules to Embryos at High Spatiotemporal Resolution. *Science (80-.).* **2014**, *346* (6208), 1257998–1257998. https://doi.org/10.1126/science.1257998.

(78) City of Hope Medical Center; National Cancer Institute; California Institute for Regenerative Medicine. HER2-CAR T Cells in Treating Patients With Recurrent Brain or Leptomeningeal Metastases. NCT03696030. 2018.

(79) Tmunity Therapeutics. A Study of CART-TnMUC1 in Patients With TnMUC1-Positive Advanced Cancers. NCT04025216. 2019.

(80) City of Hope Medical Center; National Cancer Institute. Brain Tumor-Specific Immune Cells (IL13Ralpha2-CAR T Cells) for the Treatment of Leptomeningeal Glioblastoma, Ependymoma, or Medulloblastoma. NCT04661384. 2021.

(81) Adami, A.; Maher, J. An Overview of CAR T-Cell Clinical Trial Activity to 2021. *Immunother. Adv.* **2021**, *1* (1), ltab004. https://doi.org/10.1093/immadv/ltab004.

(82) Gong, Y.; Klein Wolterink, R. G. J.; Wang, J.; Bos, G. M. J.; Germeraad, W. T. V. Chimeric Antigen Receptor Natural Killer (CAR-NK) Cell Design and Engineering for Cancer Therapy. *J. Hematol. Oncol.* **2021**, *14* (1), 73. https://doi.org/10.1186/s13045-021-01083-5.

(83) Nkarta Inc. A Phase 1 Study of NKX019, a CD19 Chimeric Antigen Receptor Natural Killer (CAR NK) Cell Therapy, in Subjects With B-Cell Malignancies. NCT05020678. 2021.

(84) Sloas, C.; Gill, S.; Klichinsky, M. Engineered CAR-Macrophages as Adoptive Immunotherapies for Solid Tumors . *Frontiers in Immunology* . 2021.

(85) Carisma Therapeutics Inc. A Phase 1, First in Human Study of Adenovirally Transduced Autologous Macrophages Engineered to Contain an Anti-HER2 Chimeric Antigen Receptor in Subjects With HER2 Overexpressing Solid Tumors. NCT04817774. 2021. https://doi.org/NCT04817774.

(86) Zhang, Q.; Lu, W.; Liang, C.-L.; Chen, Y.; Liu, H.; Qiu, F.; Dai, Z. Chimeric Antigen Receptor (CAR) Treg: A Promising Approach to Inducing Immunological Tolerance . *Frontiers in Immunology* . 2018.

(87) Sangamo Therapeutics. Multicentre Open-Label Single Ascending Dose Dose-Ranging Phase I/IIa Study to Evaluate Safety and Tolerability of an Autologous Antigen-Specific Chimeric Antigen Receptor TRegulatory Cell Therapy in Living Donor Renal Transplant. NCT04817774. Recipients. 2021.

(88) Mu, W.; Carrillo, M. A.; Kitchen, S. G. Engineering CAR T Cells to Target the HIV Reservoir . *Frontiers in Cellular and Infection Microbiology* . 2020.

(89) Deeks, S. Safety and Anti-HIV Activity of Autologous CD4+ and CD8+ T Cells Transduced With a Lentiviral Vector Encoding Bi-Specific Anti-Gp120 CAR Molecules (LVgp120duoCAR-T) in Anti-Retroviral Drug-Treated HIV-1 Infection. NCT04648046. 2021.

(90) Watanabe, N.; Mo, F.; McKenna, M. K. Impact of Manufacturing Procedures on

CAR T Cell Functionality. *Front. Immunol.* **2022**, *13*, 876339.
https://doi.org/10.3389/fimmu.2022.876339.

(91) Kuwana, Y.; Asakura, Y.; Utsunomiya, N.; Nakanishi, M.; Arata, Y.; Itoh, S.;
Nagase, F.; Kurosawa, Y. Expression of Chimeric Receptor Composed of
Immunoglobulin-Derived V Regions and T-Cell Receptor-Derived C Regions.
Biochem. Biophys. Res. Commun. **1987**, *149* (3), 960–968.
https://doi.org/10.1016/0006-291x(87)90502-x.

(92) Gross, G.; Waks, T.; Eshhar, Z. Expression of Immunoglobulin-T-Cell Receptor
Chimeric Molecules as Functional Receptors with Antibody-Type Specificity.
Proc. Natl. Acad. Sci. U. S. A. **1989**, *86* (24), 10024–10028.
https://doi.org/10.1073/pnas.86.24.10024.

(93) Irving, B. A.; Weiss, A. The Cytoplasmic Domain of the T Cell Receptor Zeta
Chain Is Sufficient to Couple to Receptor-Associated Signal Transduction
Pathways. *Cell* **1991**, *64* (5), 891–901.

(94) Kahlon, K. S.; Brown, C.; Cooper, L. J. N.; Raubitschek, A.; Forman, S. J.;
Jensen, M. C. Specific Recognition and Killing of Glioblastoma Multiforme by
Interleukin 13-Zetakine Redirected Cytolytic T Cells. *Cancer Res.* **2004**, *64* (24),
9160–9166. https://doi.org/10.1158/0008-5472.CAN-04-0454.

(95) Barber, A.; Rynda, A.; Sentman, C. L. Chimeric NKG2D Expressing T Cells
Eliminate Immunosuppression and Activate Immunity within the Ovarian Tumor
Microenvironment. *J. Immunol.* **2009**, *183* (11), 6939 LP – 6947.
https://doi.org/10.4049/jimmunol.0902000.

(96) Park, S.; Shevlin, E.; Vedvyas, Y.; Zaman, M.; Park, S.; Hsu, Y.-M. S.; Min, I. M.;

Jin, M. M. Micromolar Affinity CAR T Cells to ICAM-1 Achieves Rapid Tumor Elimination While Avoiding Systemic Toxicity. *Sci. Rep.* **2017**, *7* (1), 14366. https://doi.org/10.1038/s41598-017-14749-3.

(97)   Joy, X. Y.; Michael, D.; Noor, J.; Jessica, I.; Tao, F.; Laura, K.; Noor, M.; Novalia, P.; Steffen, R.; O., H. R.; Hidde, P. Nanobody-Based CAR T Cells That Target the Tumor Microenvironment Inhibit the Growth of Solid Tumors in Immunocompetent Mice. *Proc. Natl. Acad. Sci.* **2019**, *116* (16), 7624–7631. https://doi.org/10.1073/pnas.1817147116.

(98)   Wang, D.; Starr, R.; Chang, W.-C.; Aguilar, B.; Alizadeh, D.; Wright, S. L.; Yang, X.; Brito, A.; Sarkissian, A.; Ostberg, J. R.; Li, L.; Shi, Y.; Gutova, M.; Aboody, K.; Badie, B.; Forman, S. J.; Barish, M. E.; Brown, C. E. Chlorotoxin-Directed CAR T Cells for Specific and Effective Targeting of Glioblastoma. *Sci. Transl. Med.* **2020**, *12* (533). https://doi.org/10.1126/scitranslmed.aaw2672.

(99)   Hammill, J. A.; VanSeggelen, H.; Helsen, C. W.; Denisova, G. F.; Evelegh, C.; Tantalo, D. G. M.; Bassett, J. D.; Bramson, J. L. Designed Ankyrin Repeat Proteins Are Effective Targeting Elements for Chimeric Antigen Receptors. *J. Immunother. Cancer* **2015**, *3* (1), 55. https://doi.org/10.1186/s40425-015-0099-4.

(100) Hennecke, S.; Cosson, P. Role of Transmembrane Domains in Assembly and Intracellular Transport of the CD8 Molecule. *J. Biol. Chem.* **1993**, *268* (35), 26607–26612.

(101) Lazar-Molnar, E.; Almo, S. C.; Nathenson, S. G. The Interchain Disulfide Linkage Is Not a Prerequisite but Enhances CD28 Costimulatory Function. *Cell. Immunol.* **2006**, *244* (2), 125–129.

https://doi.org/https://doi.org/10.1016/j.cellimm.2007.02.014.

(102) Liu, H.; May, K. Disulfide Bond Structures of IgG Molecules: Structural Variations, Chemical Modifications and Possible Impacts to Stability and Biological Function. *MAbs* **2012**, *4* (1), 17–23. https://doi.org/10.4161/mabs.4.1.18347.

(103) Alabanza, L.; Pegues, M.; Geldres, C.; Shi, V.; Wiltzius, J. J. W.; Sievers, S. A.; Yang, S.; Kochenderfer, J. N. Function of Novel Anti-CD19 Chimeric Antigen Receptors with Human Variable Regions Is Affected by Hinge and Transmembrane Domains. *Mol. Ther.* **2017**, *25* (11), 2452–2465. https://doi.org/10.1016/j.ymthe.2017.07.013.

(104) Finney, H. M.; Lawson, A. D.; Bebbington, C. R.; Weir, A. N. Chimeric Receptors Providing Both Primary and Costimulatory Signaling in T Cells from a Single Gene Product. *J. Immunol.* **1998**, *161* (6), 2791–2797.

(105) Krause, A.; Guo, H. F.; Latouche, J. B.; Tan, C.; Cheung, N. K.; Sadelain, M. Antigen-Dependent CD28 Signaling Selectively Enhances Survival and Proliferation in Genetically Modified Activated Human Primary T Lymphocytes. *J. Exp. Med.* **1998**, *188* (4), 619–626. https://doi.org/10.1084/jem.188.4.619.

(106) Imai, C.; Mihara, K.; Andreansky, M.; Nicholson, I. C.; Pui, C.-H.; Geiger, T. L.; Campana, D. Chimeric Receptors with 4-1BB Signaling Capacity Provoke Potent Cytotoxicity against Acute Lymphoblastic Leukemia. *Leukemia* **2004**, *18* (4), 676–684. https://doi.org/10.1038/sj.leu.2403302.

(107) Kalos, M.; June, C. H. Adoptive T Cell Transfer for Cancer Immunotherapy in the Era of Synthetic Biology. *Immunity* **2013**, *39* (1), 49–60. https://doi.org/10.1016/j.immuni.2013.07.002.

(108) Porter, D. L.; Levine, B. L.; Kalos, M.; Bagg, A.; June, C. H. Chimeric Antigen Receptor-Modified T Cells in Chronic Lymphoid Leukemia. *N. Engl. J. Med.* **2011**, *365* (8), 725–733. https://doi.org/10.1056/NEJMoa1103849.

(109) Kalos, M.; Levine, B. L.; Porter, D. L.; Katz, S.; Grupp, S. A.; Bagg, A.; June, C. H. T Cells with Chimeric Antigen Receptors Have Potent Antitumor Effects and Can Establish Memory in Patients with Advanced Leukemia. *Sci. Transl. Med.* **2011**, *3* (95), 1–13. https://doi.org/10.1126/scitranslmed.3002842.

(110) Brentjens, R. J.; Davila, M. L.; Riviere, I.; Park, J.; Wang, X.; Cowell, L. G.; Bartido, S.; Stefanski, J.; Taylor, C.; Olszewska, M.; Borquez-Ojeda, O.; Qu, J.; Wasielewska, T.; He, Q.; Bernal, Y.; Rijo, I. V.; Hedvat, C.; Kobos, R.; Curran, K.; Steinherz, P.; Jurcic, J.; Rosenblat, T.; Maslak, P.; Frattini, M.; Sadelain, M. CD19-Targeted T Cells Rapidly Induce Molecular Remissions in Adults with Chemotherapy-Refractory Acute Lymphoblastic Leukemia. *Sci. Transl. Med.* **2013**, *5* (177). https://doi.org/10.1126/scitranslmed.3005930.

(111) Maude, S. L.; Frey, N.; Shaw, P. A.; Aplenc, R.; Barrett, D. M.; Bunin, N. J.; Chew, A.; Gonzalez, V. E.; Zheng, Z.; Lacey, S. F.; Mahnke, Y. D.; Melenhorst, J. J.; Rheingold, S. R.; Shen, A.; Teachey, D. T.; Levine, B. L.; June, C. H.; Porter, D. L.; Grupp, S. A. Chimeric Antigen Receptor T Cells for Sustained Remissions in Leukemia. *New England Journal of Medicine.* 2014, pp 1507–1517. https://doi.org/10.1056/nejmoa1407222.

(112) Turtle, C. J.; Hanafi, L. A.; Berger, C.; Gooley, T. A.; Cherian, S.; Hudecek, M.; Sommermeyer, D.; Melville, K.; Pender, B.; Budiarto, T. M.; Robinson, E.; Steevens, N. N.; Chaney, C.; Soma, L.; Chen, X.; Yeung, C.; Wood, B.; Li, D.;

Cao, J.; Heimfeld, S.; Jensen, M. C.; Riddell, S. R.; Maloney, D. G. CD19 CAR-T Cells of Defined CD4+:CD8+ Composition in Adult B Cell ALL Patients. *J. Clin. Invest.* **2016**, *126* (6), 2123–2138. https://doi.org/10.1172/JCI85309.

(113) Maude, S. L.; Laetsch, T. W.; Buechner, J.; Rives, S.; Boyer, M.; Bittencourt, H.; Bader, P.; Verneris, M. R.; Stefanski, H. E.; Myers, G. D.; Qayed, M.; De Moerloose, B.; Hiramatsu, H.; Schlis, K.; Davis, K. L.; Martin, P. L.; Nemecek, E. R.; Yanik, G. A.; Peters, C.; Baruchel, A.; Boissel, N.; Mechinaud, F.; Balduzzi, A.; Krueger, J.; June, C. H.; Levine, B. L.; Wood, P.; Taran, T.; Leung, M.; Mueller, K. T.; Zhang, Y.; Sen, K.; Lebwohl, D.; Pulsipher, M. A.; Grupp, S. A. Tisagenlecleucel in Children and Young Adults with B-Cell Lymphoblastic Leukemia. *N. Engl. J. Med.* **2018**, *378* (5), 439–448. https://doi.org/10.1056/NEJMoa1709866.

(114) Park, J. H.; Rivière, I.; Gonen, M.; Wang, X.; Sénéchal, B.; Curran, K. J.; Sauter, C.; Wang, Y.; Santomasso, B.; Mead, E.; Roshal, M.; Maslak, P.; Davila, M.; Brentjens, R. J.; Sadelain, M. Long-Term Follow-up of CD19 CAR Therapy in Acute Lymphoblastic Leukemia. *N. Engl. J. Med.* **2018**, *378* (5), 449–459. https://doi.org/10.1056/NEJMoa1709919.

(115) Schuster, S. J.; Svoboda, J.; Chong, E. A.; Nasta, S. D.; Mato, A. R.; Anak, Ö.; Brogdon, J. L.; Pruteanu-Malinici, I.; Bhoj, V.; Landsburg, D.; Wasik, M.; Levine, B. L.; Lacey, S. F.; Melenhorst, J. J.; Porter, D. L.; June, C. H. Chimeric Antigen Receptor T Cells in Refractory B-Cell Lymphomas. *N. Engl. J. Med.* **2017**, *377* (26), 2545–2554. https://doi.org/10.1056/NEJMoa1708566.

(116) Neelapu, S. S.; Locke, F. L.; Bartlett, N. L.; Lekakis, L. J.; Miklos, D. B.; Jacobson,

C. A.; Braunschweig, I.; Oluwole, O. O.; Siddiqi, T.; Lin, Y.; Timmerman, J. M.; Stiff, P. J.; Friedberg, J. W.; Flinn, I. W.; Goy, A.; Hill, B. T.; Smith, M. R.; Deol, A.; Farooq, U.; McSweeney, P.; Munoz, J.; Avivi, I.; Castro, J. E.; Westin, J. R.; Chavez, J. C.; Ghobadi, A.; Komanduri, K. V; Levy, R.; Jacobsen, E. D.; Witzig, T. E.; Reagan, P.; Bot, A.; Rossi, J.; Navale, L.; Jiang, Y.; Aycock, J.; Elias, M.; Chang, D.; Wiezorek, J.; Go, W. Y. Axicabtagene Ciloleucel CAR T-Cell Therapy in Refractory Large B-Cell Lymphoma. *N. Engl. J. Med.* **2017**, *377* (26), 2531–2544. https://doi.org/10.1056/NEJMoa1707447.

(117) Munshi, N. C.; Anderson, L. D.; Shah, N.; Madduri, D.; Berdeja, J.; Lonial, S.; Raje, N.; Lin, Y.; Siegel, D.; Oriol, A.; Moreau, P.; Yakoub-Agha, I.; Delforge, M.; Cavo, M.; Einsele, H.; Goldschmidt, H.; Weisel, K.; Rambaldi, A.; Reece, D.; Petrocca, F.; Massaro, M.; Connarn, J. N.; Kaiser, S.; Patel, P.; Huang, L.; Campbell, T. B.; Hege, K.; San-Miguel, J. Idecabtagene Vicleucel in Relapsed and Refractory Multiple Myeloma. *N. Engl. J. Med.* **2021**, *384* (8), 705–716. https://doi.org/10.1056/NEJMoa2024850.

(118) Cohen, A. D.; Garfall, A. L.; Stadtmauer, E. A.; Melenhorst, J. J.; Lacey, S. F.; Lancaster, E.; Vogl, D. T.; Weiss, B. M.; Dengel, K.; Nelson, A.; Plesa, G.; Chen, F.; Davis, M. M.; Hwang, W.-T.; Young, R. M.; Brogdon, J. L.; Isaacs, R.; Pruteanu-Malinici, I.; Siegel, D. L.; Levine, B. L.; June, C. H.; Milone, M. C. B Cell Maturation Antigen–Specific CAR T Cells Are Clinically Active in Multiple Myeloma. *J. Clin. Invest.* **2019**, *129* (6), 2210–2221. https://doi.org/10.1172/JCI126397.

(119) Raje, N.; Berdeja, J.; Lin, Y.; Siegel, D.; Jagannath, S.; Madduri, D.; Liedtke, M.;

Rosenblatt, J.; Maus, M. V; Turka, A.; Lam, L.-P.; Morgan, R. A.; Friedman, K.; Massaro, M.; Wang, J.; Russotti, G.; Yang, Z.; Campbell, T.; Hege, K.; Petrocca, F.; Quigley, M. T.; Munshi, N.; Kochenderfer, J. N. Anti-BCMA CAR T-Cell Therapy Bb2121 in Relapsed or Refractory Multiple Myeloma. *N. Engl. J. Med.* **2019**, *380* (18), 1726–1737. https://doi.org/10.1056/NEJMoa1817226.

(120) Xu, X.; Sun, Q.; Liang, X.; Chen, Z.; Zhang, X.; Zhou, X.; Li, M.; Tu, H.; Liu, Y.; Tu, S.; Li, Y. Mechanisms of Relapse After CD19 CAR T-Cell Therapy for Acute Lymphoblastic Leukemia and Its Prevention and Treatment Strategies. *Front. Immunol.* **2019**, *10*, 2664. https://doi.org/10.3389/fimmu.2019.02664.

(121) Shah, N. N.; Maatman, T.; Hari, P.; Johnson, B. Multi Targeted CAR-T Cell Therapies for B-Cell Malignancies. *Front. Oncol.* **2019**, *9*, 146. https://doi.org/10.3389/fonc.2019.00146.

(122) Newick, K.; O'Brien, S.; Moon, E.; Albelda, S. M. CAR T Cell Therapy for Solid Tumors. *Annu. Rev. Med.* **2017**, *68*, 139–152. https://doi.org/10.1146/annurev-med-062315-120245.

(123) Majzner, R. G.; Mackall, C. L. Tumor Antigen Escape from CAR T-Cell Therapy. *Cancer Discov.* **2018**, *8* (10), 1219–1226. https://doi.org/10.1158/2159-8290.CD-18-0442.

(124) Labanieh, L.; Majzner, R. G.; Mackall, C. L. Programming CAR-T Cells to Kill Cancer. *Nat. Biomed. Eng.* **2018**, *2* (6), 377–391. https://doi.org/10.1038/s41551-018-0235-9.

(125) Long, A. H.; Haso, W. M.; Shern, J. F.; Wanhainen, K. M.; Murgai, M.; Ingaramo, M.; Smith, J. P.; Walker, A. J.; Kohler, M. E.; Venkateshwara, V. R.; Kaplan, R.

N.; Patterson, G. H.; Fry, T. J.; Orentas, R. J.; Mackall, C. L. 4-1BB Costimulation Ameliorates T Cell Exhaustion Induced by Tonic Signaling of Chimeric Antigen Receptors. *Nat. Med.* **2015**, *21* (6), 581–590. https://doi.org/10.1038/nm.3838.

(126) Fraietta, J. A.; Lacey, S. F.; Orlando, E. J.; Pruteanu-Malinici, I.; Gohil, M.; Lundh, S.; Boesteanu, A. C.; Wang, Y.; O'Connor, R. S.; Hwang, W.-T.; Pequignot, E.; Ambrose, D. E.; Zhang, C.; Wilcox, N.; Bedoya, F.; Dorfmeier, C.; Chen, F.; Tian, L.; Parakandi, H.; Gupta, M.; Young, R. M.; Johnson, F. B.; Kulikovskaya, I.; Liu, L.; Xu, J.; Kassim, S. H.; Davis, M. M.; Levine, B. L.; Frey, N. V; Siegel, D. L.; Huang, A. C.; Wherry, E. J.; Bitter, H.; Brogdon, J. L.; Porter, D. L.; June, C. H.; Melenhorst, J. J. Determinants of Response and Resistance to CD19 Chimeric Antigen Receptor (CAR) T Cell Therapy of Chronic Lymphocytic Leukemia. *Nat. Med.* **2018**, *24* (5), 563–571. https://doi.org/10.1038/s41591-018-0010-1.

(127) Lim, W. A.; June, C. H. The Principles of Engineering Immune Cells to Treat Cancer. *Cell* **2017**, *168* (4), 724–740. https://doi.org/10.1016/j.cell.2017.01.016.

(128) Vitanza, N. A.; Johnson, A. J.; Wilson, A. L.; Brown, C.; Yokoyama, J. K.; Künkele, A.; Chang, C. A.; Rawlings-Rhea, S.; Huang, W.; Seidel, K.; Albert, C. M.; Pinto, N.; Gust, J.; Finn, L. S.; Ojemann, J. G.; Wright, J.; Orentas, R. J.; Baldwin, M.; Gardner, R. A.; Jensen, M. C.; Park, J. R. Locoregional Infusion of HER2-Specific CAR T Cells in Children and Young Adults with Recurrent or Refractory CNS Tumors: An Interim Analysis. *Nat. Med.* **2021**, *27* (9), 1544–1552. https://doi.org/10.1038/s41591-021-01404-8.

(129) Martinez, M.; Moon, E. K. CAR T Cells for Solid Tumors: New Strategies for Finding, Infiltrating, and Surviving in the Tumor Microenvironment . *Frontiers in*

Immunology . 2019.

(130) Li, H.; Huang, Y.; Jiang, D.-Q.; Cui, L.-Z.; He, Z.; Wang, C.; Zhang, Z.-W.; Zhu, H.-L.; Ding, Y.-M.; Li, L.-F.; Li, Q.; Jin, H.-J.; Qian, Q.-J. Antitumor Activity of EGFR-Specific CAR T Cells against Non-Small-Cell Lung Cancer Cells in Vitro and in Mice. *Cell Death Dis.* **2018**, *9* (2), 177. https://doi.org/10.1038/s41419-017-0238-6.

(131) Thistlethwaite, F. C.; Gilham, D. E.; Guest, R. D.; Rothwell, D. G.; Pillai, M.; Burt, D. J.; Byatte, A. J.; Kirillova, N.; Valle, J. W.; Sharma, S. K.; Chester, K. A.; Westwood, N. B.; Halford, S. E. R.; Nabarro, S.; Wan, S.; Austin, E.; Hawkins, R. E. The Clinical Efficacy of First-Generation Carcinoembryonic Antigen (CEACAM5)-Specific CAR T Cells Is Limited by Poor Persistence and Transient Pre-Conditioning-Dependent Respiratory Toxicity. *Cancer Immunol. Immunother.* **2017**, *66* (11), 1425–1436. https://doi.org/10.1007/s00262-017-2034-7.

(132) Richman, S. A.; Nunez-Cruz, S.; Moghimi, B.; Li, L. Z.; Gershenson, Z. T.; Mourelatos, Z.; Barrett, D. M.; Grupp, S. A.; Milone, M. C. High-Affinity GD2-Specific CAR T Cells Induce Fatal Encephalitis in a Preclinical Neuroblastoma Model. *Cancer Immunol. Res.* **2018**, *6* (1), 36–46. https://doi.org/10.1158/2326-6066.CIR-17-0211.

(133) Wei, X.; Lai, Y.; Li, J.; Qin, L.; Xu, Y.; Zhao, R.; Li, B.; Lin, S.; Wang, S.; Wu, Q.; Liang, Q.; Peng, M.; Yu, F.; Li, Y.; Zhang, X.; Wu, Y.; Liu, P.; Pei, D.; Yao, Y.; Li, P. PSCA and MUC1 in Non-Small-Cell Lung Cancer as Targets of Chimeric Antigen Receptor T Cells. *Oncoimmunology* **2017**, *6* (3), e1284722. https://doi.org/10.1080/2162402X.2017.1284722.

(134) Morgan, R. A.; Yang, J. C.; Kitano, M.; Dudley, M. E.; Laurencot, C. M.; Rosenberg, S. A. Case Report of a Serious Adverse Event Following the Administration of t Cells Transduced with a Chimeric Antigen Receptor Recognizing ERBB2. *Mol. Ther.* **2010**, *18* (4), 843–851. https://doi.org/10.1038/mt.2010.24.

(135) Srivastava, S.; Salter, A. I.; Liggitt, D.; Yechan-Gunja, S.; Sarvothama, M.; Cooper, K.; Smythe, K. S.; Dudakov, J. A.; Pierce, R. H.; Rader, C.; Riddell, S. R. Logic-Gated ROR1 Chimeric Antigen Receptor Expression Rescues T Cell-Mediated Toxicity to Normal Tissues and Enables Selective Tumor Targeting. *Cancer Cell* **2019**, *35* (3), 489-503.e8. https://doi.org/10.1016/j.ccell.2019.02.003.

(136) Roybal, K. T.; Rupp, L. J.; Morsut, L.; Walker, W. J.; McNally, K. A.; Park, J. S.; Lim, W. A. Precision Tumor Recognition by T Cells with Combinatorial Antigen-Sensing Circuits. *Cell* **2016**, *164* (4), 770–779. https://doi.org/10.1016/j.cell.2016.01.011.

(137) Liu, X.; Jiang, S.; Fang, C.; Yang, S.; Olalere, D.; Pequignot, E. C.; Cogdill, A. P.; Li, N.; Ramones, M.; Granda, B.; Zhou, L.; Loew, A.; Young, R. M.; June, C. H.; Zhao, Y. Affinity-Tuned ErbB2 or EGFR Chimeric Antigen Receptor T Cells Exhibit an Increased Therapeutic Index against Tumors in Mice. *Cancer Res.* **2015**, *75* (17), 3596–3607. https://doi.org/10.1158/0008-5472.CAN-15-0159.

(138) James, J. R. Tuning ITAM Multiplicity on T Cell Receptors Can Control Potency and Selectivity to Ligand Density. *Sci. Signal.* **2018**, *11* (531). https://doi.org/10.1126/scisignal.aan1088.

(139) Majzner, R. G.; Rietberg, S. P.; Sotillo, E.; Dong, R.; Vachharajani, V. T.;

Labanieh, L.; Myklebust, J. H.; Kadapakkam, M.; Weber, E. W.; Tousley, A. M.; Richards, R. M.; Heitzeneder, S.; Nguyen, S. M.; Wiebking, V.; Theruvath, J.; Lynn, R. C.; Xu, P.; Dunn, A. R.; Vale, R. D.; Mackall, C. L. Tuning the Antigen Density Requirement for Car T-Cell Activity. *Cancer Discov.* **2020**, *10* (5), 702–723. https://doi.org/10.1158/2159-8290.CD-19-0945.

(140) Hernandez-Lopez, R. A.; Yu, W.; Cabral, K. A.; Creasey, O. A.; Lopez Pazmino, M. del P.; Tonai, Y.; De Guzman, A.; Mäkelä, A.; Saksela, K.; Gartner, Z. J.; Lim, W. A. T Cell Circuits That Sense Antigen Density with an Ultrasensitive Threshold. *Science (80-.).* **2021**, *371* (6534), 1166 LP – 1171. https://doi.org/10.1126/science.abc1855.

(141) Caruso, H. G.; Hurton, L. V.; Najjar, A.; Rushworth, D.; Ang, S.; Olivares, S.; Mi, T.; Switzer, K.; Singh, H.; Huls, H.; Lee, D. A.; Heimberger, A. B.; Champlin, R. E.; Cooper, L. J. N. Tuning Sensitivity of CAR to EGFR Density Limits Recognition of Normal Tissue While Maintaining Potent Antitumor Activity. *Cancer Res.* **2015**, *75* (17), 3505–3518. https://doi.org/10.1158/0008-5472.CAN-15-0139.

(142) Park, S.; Shevlin, E.; Vedvyas, Y.; Zaman, M.; Park, S.; Hsu, Y. M. S.; Min, I. M.; Jin, M. M. Micromolar Affinity CAR T Cells to ICAM-1 Achieves Rapid Tumor Elimination While Avoiding Systemic Toxicity. *Sci. Rep.* **2017**, *7* (1), 1–15. https://doi.org/10.1038/s41598-017-14749-3.

(143) Davenport, A. J.; Cross, R. S.; Watson, K. A.; Liao, Y.; Shi, W.; Prince, H. M.; Beavis, P. A.; Trapani, J. A.; Kershaw, M. H.; Ritchie, D. S.; Darcy, P. K.; Neeson, P. J.; Jenkins, M. R. Chimeric Antigen Receptor T Cells Form Nonclassical and Potent Immune Synapses Driving Rapid Cytotoxicity. *Proc. Natl. Acad. Sci. U. S.*

A. **2018**, *115* (9), E2068–E2076. https://doi.org/10.1073/pnas.1716266115.

(144) Gudipati, V.; Rydzek, J.; Doel-Perez, I.; Gonçalves, V. D. R.; Scharf, L.; Königsberger, S.; Lobner, E.; Kunert, R.; Einsele, H.; Stockinger, H.; Hudecek, M.; Huppa, J. B. Inefficient CAR-Proximal Signaling Blunts Antigen Sensitivity. *Nat. Immunol.* **2020**, *21* (8), 848–856. https://doi.org/10.1038/s41590-020-0719-0.

(145) James, S. E.; Greenberg, P. D.; Jensen, M. C.; Lin, Y.; Wang, J.; Till, B. G.; Raubitschek, A. A.; Forman, S. J.; Press, O. W. Antigen Sensitivity of CD22-Specific Chimeric TCR Is Modulated by Target Epitope Distance from the Cell Membrane. *J. Immunol.* **2008**, *180* (10), 7028 LP – 7038. https://doi.org/10.4049/jimmunol.180.10.7028.

(146) McComb, S.; Nguyen, T.; Shepherd, A.; Henry, K. A.; Bloemberg, D.; Marcil, A.; Maclean, S.; Gilbert, R.; Gadoury, C.; Pon, R.; Sulea, T.; Zhu, Q.; Weeratna, R. D. Antigenic Sensitivity of Membrane-Proximal Targeting Chimeric Antigen Receptors Can Be Fine-Tuned through Hinge Truncation. *bioRxiv* **2021**, 2020.10.30.360925. https://doi.org/10.1101/2020.10.30.360925.

(147) Stone, J. D.; Chervin, A. S.; Kranz, D. M. T-Cell Receptor Binding Affinities and Kinetics: Impact on T-Cell Activity and Specificity. *Immunology* **2009**, *126* (2), 165–176. https://doi.org/10.1111/j.1365-2567.2008.03015.x.

(148) Harris, D. T.; Hager, M. V.; Smith, S. N.; Cai, Q.; Stone, J. D.; Kruger, P.; Lever, M.; Dushek, O.; Schmitt, T. M.; Greenberg, P. D.; Kranz, D. M. Comparison of T Cell Activities Mediated by Human TCRs and CARs That Use the Same Recognition Domains. *J. Immunol.* **2018**, *200* (3), 1088–1100. https://doi.org/10.4049/jimmunol.1700236.

(149) Ghorashian, S.; Kramer, A. M.; Onuoha, S.; Wright, G.; Bartram, J.; Richardson, R.; Albon, S. J.; Casanovas-Company, J.; Castro, F.; Popova, B.; Villanueva, K.; Yeung, J.; Vetharoy, W.; Guvenel, A.; Wawrzyniecka, P. A.; Mekkaoui, L.; Cheung, G. W.-K.; Pinner, D.; Chu, J.; Lucchini, G.; Silva, J.; Ciocarlie, O.; Lazareva, A.; Inglott, S.; Gilmour, K. C.; Ahsan, G.; Ferrari, M.; Manzoor, S.; Champion, K.; Brooks, T.; Lopes, A.; Hackshaw, A.; Farzaneh, F.; Chiesa, R.; Rao, K.; Bonney, D.; Samarasinghe, S.; Goulden, N.; Vora, A.; Veys, P.; Hough, R.; Wynn, R.; Pule, M. A.; Amrolia, P. J. Enhanced CAR T Cell Expansion and Prolonged Persistence in Pediatric Patients with ALL Treated with a Low-Affinity CD19 CAR. *Nat. Med.* **2019**, *25* (9), 1408–1414. https://doi.org/10.1038/s41591-019-0549-5.

(150) Corse, E.; Gottschalk, R. A.; Krogsgaard, M.; Allison, J. P. Attenuated T Cell Responses to a High-Potency Ligand in Vivo. *PLoS Biol.* **2010**, *8* (9), 1–12. https://doi.org/10.1371/journal.pbio.1000481.

(151) McMahan, R. H.; McWilliams, J. A.; Jordan, K. R.; Dow, S. W.; Wilson, D. B.; Slansky, J. E. Relating TCR-Peptide-MHC Affinity to Immunogenicity for the Design of Tumor Vaccines. *J. Clin. Invest.* **2006**, *116* (9), 2543–2551. https://doi.org/10.1172/JCI26936.

(152) Kalergis, A. H.; Boucheron, N.; Doucey, M. A.; Palmieri, E.; Goyarts, E. C.; Vegh, Z.; Luescher, I. F.; Nathenson, S. G. Efficient T Cell Activation Requires an Optimal Dwell-Time of Interaction between the TCR and the PMHC Complex. *Nat. Immunol.* **2001**, *2* (3), 229–234. https://doi.org/10.1038/85286.

(153) Schmid, D. A.; Irving, M. B.; Posevitz, V.; Hebeisen, M.; Posevitz-Fejfar, A.;

Sarria, J.-C. F.; Gomez-Eerland, R.; Thome, M.; Schumacher, T. N. M.; Romero, P.; Speiser, D. E.; Zoete, V.; Michielin, O.; Rufer, N. Evidence for a TCR Affinity Threshold Delimiting Maximal CD8 T Cell Function. *J. Immunol.* **2010**, *184* (9), 4936 LP – 4946. https://doi.org/10.4049/jimmunol.1000173.

(154) Evavold, B. D.; Allen, P. M. Separation of IL-4 Production from Th Cell Proliferation by an Altered T Cell Receptor Ligand. **1991**, *252* (5010), 1308–1310.

(155) Hudrisier, D.; Kessler, B.; Valitutti, S.; Horvath, C.; Cerottini, J. C.; Luescher, I. F. The Efficiency of Antigen Recognition by CD8+ CTL Clones Is Determined by the Frequency of Serial TCR Engagement. *J. Immunol.* **1998**, *161* (2), 553–562.

(156) Ueno, T.; Tomiyama, H.; Fujiwara, M.; Oka, S.; Takiguchi, M. Functionally Impaired HIV-Specific CD8 T Cells Show High Affinity TCR-Ligand Interactions. *J. Immunol.* **2004**, *173* (9), 5451 LP – 5457. https://doi.org/10.4049/jimmunol.173.9.5451.

(157) Coombs, D.; Kalergis, A. M.; Nathenson, S. G.; Wofsy, C.; Goldstein, B. Activated TCRs Remain Marked for Internalization after Dissociation from PMHC. *Nat. Immunol.* **2002**, *3* (10), 926–931. https://doi.org/10.1038/ni838.

(158) Hebeisen, M.; Baitsch, L.; Presotto, D.; Baumgaertner, P.; Romero, P.; Michielin, O.; Speiser, D. E.; Rufer, N. SHP-1 Phosphatase Activity Counteracts Increased T Cell Receptor Affinity. *J. Clin. Invest.* **2013**, *123* (3), 1044–1065. https://doi.org/10.1172/JCI65325.

(159) Starr, T. K.; Jameson, S. C.; Hogquist, K. A. Positive and Negative Selection of T Cells. *Annu. Rev. Immunol.* **2003**, *21*, 139–176. https://doi.org/10.1146/annurev.immunol.21.120601.141107.

(160) Savage, P. A.; Davis, M. M. A Kinetic Window Constricts the T Cell Receptor Repertoire in the Thymus. *Immunity* **2001**, *14* (3), 243–252. https://doi.org/10.1016/s1074-7613(01)00106-6.

(161) Kaech, S. M.; Wherry, E. J.; Ahmed, R. Effector and Memory T-Cell Differentiation: Implications for Vaccine Development. *Nat. Rev. Immunol.* **2002**, *2* (4), 251–262. https://doi.org/10.1038/nri778.

(162) Zhu, J. T Helper Cell Differentiation, Heterogeneity, and Plasticity. *Cold Spring Harb. Perspect. Biol.* **2018**, *10* (10). https://doi.org/10.1101/cshperspect.a030338.

(163) Zhang, X.; Brunner, T.; Carter, L.; Dutton, R. W.; Rogers, P.; Bradley, L.; Sato, T.; Reed, J. C.; Green, D.; Swain, S. L. Unequal Death in T Helper Cell (Th)1 and Th2 Effectors: Th1, but Not Th2, Effectors Undergo Rapid Fas/FasL-Mediated Apoptosis. *J. Exp. Med.* **1997**, *185* (10), 1837–1849. https://doi.org/10.1084/jem.185.10.1837.

(164) McLane, L. M.; Abdel-Hakeem, M. S.; Wherry, E. J. CD8 T Cell Exhaustion During Chronic Viral Infection and Cancer. *Annu. Rev. Immunol.* **2019**, *37*, 457–495. https://doi.org/10.1146/annurev-immunol-041015-055318.

(165) Philip, M.; Schietinger, A. CD8+ T Cell Differentiation and Dysfunction in Cancer. *Nat. Rev. Immunol.* **2022**, *22* (4), 209–223. https://doi.org/10.1038/s41577-021-00574-3.

(166) Glauert, A. M.; Sanderson, C. J. The Mechanism of K-Cell (Antibody-Dependent) Mediated Cytotoxicity. III. The Ultrastructure of K Cell Projections and Their Possible Role in Target Cell Killing. *J. Cell Sci.* **1979**, *35*, 355–366. https://doi.org/10.1242/jcs.35.1.355.

(167) Bunnell, S. C.; Kapoor, V.; Trible, R. P.; Zhang, W.; Samelson, L. E. Dynamic Actin Polymerization Drives T Cell Receptor-Induced Spreading: A Role for the Signal Transduction Adaptor LAT. *Immunity* **2001**, *14* (3), 315–329. https://doi.org/10.1016/s1074-7613(01)00112-1.

(168) Stinchcombe, J. C.; Bossi, G.; Booth, S.; Griffiths, G. M. The Immunological Synapse of CTL Contains a Secretory Domain and Membrane Bridges. *Immunity* **2001**, *15* (5), 751–761. https://doi.org/10.1016/s1074-7613(01)00234-5.

(169) Ueda, H.; Morphew, M. K.; McIntosh, J. R.; Davis, M. M. CD4 + T-Cell Synapses Involve Multiple Distinct Stages. *Proc. Natl. Acad. Sci. U. S. A.* **2011**, *108* (41), 17099–17104. https://doi.org/10.1073/pnas.1113703108.

(170) Sage, P. T.; Varghese, L. M.; Martinelli, R.; Sciuto, T. E.; Kamei, M.; Dvorak, A. M.; Springer, T. A.; Sharpe, A. H.; Carman, C. V. Antigen Recognition Is Facilitated by Invadosome-like Protrusions Formed by Memory/Effector T Cells. *J. Immunol.* **2012**, *188* (8), 3686–3699. https://doi.org/10.4049/jimmunol.1102594.

(171) Pierres, A.; Monnet-Corti, V.; Benoliel, A.-M.; Bongrand, P. Do Membrane Undulations Help Cells Probe the World? *Trends Cell Biol.* **2009**, *19* (9), 428–433. https://doi.org/10.1016/j.tcb.2009.05.009.

(172) Miller, M. J.; Wei, S. H.; Parker, I.; Cahalan, M. D. Two-Photon Imaging of Lymphocyte Motility and Antigen Response in Intact Lymph Node. *Science* **2002**, *296* (5574), 1869–1873. https://doi.org/10.1126/science.1070051.

(173) Krummel, M. F.; Bartumeus, F.; Gérard, A. T Cell Migration, Search Strategies and Mechanisms. *Nat. Rev. Immunol.* **2016**, *16* (3), 193–201. https://doi.org/10.1038/nri.2015.16.

(174) Seuront, L. *Fractals and Multifractals in Ecology and Aquatic Sciences*; CRC Press, 2009.

(175) Michael F, B. *Fractals Everywhere*; Academic Press: New York, 1988.

(176) Méndez, V.; Campos, D.; Bartumeus, F. *Stochastic Foundations in Movement Ecology: Anomalous Diffusion, Invasion Fronts and Random Searches*; Springer Verlag: Gerlin, 2013.

(177) Alakoskela, J.-M.; Koner, A. L.; Rudnicka, D.; Köhler, K.; Howarth, M.; Davis, D. M. Mechanisms for Size-Dependent Protein Segregation at Immune Synapses Assessed with Molecular Rulers. *Biophys. J.* **2011**, *100* (12), 2865–2874. https://doi.org/10.1016/j.bpj.2011.05.013.

(178) Au-Yeung, B. B.; Melichar, H. J.; Ross, J. O.; Cheng, D. A.; Zikherman, J.; Shokat, K. M.; Robey, E. A.; Weiss, A. Quantitative and Temporal Requirements Revealed for Zap70 Catalytic Activity during T Cell Development. *Nat. Immunol.* **2014**, *15* (7), 687–694. https://doi.org/10.1038/ni.2918.

(179) Kumari, S.; Depoil, D.; Martinelli, R.; Judokusumo, E.; Carmona, G.; Gertler, F. B.; Kam, L. C.; Carman, C. V.; Burkhardt, J. K.; Irvine, D. J.; Dustin, M. L. Actin Foci Facilitate Activation of the Phospholipase C-Gamma in Primary T Lymphocytes via the WASP Pathway. *Elife* **2015**, *2015* (4), 1–31. https://doi.org/10.7554/eLife.04953.

(180) Ritter, A. T.; Asano, Y.; Stinchcombe, J. C.; Dieckmann, N. M. G.; Chen, B. C.; Gawden-Bone, C.; van Engelenburg, S.; Legant, W.; Gao, L.; Davidson, M. W.; Betzig, E.; Lippincott-Schwartz, J.; Griffiths, G. M. Actin Depletion Initiates Events Leading to Granule Secretion at the Immunological Synapse. *Immunity* **2015**, *42*

(5), 864–876. https://doi.org/10.1016/j.immuni.2015.04.013.

(181) Germain, R. N. T-Cell Signaling: The Importance of Receptor Clustering. *Curr. Biol.* **1997**, *7* (10), R640-4. https://doi.org/10.1016/s0960-9822(06)00323-x.

(182) Lyons, D. S.; Lieberman, S. A.; Hampl, J.; Boniface, J. J.; Chien, Y.; Berg, L. J.; Davis, M. M. A TCR Binds to Antagonist Ligands with Lower Affinities and Faster Dissociation Rates than to Agonists. *Immunity* **1996**, *5* (1), 53–61. https://doi.org/10.1016/s1074-7613(00)80309-x.

(183) Hashimoto-Tane, A.; Sakuma, M.; Ike, H.; Yokosuka, T.; Kimura, Y.; Ohara, O.; Saito, T. Micro–Adhesion Rings Surrounding TCR Microclusters Are Essential for T Cell Activation. *J. Exp. Med.* **2016**, jem.20151088. https://doi.org/10.1084/jem.20151088.

(184) Muzumdar, M. D.; Tasic, B.; Miyamichi, K.; Li, L.; Luo, L. A Global Double-Fluorescent Cre Reporter Mouse. *Genesis* **2007**, *45* (9), 593–605. https://doi.org/10.1002/dvg.20335.

(185) Gérard, A.; Khan, O.; Beemiller, P.; Oswald, E.; Hu, J.; Matloubian, M.; Krummel, M. F. Secondary T Cell-T Cell Synaptic Interactions Drive the Differentiation of Protective CD8+ T Cells. *Nat. Immunol.* **2013**, *14* (4), 356–363. https://doi.org/10.1038/ni.2547.

(186) Paszek, M. J.; DuFort, C. C.; Rubashkin, M. G.; Davidson, M. W.; Thorn, K. S.; Liphardt, J. T.; Weaver, V. M. Scanning Angle Interference Microscopy Reveals Cell Dynamics at the Nanoscale. *Nat. Methods* **2012**, *9* (8), 825–827. https://doi.org/10.1038/nmeth.2077.

(187) Sauvanet, C.; Wayt, J.; Pelaseyed, T.; Bretscher, A. Structure, Regulation, and

Functional Diversity of Microvilli on the Apical Domain of Epithelial Cells. *Annu. Rev. Cell Dev. Biol.* **2015**, *31*, 593–621. https://doi.org/10.1146/annurev-cellbio-100814-125234.

(188) Cai, E.; Marchuk, K.; Beemiller, P.; Beppler, C.; Rubashkin, M. G.; Weaver, V. M.; Gerard, A.; Liu, T.-L.; Chen, B.-C.; Betzig, E.; Bartumeus, F.; Krummel, M. F. Visualizing Dynamic Microvillar Search and Stabilization during Ligand Detection by T Cells. *Science (80-.).* **2017**, *356*. https://doi.org/10.1126/science.aal3118.

(189) Orbach, R.; Su, X. Surfing on Membrane Waves: Microvilli, Curved Membranes, and Immune Signaling. *Front. Immunol.* **2020**, *11* (September). https://doi.org/10.3389/fimmu.2020.02187.

(190) Pettmann, J.; Santos, A. M.; Dushek, O.; Davis, S. J. Membrane Ultrastructure and T Cell Activation. *Front. Immunol.* **2018**, *9* (SEP), 1–9. https://doi.org/10.3389/fimmu.2018.02152.

(191) Razvag, Y.; Neve-Oz, Y.; Sajman, J.; Reches, M.; Sherman, E. Nanoscale Kinetic Segregation of TCR and CD45 in Engaged Microvilli Facilitates Early T Cell Activation. *Nat. Commun.* **2018**, *9* (1). https://doi.org/10.1038/s41467-018-03127-w.

(192) Aramesh, M.; Stoycheva, D.; Sandu, I.; Ihle, S. J.; Zünd, T.; Shiu, J. Y.; Forró, C.; Asghari, M.; Bernero, M.; Lickert, S.; Oxenius, A.; Vogel, V.; Klotzsch, E. Nanoconfinement of Microvilli Alters Gene Expression and Boosts T Cell Activation. *Proc. Natl. Acad. Sci. U. S. A.* **2021**, *118* (40). https://doi.org/10.1073/pnas.2107535118.

(193) Garcia, K. C.; Scott, C. A.; Brunmark, A.; Carbonet, F. R.; Peterson, P. A.; Wilson,

I. A.; Teyton, L. CD8 Enhances Formation of Stable T-Cell Receptor/MHC Class I Molecule Complexes. **1996**, *384* (December), 577–581.

(194) Salter, A. I.; Rajan, A.; Kennedy, J. J.; Ivey, R. G.; Shelby, S. A.; Leung, I.; Templeton, M. L.; Muhunthan, V.; Voillet, V.; Sommermeyer, D.; Whiteaker, J. R.; Gottardo, R.; Veatch, S. L.; Paulovich, A. G.; Riddell, S. R. Comparative Analysis of TCR and CAR Signaling Informs CAR Designs with Superior Antigen Sensitivity and in Vivo Function. *Sci. Signal.* **2021**, *14* (697). https://doi.org/10.1126/scisignal.abe2606.

(195) Viola, A.; Linkert, S.; Lanzavecchia, A. A T Cell Receptor (TCR) Antagonist Competitively Inhibits Serial TCR Triggering by Low-Affinity Ligands, but Does Not Affect Triggering by High-Affinity Anti-CD3 Antibodies. *Eur. J. Immunol.* **1997**, *27* (11), 3080–3083. https://doi.org/10.1002/eji.1830271146.

(196) Shakiba, M.; Zumbo, P.; Espinosa-Carrasco, G.; Menocal, L.; Dündar, F.; Carson, S. E.; Bruno, E. M.; Sanchez-Rivera, F. J.; Lowe, S. W.; Camara, S.; Koche, R. P.; Reuter, V. P.; Socci, N. D.; Whitlock, B.; Tamzalit, F.; Huse, M.; Hellmann, M. D.; Wells, D. K.; Defranoux, N. A.; Betel, D.; Philip, M.; Schietinger, A. TCR Signal Strength Defines Distinct Mechanisms of T Cell Dysfunction and Cancer Evasion. *J. Exp. Med.* **2021**, *219* (2). https://doi.org/10.1084/jem.20201966.

(197) Lillemeier, B. F.; Pfeiffer, J. R.; Surviladze, Z.; Wilson, B. S.; Davis, M. M. Plasma Membrane-Associated Proteins Are Clustered into Islands Attached to the Cytoskeleton. *Proc. Natl. Acad. Sci. U. S. A.* **2006**, *103* (50), 18992–18997. https://doi.org/10.1073/pnas.0609009103.

(198) Hu, Y. S.; Cang, H.; Lillemeier, B. F. Superresolution Imaging Reveals

Nanometer- and Micrometer-Scale Spatial Distributions of T-Cell Receptors in Lymph Nodes. *Proc. Natl. Acad. Sci. U. S. A.* **2016**, *113* (26), 7201–7206. https://doi.org/10.1073/pnas.1512331113.

(199) Farrell, M. V.; Webster, S.; Gaus, K.; Goyette, J. T Cell Membrane Heterogeneity Aids Antigen Recognition and T Cell Activation. *Front. Cell Dev. Biol.* **2020**, *8* (July), 1–9. https://doi.org/10.3389/fcell.2020.00609.

(200) Nobili, S.; Mannini, A.; Parenti, A.; Raggi, C.; Lapucci, A.; Chiorino, G.; Paccosi, S.; Di Gennaro, P.; Vezzosi, V.; Romagnoli, P.; Susini, T.; Coronnello, M. Establishment and Characterization of a New Spontaneously Immortalized ER−/PR−/HER2+ Human Breast Cancer Cell Line, DHSF-BR16. *Sci. Rep.* **2021**, *11* (1), 8340. https://doi.org/10.1038/s41598-021-87362-0.

(201) Liu, X.; Jiang, S.; Fang, C.; Yang, S.; Olalere, D.; Pequignot, E. C.; Cogdill, A. P.; Li, N.; Ramones, M.; Granda, B.; Zhou, L.; Loew, A.; Young, R. M.; June, C. H.; Zhao, Y. Affinity-Tuned ErbB2 or EGFR Chimeric Antigen Receptor T Cells Exhibit an Increased Therapeutic Index against Tumors in Mice. *Cancer Res.* **2015**, *75* (17), 3596–3607. https://doi.org/10.1158/0008-5472.CAN-15-0159.

(202) Comsa, Ş.; Cimpean, A. M.; Raica, M. The Story of MCF-7 Breast Cancer Cell Line: 40 Years of Experience in Research. *Anticancer Res.* **2015**, *35* (6), 3147 LP – 3154.

(203) Beemiller, P.; Jacobelli, J.; Krummel, M. Imaging and Analysis of OT1 T Cell Activation on Lipid Bilayers. *Protoc. Exch.* **2012**. https://doi.org/10.1038/protex.2012.028.

(204) Mota, A. de L.; Evangelista, A. F.; Macedo, T.; Oliveira, R.; Scapulatempo-Neto,

C.; Vieira, R. A. da C.; Marques, M. M. C. Molecular Characterization of Breast Cancer Cell Lines by Clinical Immunohistochemical Markers. *Oncol. Lett.* **2017**, *13* (6), 4708–4712. https://doi.org/10.3892/ol.2017.6093.

(205) Friedman, R. S.; Jacobelli, J.; Krummel, M. F. Surface-Bound Chemokines Capture and Prime T Cells for Synapse Formation. *Nat. Immunol.* **2006**, *7* (10), 1101–1108. https://doi.org/10.1038/ni1384.

(206) Scharping, N. E.; Rivadeneira, D. B.; Menk, A. V.; Vignali, P. D. A.; Ford, B. R.; Rittenhouse, N. L.; Peralta, R.; Wang, Y.; Wang, Y.; DePeaux, K.; Poholek, A. C.; Delgoffe, G. M. Mitochondrial Stress Induced by Continuous Stimulation under Hypoxia Rapidly Drives T Cell Exhaustion. *Nat. Immunol.* **2021**, *22* (2), 205–215. https://doi.org/10.1038/s41590-020-00834-9.

(207) Lyon, A. S.; Peeples, W. B.; Rosen, M. K. A Framework for Understanding the Functions of Biomolecular Condensates across Scales. *Nat. Rev. Mol. Cell Biol.* **2021**, *22* (3), 215–235. https://doi.org/10.1038/s41580-020-00303-z.

(208) Thompson, S. B.; Waldman, M. M.; Jacobelli, J. Polymerization Power: Effectors of Actin Polymerization as Regulators of T Lymphocyte Migration through Complex Environments. *FEBS J.* **2021**, 1–18. https://doi.org/10.1111/febs.16130.

(209) Dupré, L.; Boztug, K.; Pfajfer, L. Actin Dynamics at the T Cell Synapse as Revealed by Immune-Related Actinopathies. *Front. Cell Dev. Biol.* **2021**, *9* (June). https://doi.org/10.3389/fcell.2021.665519.

(210) Leithner, A.; Altenburger, L. M.; Hauschild, R.; Assen, F. P.; Rottner, K.; Stradal, T. E. B.; Diz-Muñoz, A.; Stein, J. V.; Sixt, M. Dendritic Cell Actin Dynamics Control Contact Duration and Priming Efficiency at the Immunological Synapse. *J.*

Cell Biol. **2021**, *220* (4). https://doi.org/10.1083/JCB.202006081.

(211) Colin-York, H.; Javanmardi, Y.; Skamrahl, M.; Kumari, S.; Chang, V. T.; Khuon, S.; Taylor, A.; Chew, T. L.; Betzig, E.; Moeendarbary, E.; Cerundolo, V.; Eggeling, C.; Fritzsche, M. Cytoskeletal Control of Antigen-Dependent T Cell Activation. *Cell Rep.* **2019**, *26* (12), 3369-3379.e5. https://doi.org/10.1016/j.celrep.2019.02.074.

(212) Mossman, K. D.; Campi, G.; Groves, J. T.; Dustin, M. L. Altered TCR Signaling from Geometrically Repatterned Immunological Synapses. *Science (80-.).* **2005**, *310* (5751), 1191–1193. https://doi.org/10.1126/science.1119238.

(213) Dushek, O.; Aleksic, M.; Wheeler, R. J.; Zhang, H.; Cordoba, S. P.; Peng, Y. C.; Chen, J. L.; Cerundolo, V.; Dong, T.; Coombs, D.; Van Der Merwe, P. A. Antigen Potency and Maximal Efficacy Reveal a Mechanism of Efficient T Cell Activation. *Sci. Signal.* **2011**, *4* (176), 1–9. https://doi.org/10.1126/scisignal.2001430.

(214) Blumenthal, D.; Burkhardt, J. K. Multiple Actin Networks Coordinate Mechanotransduction at the Immunological Synapse. *J. Cell Biol.* **2020**, *219* (2), 1–12. https://doi.org/10.1083/jcb.201911058.

(215) Sendra, G. H.; Hoerth, C. H.; Wunder, C.; Lorenz, H. 2D Map Projections for Visualization and Quantitative Analysis of 3D Fluorescence Micrographs. *Sci. Rep.* **2015**, *5* (November 2014). https://doi.org/10.1038/srep12457.

(216) Au-Yeung, B. B.; Levin, S. E.; Zhang, C.; Hsu, L.-Y.; Cheng, D. A.; Killeen, N.; Shokat, K. M.; Weiss, A. A Genetically Selective Inhibitor Demonstrates a Function for the Kinase Zap70 in Regulatory T Cells Independent of Its Catalytic Activity. *Nat. Immunol.* **2010**, *11* (12), 1085–1092. https://doi.org/10.1038/ni.1955.

(217) Jung, Y.; Wen, L.; Altman, A.; Ley, K. CD45 Pre-Exclusion from the Tips of T Cell

Microvilli Prior to Antigen Recognition. *Nat. Commun.* **2021**, *12* (1), 1–16. https://doi.org/10.1038/s41467-021-23792-8.

(218) Alfei, F.; Kanev, K.; Hofmann, M.; Wu, M.; Ghoneim, H. E.; Roelli, P.; Utzschneider, D. T.; von Hoesslin, M.; Cullen, J. G.; Fan, Y.; Eisenberg, V.; Wohlleber, D.; Steiger, K.; Merkler, D.; Delorenzi, M.; Knolle, P. A.; Cohen, C. J.; Thimme, R.; Youngblood, B.; Zehn, D. TOX Reinforces the Phenotype and Longevity of Exhausted T Cells in Chronic Viral Infection. *Nature* **2019**, *571* (7764), 265–269. https://doi.org/10.1038/s41586-019-1326-9.

(219) Khan, O.; Giles, J. R.; McDonald, S.; Manne, S.; Ngiow, S. F.; Patel, K. P.; Werner, M. T.; Huang, A. C.; Alexander, K. A.; Wu, J. E.; Attanasio, J.; Yan, P.; George, S. M.; Bengsch, B.; Staupe, R. P.; Donahue, G.; Xu, W.; Amaravadi, R. K.; Xu, X.; Karakousis, G. C.; Mitchell, T. C.; Schuchter, L. M.; Kaye, J.; Berger, S. L.; Wherry, E. J. TOX Transcriptionally and Epigenetically Programs CD8(+) T Cell Exhaustion. *Nature* **2019**, *571* (7764), 211–218. https://doi.org/10.1038/s41586-019-1325-x.

(220) Hyrenius-Wittsten, A.; Su, Y.; Park, M.; Garcia, J. M.; Alavi, J.; Perry, N.; Montgomery, G.; Liu, B.; Roybal, K. T. SynNotch CAR Circuits Enhance Solid Tumor Recognition and Promote Persistent Antitumor Activity in Mouse Models. *Sci. Transl. Med.* **2021**, *13* (591). https://doi.org/10.1126/scitranslmed.abd8836.

(221) Choe, J. H.; Watchmaker, P. B.; Simic, M. S.; Gilbert, R. D.; Li, A. W.; Krasnow, N. A.; Downey, K. M.; Yu, W.; Carrera, D. A.; Celli, A.; Cho, J.; Briones, J. D.; Duecker, J. M.; Goretsky, Y. E.; Dannenfelser, R.; Cardarelli, L.; Troyanskaya, O.; Sidhu, S. S.; Roybal, K. T.; Okada, H.; Lim, W. A. SynNotch-CAR T Cells

Overcome Challenges of Specificity, Heterogeneity, and Persistence in Treating

Glioblastoma. *Sci. Transl. Med.* **2021**, *13* (591).

https://doi.org/10.1126/scitranslmed.abe7378.

(222) Weber, E. W.; Parker, K. R.; Sotillo, E.; Lynn, R. C.; Anbunathan, H.; Lattin, J.;

Good, Z.; Belk, J. A.; Daniel, B.; Klysz, D.; Malipatlolla, M.; Xu, P.; Bashti, M.;

Heitzeneder, S.; Labanieh, L.; Vandris, P.; Majzner, R. G.; Qi, Y.; Sandor, K.;

Chen, L. C.; Prabhu, S.; Gentles, A. J.; Wandless, T. J.; Satpathy, A. T.; Chang,

H. Y.; Mackall, C. L. Transient Rest Restores Functionality in Exhausted CAR-T

Cells through Epigenetic Remodeling. *Science (80-.).* **2021**, *372* (6537).

https://doi.org/10.1126/science.aba1786.

(223) Eyquem, J.; Mansilla-Soto, J.; Giavridis, T.; van der Stegen, S. J. C.; Hamieh, M.;

Cunanan, K. M.; Odak, A.; Gönen, M.; Sadelain, M. Targeting a CAR to the TRAC

Locus with CRISPR/Cas9 Enhances Tumour Rejection. *Nature* **2017**, *543* (7643),

113–117. https://doi.org/10.1038/nature21405.

(224) Fei, C.; W., T. P.; S., B. E. Expansion Microscopy. *Science (80-.).* **2015**, *347*

(6221), 543–548. https://doi.org/10.1126/science.1260088.

(225) Hudecek, M.; Lupo-Stanghellini, M. T.; Kosasih, P. L.; Sommermeyer, D.; Jensen,

M. C.; Rader, C.; Riddell, S. R. Receptor Affinity and Extracellular Domain

Modifications Affect Tumor Recognition by ROR1-Specific Chimeric Antigen

Receptor T Cells. *Clin. Cancer Res.* **2013**, *19* (12), 3153–3164.

https://doi.org/10.1158/1078-0432.CCR-13-0330.

Publishing Agreement

It is the policy of the University to encourage open access and broad distribution of all theses, dissertations, and manuscripts. The Graduate Division will facilitate the distribution of UCSF theses, dissertations, and manuscripts to the UCSF Library for open access and distribution. UCSF will make such theses, dissertations, and manuscripts accessible to the public and will take reasonable steps to preserve these works in perpetuity.

I hereby grant the non-exclusive, perpetual right to The Regents of the University of California to reproduce, publicly display, distribute, preserve, and publish copies of my thesis, dissertation, or manuscript in any form or media, now existing or later derived, including access online for teaching, research, and public service purposes.

DocuSigned by:

Casey Beppler

—9CD03F03FA61499...   Author Signature

5/25/2022

Date